Studies of Sodium Solid-State Batteries with Emphasis on the Catholyte|Active Material Interface in Cathode Composites

Untersuchungen von Natrium-Festkörperbatterien mit Schwerpunkt auf der Katholyt|Aktivmaterial-Grenzfläche in Kathodenkompositen

Dem Fachbereich Biologie und Chemie
der Justus-Liebig-Universität Gießen

vorgelegte
Dissertation
zur Erlangung des akademischen Grades

Doktor der Naturwissenschaft
– Dr. rer. Nat. –

von
Laura Elizabeth Goodwin

Gießen, den 19.04.2024

Dekan/Dean	Prof. Dr. Thomas Wilke
1. Gutachter /1st Reviewer	Prof. Dr. Dr. h. c. Jürgen Janek
2. Gutachter /2nd Reviewer	Prof. Dr. Philipp Adelhelm

Eingereicht/submitted

Erklärung

Ich erkläre: ich habe die vorgelegte Dissertation selbständig und ohne unerlaubte fremde Hilfe und nur mit den Hilfen angefertigt, die ich in der Dissertation angegeben habe. Alle Textstellen, die wörtlich oder sinngemäß aus veröffentlichten Schriften entnommen sind, und alle Angaben, die auf mündlichen Auskünften beruhen, sind als solche kenntlich gemacht. Bei den von mir durchgeführten und in der Dissertation erwähnten Untersuchungen habe ich die Grundsätze guter wissenschaftlicher Praxis, wie sie in der „Satzung der Justus-Liebig-Universität Gießen zu Sicherung guter wissenschaftlicher Praxis“ niedergelegt sind, eingehalten.

Gießen, den 19.04.2024

_____

Laura E. Goodwin

Abstract

Adressing the growing demand for energy storage of renewable energies involves exploring alternatives to lithium-ion batteries. Sodium-based battery materials have gained momentum in research as they offer similar cell chemistry. Additionally, sodium, iron and manganese used in sodium-based cells are more sustainable and cost-effective compared to the classical elements used in high-capacity lithium cells, such as lithium, cobalt and nickel. Despite the higher reactivity of sodium with water, sodium-ion batteries show better safety characteristics. However, they face the drawback of lower energy density compared to lithium counterparts.

To optimise the lower energy density issue, the use of solid electrolytes is being investigated not only in academia but in industry as well. Research on lithium-based systems has already shown an increase in energy density of solid-state batteries by employing anode materials with higher specific capacity, like lithium metal, compared to graphite. Solid-state batteries, in addition to their higher energy density, provide enhanced safety due to the non-flammable nature of solid electrolytes, as opposed to liquid electrolytes. Key challenges of solid-state cells include highly resistive interfaces, contact loss due to volume expansion and contraction of the electrodes, requiring compensation with high pressures, and interface reactions.

Transitioning from lithium to sodium and liquid to solid electrolyte requires careful consideration of the following aspects. Notably, graphite is not an efficient intercalation material for sodium, as sodium-ions do not form stable graphite intercalation compounds due to the size mismatch between sodium and the graphite interlayer spacing. More precisely, the increasing size and at the same time an insufficient chemical bonding between the alkali metal ion and the carbon atoms lead to a positive formation energy. Therefore, either hard carbons, where sodium fills the pores, or elemental sodium is used in sodium-ion batteries. While liquid electrolytes are permeable to dendrites, sodium metal is primarily used as anode material for solid-state cells, along with alloy materials. Hard carbons have been introduced in solid-state cells but encounter challenges in establishing proper contact with the solid electrolyte. Different classes of separator electrolytes for sodium solid-state batteries are under study, each with distinct beneficial properties such as good processability, high ionic conductivity or chemical stability. Cathodes of solid-state batteries are primarily composites of a redox active material with another ion- and often electron-conducting phase, being a solid electrolyte and carbon.

This study focuses on sodium-based all-solid-state battery systems, examining the influence of different electrolytes as separators or catholytes. Cathode composites with sulfide and halide catholytes where prepared, optimized and analyzed. Their cycling performance and especially the reaction with transition metal oxides was studied. Despite the lower ionic conductivity of the halide catholyte, its higher redox

stability allowed cell cycling that was not possible with the sulfide-based electrolyte. Regarding separator electrolytes, sulfides with and without doping were studied, and the need of a protective layer at the anode was determined. This protective layer, represented by an oxide ceramic electrolyte, exhibited beneficial stability at the anode but lacks the necessary flexibility to accommodate pressure changes in the cathode composite. Various methods, including time-of-flight secondary ion mass spectrometry, X-ray photoelectron spectroscopy, electrochemical impedance spectroscopy, scanning electron microscopy and different cycling procedures, were employed to study these phenomena.

Overall, this thesis provides a detailed insight into current challenges in sodium all-solid-state full cells using halide, sulfide and oxide electrolytes. Based on this knowledge clear trends could be determined for future research approaches and optimization procedures. If the favorable sulfide electrolytes are to be used as catholytes, coatings need to be introduced to protect the sulfides from decomposition. The use of the halide with increased chemical stability necessitates an increase of ionic conductivity to ensure the ability to use higher currents. The anode|separator interface has to be improved, potentially by an alternative electrode material such as hard carbon instead of the sodium–tin alloy. The reason is the strong reactivity of the sulfide separator with both sodium metal and the alloy. If oxides may potentially be used, further investigations are needed regarding the mechanical challenges.

Zusammenfassung

Um den wachsenden Bedarf an Energiespeichern für erneuerbare Energien zu decken, müssen Alternativen zu Lithium-Ionen-Batterien erforscht werden. Natriumbasierte Batteriematerialien haben in der Forschung an Bedeutung gewonnen, da sie eine ähnliche Zellchemie bieten. Außerdem sind Natrium, Eisen und Mangan, die in natriumbasierten Zellen verwendet werden, nachhaltiger und kostengünstiger als die klassischen Elemente, die in Lithiumzellen mit hoher Kapazität verwendet werden, wie Lithium, Kobalt und Nickel. Trotz der höheren Reaktivität von Natrium mit Wasser weisen Natrium-Ionen-Batterien bessere Sicherheitseigenschaften auf. Sie haben jedoch den Nachteil einer geringeren Energiedichte im Vergleich zu ihren Lithium-Pendants.

Um das Problem der geringeren Energiedichte zu optimieren, wird der Einsatz von Festelektrolyten nicht nur in der Wissenschaft, sondern auch in der Industrie untersucht. Forschungsarbeiten zu lithiumbasierten Systemen haben bereits gezeigt, dass sich die Energiedichte von Festkörperbatterien durch den Einsatz von Anodenmaterialien mit höherer Energiedichte, wie Lithiummetall, im Vergleich zu Graphit erhöhen lässt. Festkörperbatterien bieten neben ihrer höheren Energiedichte auch eine höhere Sicherheit, da Festelektrolyte im Gegensatz zu Flüssigelektrolyten nicht entflammbar sind. Zu den wichtigsten Herausforderungen von Festkörperzellen gehören hochohmige Grenzflächen, Kontaktverluste aufgrund der Volumenausdehnung und -kontraktion der Elektroden, die durch hohe Drücke kompensiert werden müssen, sowie Grenzflächenreaktionen.

Der Übergang von Lithium zu Natrium und von Flüssig- zu Festelektrolyten erfordert eine sorgfältige Berücksichtigung der folgenden Aspekte. Graphit ist kein effizientes Interkalationsmaterial für Natrium, da Natrium-Ionen aufgrund des Größenunterschieds zwischen Natrium und dem Graphit-Zwischengitterabstand keine stabilen Graphit-Interkalationsverbindungen bildet. Genauer gesagt, die zunehmende Größe und gleichzeitig eine unzureichende chemische Bindung zwischen dem Alkalimetallion und dem C-Atom führen zu einer positiven Bildungsenergie. Daher werden in Natrium-Ionen-Batterien entweder Hartkohlenstoffe, in denen Natrium die Poren füllt, oder elementares Natrium verwendet. Da Flüssigelektrolyte für Dendriten durchlässig sind, wird Natriummetall hauptsächlich als Anodenmaterial in Festkörperzellen verwendet, zusammen mit Legierungsmaterialien. Hartkohlenstoffe wurden bereits in Festkörperzellen untersucht, stoßen jedoch auf Probleme bei der Herstellung eines ausreichenden Kontakts mit dem Elektrolyten. Es werden verschiedene Klassen von Separatorelektrolyten für Natrium-Festkörperbatterien untersucht, die jeweils unterschiedliche vorteilhafte Eigenschaften wie gute Verarbeitbarkeit, hohe Ionenleitfähigkeit oder chemische Stabilität aufweisen. Kathoden von Festkörperbatterien bestehen in erster Linie aus einem redoxaktiven Material, einer anderen ionen- und oft auch elektronenleitenden Phase, nämlich einem Festelektrolyten und Kohlenstoff.

Die Arbeit konzentriert sich auf Natrium-basierte Festkörperbatteriesysteme und dokumentiert den Einfluss verschiedener Elektrolyte als Separatoren oder Katholyten. Kathodenkomposite mit Sulfid- und

Halogenid-Katholyten wurden hergestellt, optimiert und analysiert. Ihre Zyklenstabilität und insbesondere die Reaktion mit Übergangsmetalloxiden wurde untersucht. Trotz der geringeren Ionenleitfähigkeit des Halogenidkatholyten ermöglichte seine höhere Redoxstabilität Zellzyklen, die mit dem Elektrolyten auf Sulfidbasis nicht möglich waren. Bei den Separatorelektrolyten wurden Sulfide mit und ohne Dotierung untersucht, und es wurde festgestellt, dass eine Schutzschicht an der Anode erforderlich ist. Diese Schutzschicht, die durch einen oxidischen Elektrolyten repräsentiert wird, weist eine vorteilhafte Stabilität an der Anode auf, verfügt jedoch nicht über die notwendige Flexibilität, um Druckänderungen im Kathodenkomposit zu kompensieren. Zur Untersuchung dieser Phänomene wurden verschiedene Methoden eingesetzt, darunter Flugzeit-Sekundärionen-Massenspektrometrie, Röntgen-Photoelektronenspektroskopie, elektrochemische Impedanzspektroskopie, Rasterelektronenmikroskopie und verschiedene Zyklisierexperimente.

Insgesamt gibt diese Arbeit einen detaillierten Einblick in die aktuellen Herausforderungen bei Natrium-Festkörper-Vollzellen mit Halogenid-, Sulfid- und Oxid-Elektrolyten. Basierend auf diesen Erkenntnissen konnten klare Trends für zukünftige Optimierungsverfahren ermittelt werden. Sollten die Sulfidelektrolyte als Katholyten eingesetzt werden, müssen Beschichtungen eingeführt werden, um die Sulfide vor Zersetzung zu schützen. Die Verwendung des Halogenids, das erhöhte chemische Stabilität aufweist, erfordert eine Erhöhung der Ionenleitfähigkeit, um höhere Ströme nutzen zu können. Die Grenzfläche zwischen Anode und Separator muss verbessert werden, möglicherweise durch ein alternatives Elektrodenmaterial wie z. B. Hartkohlenstoffe (Hard Carbons) anstelle der Natrium-Zinn-Legierung. Grund dafür ist die starke Reaktivität des Sulfidseparators sowohl mit Natriummetall als auch mit der Legierung. Wenn möglicherweise Oxide verwendet werden, sind weitere Untersuchungen zu den mechanischen Herausforderungen erforderlich.

Inhaltsverzeichnis

1. Introduction

In recent years, the urgency to address climate change and reduce greenhouse gas emissions has driven a significant shift in the transportation sector. The transition from traditional combustion engines to battery electric vehicles (BEVs) has gained considerable momentum, offering a cleaner and more sustainable mode of transportation.

One of the critical factors in enabling the widespread adoption of BEVs is the development of advanced battery technologies capable of storing renewable energies efficiently. Renewable sources such as solar and wind power have become increasingly popular for generating electricity, but the intermittent nature of these sources necessitates effective energy storage solutions. Sodium-ion batteries (SIBs) have emerged as a promising candidate for large-scale energy storage due to the abundant availability of sodium.

While lithium-ion batteries (LIBs) have dominated the market so far, sodium-ion batteries possess the potential to exceed the physicochemical limits of lithium-based systems. Sodium, unlike Na-thing else, is the 6th most abundant element on earth and does not only comprise 2.6 % of the earth crust but also mainly occurs as NaCl in the ocean.[1]

To take a step back, the next few paragraphs will provide an overview of the current state of the art, to help to put this work into perspective. When studying sodium all-solid-state batteries (Na-ASSBs), it is important to consider the history and development of lithium- and sodium-ion batteries, as the basic electrochemical processes are similar and therefore studied in a similar manner. In particular, the work on lithium solid-state batteries, which has been increasingly focused on, should serve as a role model for the studies of Na-ASSBs, as they face many similar challenges.

LIBs have been used in consumer electronics long before becoming the key technology in BEVs. However, the annual growth rate for BEVs and also stationary energy storage systems in terms of the global demand on LIB in GWh is forecasted to be around 30% from 2020 to 2030 underlining its importance in the near future.[2] Leading battery companies like CATL or big car companies such as Volkswagen are investing and building gigafactories to meet the increasing energy storage demand.

The SIBs have been of increasing interest since 2010.[3] HiNa-Batteries, a Chinese company, has commercialized SIBs for low-speed vehicles and large-scale energy storage. But also companies such as Faradion, Tiamat, NaTrium Energy Co. or Natron Energy, to name just a few, are either on the verge or have recently commercialized SIBs.[4] The SIB chemistry, however, still faces hurdles to overcome what hinders are more global production.[5]

Striving for longer driving ranges, shorter charging times and an overall price tag comparable to those for combustion cars, industry has become interested in lithium solid-state batteries. If the mass production of solid-state batteries is going to be successful, their high energy density could address these goals.[6]

A successful mass production, however, is for now unclear as many of the current issues on cell level and upscaling are yet not resolved. The industrial big players in the research on lithium solid-state batteries are for now start-ups in the USA such as Quantumscape or Solid Power that are heavily invested in by big car companies such as VW, Ford and BMW.[6] Academia has started its research by the development of sodium de- and intercalation layered cathode material Na_xCoO_2 in 1981.[7] As for now, most sodium cathode materials are still transition metal oxides besides polyanionic compounds like sodium vanadium fluorophosphates or Prussian blue/white analogues. The discovery of hard carbons as anode material by Jeff Dahn's group,[8] reaching reversible capacities close to those of lithium insertion into graphite, gave a major boost for competitive thinking in terms of lithium- vs. sodium-ion batteries.

Industrially, Na-SSB have not yet reached the scope of the big battery players, but if lithium SSBs manage to reach mass production, the transition to sodium will be faster than from liquid to solid electrolyte[6] and have the advantage of a reduced cost and higher abundance of the battery materials, as lithium has significantly gone up in cost.[2] The cathode active materials for Na-SSBs are similar to those used in SIBs with liquid electrolyte and are as of now primarily transition metal oxides.[4] Na-SSBs enable the use of sodium metal with a decreased dendrite formation compared to liquid electrolytes while increasing energy density significantly. Therefore, sodium metal is the most common choice, however, increasing work has been conducted on alloy anodes.[9,10] The solid electrolytes studied at present are sulfide/selenide, halide, oxide and *closo*-borate electrolytes with conductivities of up to 40 $mS \cdot cm^{-1}$ surpassing those of liquid electrolytes.[11,12]

The use of solid electrolytes in sodium batteries offers several advantages. The possibility to use sodium metal as the anode, in contrast to graphite or hard carbons as used in commercialized lithium- or sodium-ion batteries, contributes significantly to the enhanced energy density. Moreover, the transference number t_{Na+} for inorganic solid electrolytes is close to unity, which means that the total current is transported by the cation without generating a concentration gradient as in liquid electrolytes, thus increasing the power density.[13]

In light of these factors, it is crucial to explore sodium batteries with solid electrolytes and address the key challenges remaining. By understanding the strong reactivity between electrolyte and electrode materials and tackling the mechanical issues, the way for the development of safer, more efficient, and higher energy-density sodium-based energy storage systems is paved.

In this work, I present a comprehensive exploration of various aspects related to Na-ASSBs. The findings are divided into two publications each focusing on specific aspects of the battery system.

Publication 1 titled "Protective NaSICON Interlayer between a Sodium–Tin Alloy Anode and Sulfide-Based Solid Electrolytes for All-Solid-State Sodium Batteries" studies the reaction of different sodium solid electrolytes with a sodium–tin alloy anode material. Specifically, the sulfide electrolytes Na_3SbS_4 and $Na_{2.9}Sb_{0.9}W_{0.1}S_4$ exhibit significant degradation at the anode|electrolyte interface. To address this

issue, we introduce a rigid ceramic $Na_{3.4}Zr_2Si_{2.4}P_{0.6}O_{12}$ disk as a protective interlayer between the anode and the sulfide electrolyte. This interlayer proves to be effective in maintaining stable impedance and protecting the sulfide electrolyte from decomposition.

Publication 2 titled “Halide and Sulfide Electrolytes in Cathode Composites for Sodium All-solid-state Batteries and their Stability” focuses on the reactions between different transition metal oxide cathode active materials and a sulfide and halide electrolyte. By studying these reactions, we aim to improve the understanding of the interfacial processes and identify strategies to enhance the performance and durability of sodium all-solid-state batteries.

Collectively, the results presented in this dissertation shed light on the challenges and opportunities associated with sodium all-solid-state batteries, particularly in terms of interfacial contact, conductivity and reactivity. The findings contribute to the ongoing efforts to develop efficient and reliable energy storage systems and provide valuable insights for future research in this exciting field.

2. Fundamentals

The fundamentals will provide a more detailed insight into current knowledge in literature. The topics addressed will be the concept of batteries and especially solid-state batteries in general, specifics such as ion transport, reactivity, pressure dependency of electrolytes, the working principles of alloys and reference electrodes as well as interfacial degradation and analytical methods to study them.

2.1. Sodium All-Solid-State Batteries

2.1.1. Architecture of all-solid-state batteries

An all-solid-state battery (ASSBs) is a type of rechargeable secondary cell that stores and releases energy through electrochemical redox reactions. It can be recharged using an external electrical potential or current. The key components of ASSBs include two electrodes (cathode and anode), a separator and two current collectors. In general the anode is the electrode that undergoes oxidation whereas the cathode is the electrode that undergoes reduction. In secondary batteries, though, the oxidation or reduction process at the electrodes depends on whether the cell is being charged or discharged. However, the terminology of the electrodes remains consistent, with “cathode” or “anode” consistently representing the electrodes whose reaction that takes place voluntarily, ergo during discharge. Consequently, the positive electrode is designated as the cathode whereas the negative electrode is identified as anode. In ASSBs, as in liquid electrolyte based cells, the cell voltage is determined by the difference in chemical potential of lithium or sodium between the two electrodes.

One distinctive feature of ASSBs compared to conventional lithium/sodium-ion batteries is the replacement of the separator and liquid electrolyte with a solid electrolyte. The solid electrolyte serves as both an electronic barrier between the electrodes and as an ionic conductor within the electrode composites and between electrodes, enabling efficient charge transfer.

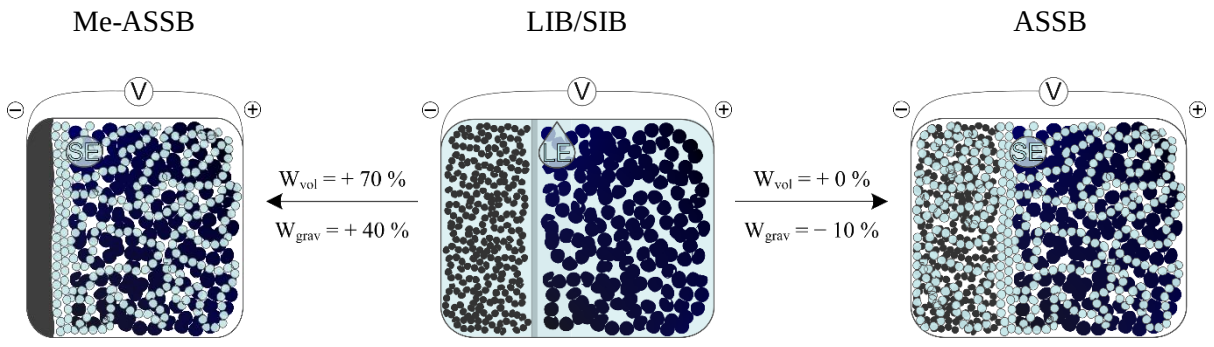

Figure 1: Architecture and changes of volumetric and gravimetric energy densities going from liquid based cells (LIB/SIB) to cells with solid electrolyte (ASSB) and cells with solid electrolyte and additionally a metal electrode (Me-ASSB).

Figure 1 adapted from Janek et al.[14] illustrates the changes in battery architecture when using solid electrolytes and when additionally using a metal anode instead of graphite/hard carbons or an alloy (not depicted in Figure 1). There are many positive aspects attributed to ASSBs, some of which are indeed quite obvious. 1. There is no concentration polarization within the electrolyte as the anions do not migrate.[15] The high transference number of close to 1 compared to liquid electrolytes with t_{Li+} of 0.4–0.6 enhances the overall battery performance.[16] 2. There is no need for ion desolvation, reducing the transfer resistance. 3. Solid electrolytes have a reduced flammability compared to liquid electrolytes. 4. The energy density is maximized by the ability to use metal anodes and bipolar stacking.[14]

However, several aspects related to ASSBs still require further investigation and validation. These include safety considerations, particularly concerning sulfide-based materials that release H_2S gas. Additionally, the safety implications of increasing energy density through the use of metal electrodes, which can react strongly with e.g. water, need to be thoroughly examined. Moreover, although many solid electrolyte materials show improved dendrite stability compared to liquid electrolytes, dendrite growth along grain boundaries is still a concern in certain material classes such as ceramics like NaSICON.

One of the inherent challenges in ASSBs is achieving good contact between solid components, which is currently addressed by applying pressure during battery assembly and cycling. Section 2.3 of this study shows the effect of electrolytes with low Young's modulus[17] facilitating the contact between the battery components and increasing the battery performance.

The field of ASSBs involves a wide range of material classes that operate with various working principles. These diverse materials offer compelling possibilities and opportunities for enhancing the performance and capabilities of ASSBs and are discussed below.

2.1.2. Solid electrolytes and the ionic transport

The transport of ions within the solid electrolyte strongly differs from liquid electrolytes. Since there is no gradient in charge carrier concentration and no diffusive and migrational fluxes of anions within a solid electrolyte, the electrical conductivity σ relates to the electric field $\vec{E}$ that is applied and results in a current density $\vec{J}$ according to Ohm's law.

$$\vec{J} = \sigma \cdot \vec{E} \tag{1}$$

In solid electrolytes, two different length scales are considered. An atomic scale in crystalline lattices and in the longer scale the impact of grain boundaries or pores can be distinguished.

The migration of sodium-ions in solid electrolytes on the atomic scale occurs with a hopping mechanism and can be calculated.[4] The place of a cation position within a lattice can either be occupied or vacant. The hopping of a sodium-cation from an occupied to a vacant position is one of the ion migration path-

ways within not only a solid electrolyte but any ion conducting crystal such as the cathode active material. The other migration possibility is the hopping of a sodium-ion to an adjacent occupied site by pushing that ion to the next vacant site. Especially for close to fully sodiated cathode active materials this is the way for ion diffusion. This migration is called correlated migration. The third transport mechanism is the interstitial migration when cations diffuse via interstitial sites which according to theoretical work, however, is not suggested to occur for the sodium ion migration.[18,19]

Considering the anionic framework of for instance Na_3PS_4, a sodium ion conductor, an additional contribution can lead to an increased conductivity. The so called "paddle-wheel" or "revolving door" is a dynamic rotational disorder occurring in the PS_4^{3-} tetrahedra that leads to an even faster migration of cations.[4]

The long range diffusion can be affected by migration through and along grain boundaries and by the presence of pores. Especially in oxide electrolytes, these phenomena play a crucial role where from the atomic scale, i.e. inside a perfect lattice, an ion pathway leads through intergranular regions, also called grain boundaries. These grain boundaries or intergranular regions do not constitute of a different "phase" but can have different mechanical and chemical properties. The heterogeneity in migration pathways can change the resistivity by creating a tortuous diffusion path and reducing the conductivity of the material or increasing conductivity along the grain boundaries.

Therefore, the minimization of pores, via i.e. densification, within a solid-state conducting material is essential. This densification can be established through different processes. Oxide electrolytes, so ceramics, have to be sintered at high temperatures whereas sulfide materials can be cold pressed, facilitating the preparation of composites.

One of the key aspects of ion conduction within electrolytes is its temperature dependence. The ion transport is a thermally activated process, causing the ionic conductivity to increase with temperature, which can be described by an Arrhenius-type equation:

$$\sigma_i(T) = \frac{\sigma_i^0}{T} e^{-E_a/k_B T} \tag{2}$$

where σ_i is the ionic conductivity, σ_i^0 the pre-exponential factor, T the temperature, E_a the activation barrier and k_B the Boltzmann constant.[20,21] When dealing with solid electrolytes, it is necessary to differentiate between the temperature dependence at the grain boundaries and in the bulk material. The magnitude of the grain boundary resistivity can change differently with temperature compared to the bulk resistivity and can, therefore, play an important role in the total ionic conductivity.[22] However, deriving from this equation it is evident that an elevation in temperature results in an overall increased ionic conductivity.

Many solid electrolytes like their liquid counterparts suffer from a lack of redox stability either at the anode or cathode side, which will be discussed in more detail in chapter 2.2.[14] A major benefit of ASSBs is, however, the ability to use multiple electrolytes, for instance, as a separator or catholyte according to the desired requirements. To sum up, a perfect solid electrolyte should have the following properties: a high ionic and low electronic conductivity, a wide voltage stability window and a low Young's modulus. The solid electrolytes studied at present are sulfide/selenide, halide, oxide and *closo*-borate electrolytes of which the following section will concentrate on those studied within this work.

Sulfide electrolytes

Sulfide electrolytes (SEs) studied for the lithium-ion conduction reach higher conductivities compared to liquid electrolytes and even exceed these conductivities when sodium sulfides where developed. The most commonly used sulfide electrolyte is Na_3PS_4. At present the $Na_{2.9}Sb_{0.9}W_{0.1}S_4$ SE with a conductivity of 40 $mS \cdot cm^{-1}$ shows the highest ionic conductivity reported for a sodium-ion conducting electrolyte. Key for the high ionic conductivity is A) the introduction of vacancies using aliovalent substitution with W^{6+} and B) the isoelectronic substitution of P with Sb as it lowers the activation barrier for the ion migration by widening the diffusion bottleneck.[11]

The major advantage apart from the sulfides high conductivity is their deformability, enabling to compensate for volume changes of the active material especially in the cathode. A consolidation/densification and usage of constant pressure throughout cycling is, however, essential as a crystalline sulfide-type electrolyte loses contact upon pressure release. This leads to pore formation and therefore a tortuous transport pathway resulting in a decreased effective ionic conductivity. The alternative of synthesizing amorphous sulfide-type electrolytes containing nanocrystallites has the advantage of an improved contact upon pressure release. However, the disadvantage is the decreased bulk ionic conductivity of these amorphous electrolytes.[23]

In terms of electrochemical stability this type of SE lacks the necessary voltage stability window[24] leading to the formation of interphases both at the anode side (reaction with sodium) and cathode side which will be further discussed in chapter 2.2.

Halide electrolytes

As a relatively new group of SEs, the challenges and capabilities of halide and especially chloride electrolytes have yet to be studied in depth. As for the sulfides, first studies have demonstrated an enhancement in ionic conductivity when using mechanochemical synthesis compared to SEs prepared through high-temperature synthesis.[25] The possibility to cold sinter them by compacting them[26] signifies a sufficient contact upon pressing and therefore a high softness, which is needed within the cathode composite. However, so far sodium chloride electrolytes show conductivities far below those of oxides and sulfides in the range of 10^{-5} $S \cdot cm^{-1}$. Their thermodynamic reduction stability was calculated to be insufficient

vs. Na^+/Na.[27] Also lithium-based halide electrolytes show a reduction instability,[28] leading to a mixed conducting interface, that is a constant grow of the reaction layer (see chapter 2.2). Lithium-based halides have, however, proven themselves to be very stable to oxidation[29] and the oxidative stability of the sodium counterpart will be further investigated in this work.

Oxide electrolytes

Only a few oxide electrolyte structures have been intensively studied, which are Na-β/β''-alumina and NaSICON structures.[30] Na-β/β''-alumina, which even as a polycrystalline material reaches ionic conductivities of up to 6 $mS \cdot cm^{-1}$, is already used in industry within the ZEBRA cell, which operates at high temperatures with molten sodium. NaSICON structures presented and studied in this work have been intensively studied but due to their rigidity not yet used in full cell applications. Even though NaSICON phases are predicted to be thermodynamically unstable against sodium, studies have proven that the formation of Na_3PO_4 on the surface[31] by adding an excess of sodium and phosphorus during the synthesis leads to a stabilization of the interface on contact with sodium. Oxide electrolytes offer high ionic conductivities and a wide voltage stability window,[24] are more resistant to contact with atmospheric gases than most electrolytes and show low charge transfer resistances at the interface with sodium. Major drawbacks are, however, the high temperatures necessary for densification of the oxides or co-sintering with the cathode materials, as this is costly and can also lead to unwanted reactions with the cathode, forming resistive interphases. Other than that, the lack of deformability especially in ASSBs causes mechanical issues upon manufacturing of thin layers and during cycling and volume expansion within the cathode which can cause cracking and delamination of the rigid SE.

2.1.3. Cathode active material

Within cathode active materials (CAM), this work will only focus on transition metal oxide (TMO) intercalation materials. During discharge, sodium ions intercalate into oxygen–transition metal slabs reducing the transition metals and vice versa during charge. TMO cathodes are high voltage materials, causing problems with the stability voltage window of many electrolytes. They are mixed ionic/electronic conductors and have to be used within a composite with an ionic (solid electrolyte) and mostly also electronic conductor (carbon). For ASSBs, the morphology, particle size, the volume expansion and cracking of the cathode active materials during charging and discharging play the most important role as the solid materials lack the good contact compared to liquid electrolytes.[32] A good TMO cathode active material should, other than that, show high capacity, reversible de-/intercalation of sodium ions and no degassing during cycling. The particle size and size distribution is to this point highly discussed, see Minnmann et al.[33]

Lithium and sodium TMOs display distinct variations in their voltage profiles during intercalation and deintercalation of the corresponding cation. Figure 2 presents exemplarily the voltage profiles of $NaCoO_2$ and $LiCoO_2$, where $NaCoO_2$ demonstrates several distinct voltage plateaus, signifying multiple individual phases, while $LiCoO_2$ shows a rather gradual phase transition. The size of the sodium-ion accounts for these variations. Upon extraction or insertion of the large sodium-ions, the TMO framework undergoes ordering phenomena, without breaking the transition metal–oxygen bond.[34] The type of transition that occurs determines whether irreversible changes take place in the structure, resulting in a loss of capacity. The most common structures are P2- und O3-type phases with P (prismatic) and O (octahedral) being the coordination sites for the sodium-ions within the lattice and 2 and 3 being the repeated stacks of oxygen layer in the crystal structure. The type of phase is primarily determined by sodium content (via synthesis or cycling) but also by the transition metal and/or synthesis condition. Generally, the prismatic sites enable a faster ion diffusion, however, P2-type phases have diminished sodium content ergo less capacity.

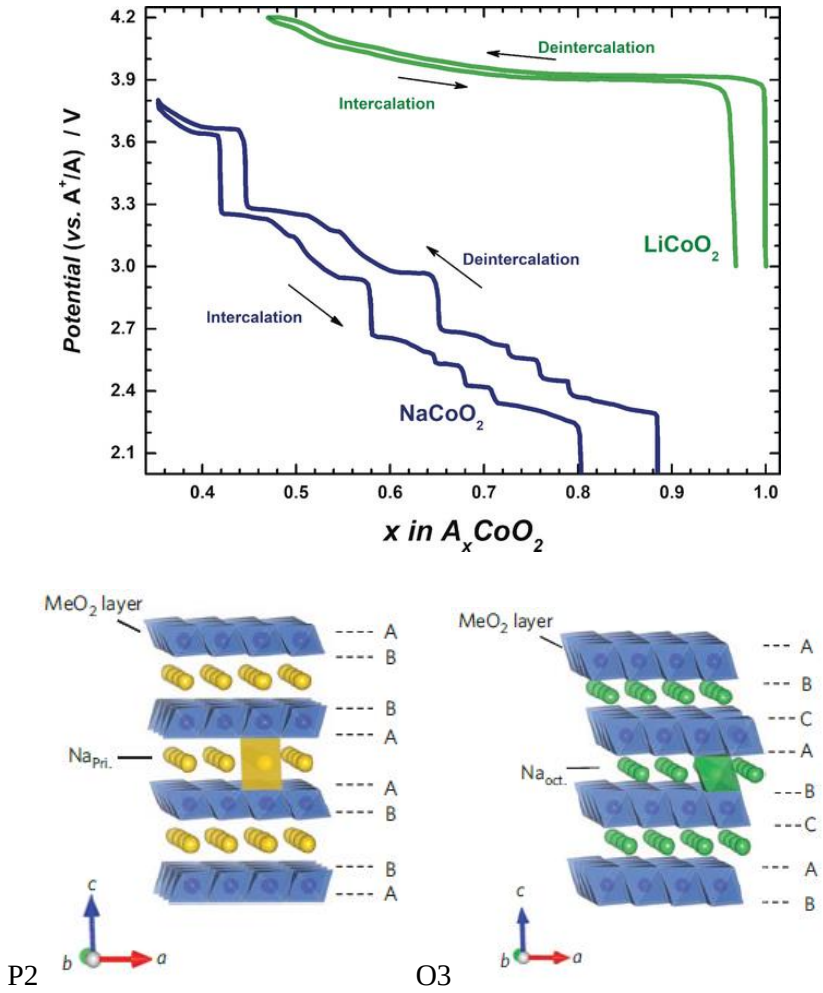

Figure 2: Comparison of $NaCoO_2$ and $LiCo_2$ voltages profiles reprinted with permission from Nayak et al.[35] and $NaMeO_2$ (Me= metal) phases P2 and O3 reprinted with permission from Yabuuchi et al.[36]

The TMO intercalation CAM used within this work is foremost P2-$Na_{0.66}Fe_{0.4}Mn_{0.5}Mg_{0.1}O_2$. The unsubstituted O3- and P2-$Na_{0.66}Fe_{0.5}Mn_{0.5}O_2$ material has been originally studied by Yabuuchi et al.[36] but its

phase changes especially at high voltages remain a controversial topic. The substitution with magnesium reported by Yang et al.[37] does not only lead to a structural stabilization but the enlargement of the inter-layer spacing facilitates the sodium-ion conduction and has shown apart from its earth abundant materials good performance in liquid based cells.

2.1.4. Anode

As anode material for ASSBs, metal electrodes are highly discussed for their high energy density and reduced dendrite formation with solid electrolytes compared to liquid electrolytes. Sodium metal is a very soft material[38] which can lead to creep. One has to specify that creep in this case is the definition of a transport mechanism within the metal, which can be in fact beneficial as consistently metal will creep to the solid electrolyte|separator interface, enabling high current densities.[39] However, the softness of the sodium metal can also cause problems, particularly under pressure, which is required for contact in the cathode composite. The metal may be forced through a slightly porous solid electrolyte,[40] posing the potential issue of a short circuit. Furthermore, many solid electrolytes, especially sulfide electrolytes, are highly reactive with sodium metal. As an alternative, alloy materials can be used as anode material. They show increased mechanical and electrochemical stability. Many alloy materials experience, however, an even stronger volume increase than pure metal upon sodiation/lithiation causing contact issues within the ASSBs. Within this work, a sodium–tin alloy material was studied. Considering the Na–Sn binary phase diagram and the study of the sodium insertion and removal of a tin thin film by Ellis et al.[41] a suitable alloy material was chosen. The voltage curves within the work showed several distinct plateaus. One of which corresponds to a $Na_{15}Sn_4$–Na_3Sn two phase region which presented a potential of 0.2 V vs. Na^+/Na. It was chosen due to the lowest volume expansion and highest voltage difference to the cathode material, which signifies high capacity cells, without including sodium metal. The alloy material shows good mechanical properties and an increased stability towards the sulfide separator material as also verified in this work.

2.2. Alloy anode material

Alloy materials and especially the sodium–tin alloy are highly complex materials and a topic that has been widely studied but still not fully understood. The first section will be on the theory of alloys and the alloying principle and the second section on experimental observations and potential explanations.

An electrochemical alloying reaction of sodium with another metal occurs through the formation of a binary alloy with different stoichiometry in a stepwise manner:

$$x\mathrm{Na}^+ + x\mathrm{e}^- + \mathrm{M} \leftrightarrow \mathrm{Na}_x\mathrm{M}$$

Alloys, as they themselves are metals, are electronically conducting. The properties of an alloy, however, can differ from the individual metal(s) it is composed of. The introduction of metal atoms of one sort into the lattice of another leads to stress which can change its properties, especially mechanically. There are two alloying processes. Interstitial alloying occurs when very different sized metal atoms are alloyed and the smaller metal species rests in the interstitial positions of the atom structure of the other metal. During substitutional alloying, the atomic position of one metal atom is substituted by the other metal atom. In both cases the alloying leads to a large volume expansion creating issues especially in ASSBs.

The phase/phases formed throughout the alloying procedure can be extracted from the phase diagram, theoretically calculated through density functional theory (DFT) or for the sodium–tin alloy case constructed experimentally. Over the course of time different sodium–tin phase diagrams where determined that partially differ in the stoichiometry of the different phases. Figure 3 and Figure 4 show two different phase diagrams with the first one being the most recent one and the foundation of the future discussion.

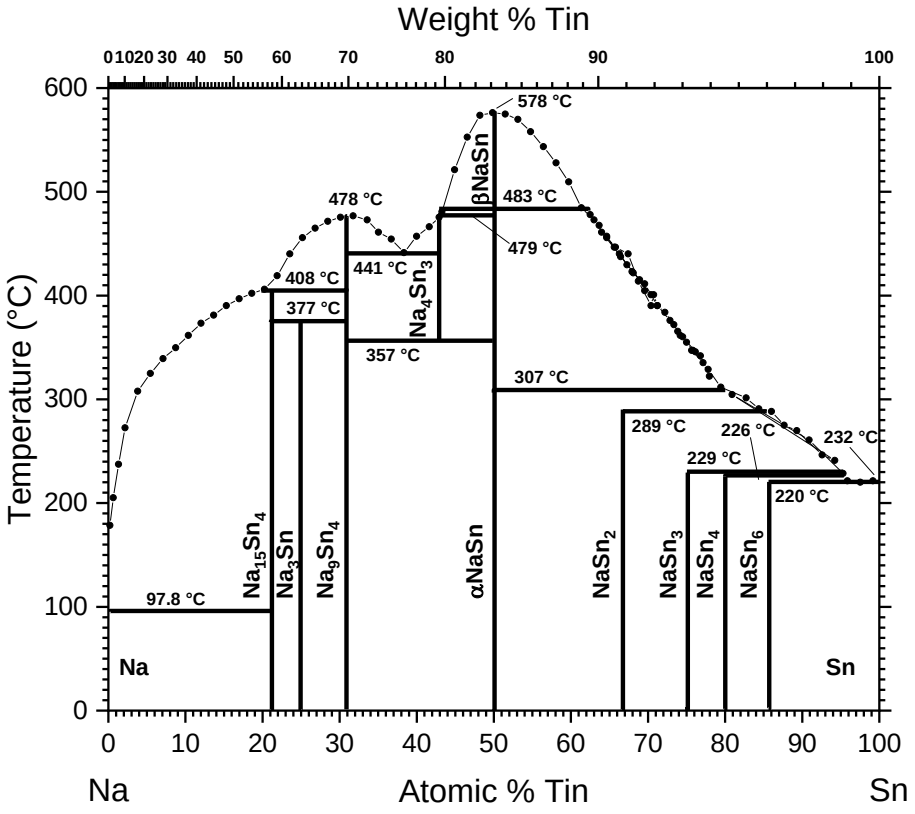

Figure 3: Sodium–tin phase diagram from 1998 digitalized and replotted.[42]

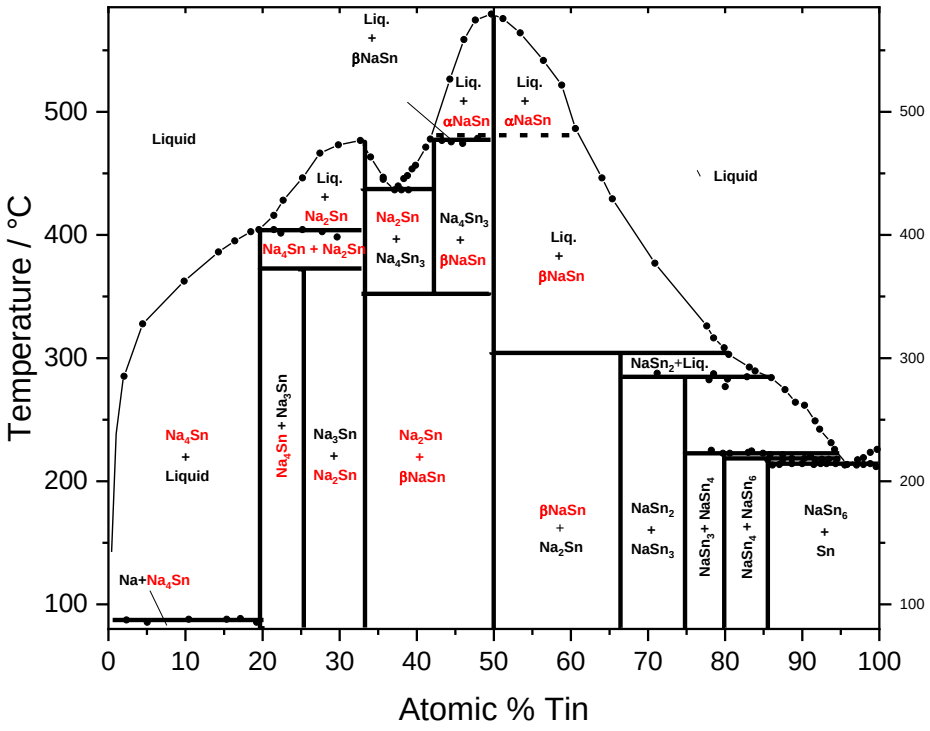

Figure 4: Sodium–tin phase diagram from 1928 digitalized and replotted.[43] The phases marked in red differ in stoichiometry or notation from the phase diagram from 1998 by Sangster et al.

Despite the established phase diagrams, in some cases, anodes made of alloys can follow a reaction path that differs from the equilibrium phase diagram.[4]

The alloying reaction of sodium–tin forms amorphous and metastable crystalline intermediates which are difficult to study with common characterization techniques.[44] Furthermore, the alloying of sodium–tin strongly depends on many parameters such as current density, cut off voltage, cycle number, thickness of the electrode, cell configuration and electrolyte.

The alloy material used in this work is synthesized mechanically. The ratio between sodium and tin, that was chosen, leads to an already sodium rich phase after synthesis. Therefore, the focus is put in the sodium rich phase(s) of the phase diagram being the two phase region $Na_{15}Sn_4$–Na, the $Na_{15}Sn_4$ phase and the two phase region $Na_{15}Sn_4$–Na_3Sn.

2.3. Electrode interfaces and degradation mechanisms

After cell assembly the interface from electrolyte to active material whether within the cathode composite or from separator material to anode material can experience several issues. High interface resistances can be caused by contaminants, voids or electro-/chemical instabilities.

Electrochemical instabilities

Both chemical and electrochemical instabilities lead to the formation of a solid–electrolyte interphase (SEI). The same phenomenon is called cathode–electrolyte interphase (CEI) at the cathode. In ASSBs, the term SEI may be misleading as solid electrolytes are used. However, similar to liquid cells, it represents the interfaces/interphases between electrolyte and electrode. The electrode|electrolyte interface or interphases can be categorized as follows: (1) If no reaction between the electrode material and the electrolyte takes place a stable interface is formed. (2) If a reaction between electrolyte and active material/electrode takes place and an interphase is formed, that has an ionic conductivity but no electronic conductivity, this interphase is called SEI/CEI. It will passivate and not grow indefinitely. (3) If a reaction between electrolyte and active material/electrode takes place and an interphase is formed that has ionic and electronic conducting properties it is called mixed conducting interphase (MCI) and grows consuming the electrolyte. This characterization has mainly been used for metal anode materials but equally applies for the interface between SE and CAM, current collector or carbon.

The electrochemical decomposition of a SE occurs primarily due to its narrow thermodynamic stability window. For the representation of the electrochemical stability window for liquid electrolytes the highest occupied molecular orbital (HOMO) and lowest occupied molecular orbital (LUMO) used to be considered, as spread to the battery community by Goodenough.[45] Equivalently, for the SEs, the conduction band (CB) and the valence band (VB) have been considered.[46] The theory was that if the CB minimum/VB maximum has a higher/lower energy then the anode/cathode material the solid electrolyte would be stable. However, this approximation only considers electrons. The example of the redox stability of water being 1.23 V vs. the HOMO–LUMO energy gap (E_g) of 8.7 V supports this misconception.[47] It neglects the energy contribution of the ion, which, in case of an instability, will leave the electrode like the electron due to charge neutrality.[47] It is, therefore, only a first approximation which only provides an upper limit. The stability window can be calculated through quantum mechanical calculations. If the lowest/highest energy ($-e[E_{\text{Oxidation}}]/-e[E_{\text{Reduction}}]$) of the stability window is calculated to be lower/higher than the electrochemical potentials of the anode/cathode ($\widetilde{\mu}_{e^-,\text{Anode}}$ /$\widetilde{\mu}_{e^-,\text{Cathode}}$) it degrades and forms an interphase at the electrodes.[4,45] This occurs when the formation of an interphase is not hindered kinetically. Figure 5 illustrates an electrochemically unstable solid electrolyte, where the stability window is not determined by the CB or VB of the electrolyte.

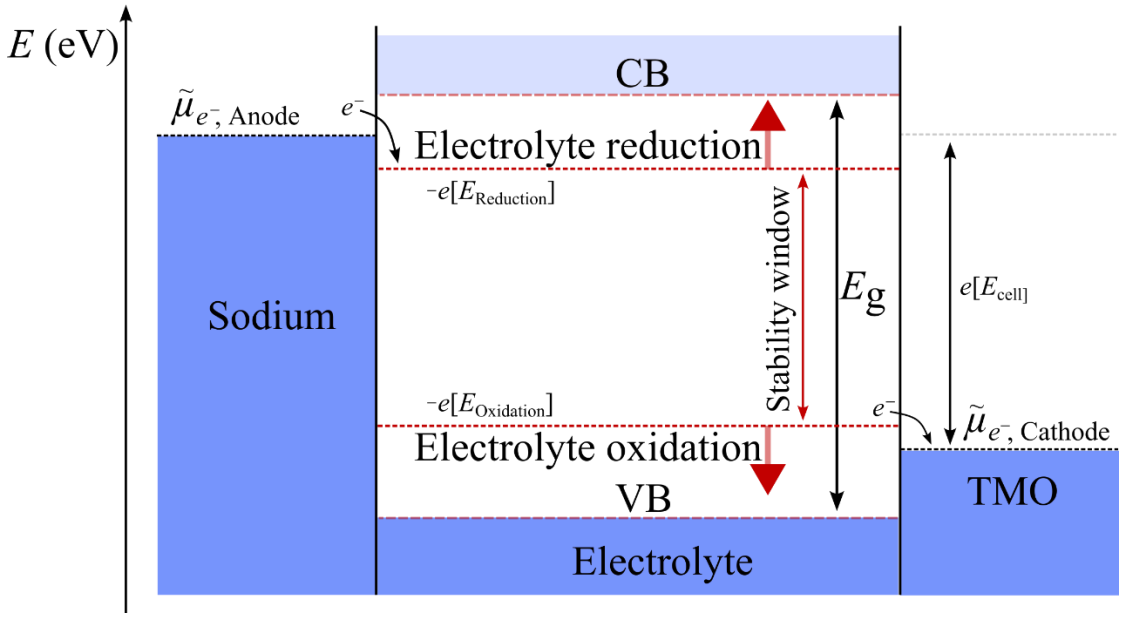

Figure 5: Schematic illustration of the energies of the electrolyte stability window adapted from Peljo et al.[47] Depicted are the valence band (VB) in dark blue and conduction band (CB) in light blue of the solid electrolyte and the electrochemical potential of the anode ($\tilde{\mu}_{e^-,Anode}$), here sodium, as the reductant and the electrochemical potential of the cathode ($\tilde{\mu}_{e^-,Cathode}$) here a transition metal oxide (TMO) as the oxidant. The stability window with an upper energy limit ($-e[E_{Reduction}]$) and a lower energy limit ($-e[E_{Oxidation}]$) is smaller than the cell voltage ($e[E_{cell}]$) which signifies a reduction/oxidation of the electrolyte if no stable SEI is formed at the interface.

Considering the work by Lacivita et al.[24] the reduction stability of NaSICON was calculated to be 1.11 V vs. Na^+/Na. The reaction with sodium, however, showed kinetic limitations due to the formation of a stable SEI. This explains why NaSICON materials with a stability window including low voltages are used at the anode side. NaSICON forms decomposition products with high voltage cathode materials. For the material with a slightly higher phosphorus content $Na_{3.4}Zr_2Si_2PO_{12}$ vs. $Na_{3.4}Zr_2Si_{2.4}P_{0.6}O_{12}$ the oxidative stability was calculated to be 3.41 V vs. Na^+/Na.[48] The oxidative decomposition products were calculated to be $ZrSiO_4$, O_2, SiO_2 and $Zr_2P_2O_9$.

To the knowledge of the author no calculations were performed for the precise composition of $Na_{2.4}Er_{0.4}Zr_{0.6}Cl_6$. Nevertheless the halide electrolyte Na_3MeCl_6 with Me = Er exhibits a structural similarity and calculations revealed a high voltage window ranging from approximately 0.5 V to 4 V vs. Na^+/Na.[49] Even though it lacks stability with sodium metal, it shows great oxidative stability. Furthermore, the material $Na_{2.25}Y_{0.25}Zr_{0.75}Cl_6$ (NYZC) with yttrium instead of erbium[50] also shows a stability window at comparably higher voltages and is successfully used in composites with high voltage cathodes. An insufficient anode stability for that NYZC halide is reported by Deysher et al.[27]

Sulfide electrolytes show an overall small stability window as shown by Tian[51] or Lacivita.[24] For the reaction of Na_3SbS_4 with sodium metal, a chemical instability has been calculated,[52] forming Na_2S and Na_3Sb which upon cycling leads to the formation of Sb[53] at the anode. As Na_2Sb and Sb are mixed

conducting materials, a MCI is formed degrading the electrolyte continuously. At the cathode, a chemical instability forming Sb_2S_3 and S is calculated.

A decomposition of the solid electrolyte forming a stable SEI/CEI, however, can be partially reversible if the appropriate potential range during cycling is chosen. Considering that most decomposition products are poor ionic conductors, an irreversible decomposition leads to a local increase in resistance at the SE|electrode interface. This in turn leads to a decrease in partial ionic conductivity within the composite, a high overpotential reducing the "real" state of charge (SOC) of the active material from cycle to cycle and hence decreasing the ASSB cell performance.

Chemical reactions

Even if not electrochemically induced, interfaces can still undergo chemical reactions over time or temperature. Literature on lithium sulfide electrolytes by Park et al.[54] state that most SE interface reactions with the current collector or the carbon additives derive from the presence of functional groups on the surface. These functional groups are –OH groups, carbonates and water residuals.[55] As these functional groups are limited, it can be assumed that most decomposition products at these interfaces are primarily formed through electrochemical decomposition. At the SE|CAM or the SE|anode interface, however chemical reactions can take place with or without additional functional groups as been heavily studied not only for lithium SSBs[56–59] but also sodium-containing solid|solid interfaces.[24,60]

A key issue that has to be considered is that experimental evidence of chemical reactions is often hardly distinguishable from electrochemical degradation as analytical methods can induce damage and decomposition.

The electrochemical and chemical reactions mentioned in this chapter lead to mostly undesired products which with a few exceptions lead to resistive interlayers. As mentioned above, these resistive interlayers impede sodium-ion transport and lead to a decrease in cycling performance.

Protective layers

Protective interlayers can be used if chemical or electrochemical reactions take place between the electrode material and electrolyte as described above. With the usage of a protection layer, two new interfaces are formed. One from the protection layer towards the electrode material and one towards the electrolyte. Even though they do not necessary need to form a stable interface as described above, they should, however, at least form a stable interphase. Fundamental considerations for an appropriate coating, as well as coating methods and various material classes successfully used in lithium-based ASSBs are discussed by Culver et al.[61] Derived from coating materials and strategies for Li-ASSBs[62] as well as study on coatings for cathode materials for SIBs,[63–66] research has recently found interest in coatings for Na-ASSBs.[67]

2.4. Chemo mechanical effects and mechanical considerations for all-solid-state-batteries

In ASSBs, composite cathodes are employed due to inadequate ionic and electronic conduction of most cathode active materials. These composite cathodes comprise three components: an electron-conducting material (e.g. carbon), an ion-conducting material (SE) to facilitate contact with each redox-active particle, and a mixed-conducting material for cation diffusion within the particle.

There are three main issues associated with cathode composites. The first issue as mentioned above is the consumption of charge carriers during the formation of a CEI. The second issue arises during the fabrication process of cathode composites, where the establishment of an efficient diffusion pathway is crucial. This requires achieving a homogeneous distribution of particles within the cathode through proper mixing and distribution procedures, as well as attaining the optimal volumetric ratio of SE/CAM/Carbon for efficient cycling.[68,69] The third issue is the potential disruption of the percolation network in the cathode due to volume expansion of the active material during intercalation, cracking of the SE or insufficient distribution.

The issues apart from chemical or electrochemical instabilities at the anode can be equally chemo-mechanic. Poor contact and void formation during stripping can lead to high transfer resistances. Furthermore, the void formation during stripping can lead to an increased current flow at the remaining contact points, facilitating dendrite growth during plating.

To overcome these issues, it is essential to ensure a void-free and stable interface between the cathode composite materials as well as the separator electrolyte and the anode. If instabilities are present, a coating may be necessary. The solid electrolyte should possess sufficient flexibility/softness to compensate volume changes of the rigid cathode active materials. Additionally, the application of external pressure is required to ensure good contact during cycling. Alternatively, zero-strain cathode materials such as vanadium phosphates can be used, which, however, have lower capacities and are not addressed in this work. Lastly, achieving homogeneous mixing, as described earlier, is essential to address these challenges.

2.5. Reference electrode

A method to study the aforementioned causes for capacity fading is the incorporation of a reference electrode (RE). The necessity for a RE in battery cells lies in the fact that two-electrode measurements can hardly separate contributions from the cathode or anode. These contributions often overlap in measurements such as impedance measurements. In battery cell testing for cells with liquid electrolyte the

use of REs is already very common. For the use in ASSB, however, the construction and positioning of the RE are the greatest challenges. Introducing a RE to a SSB cell without changing the cell geometry significantly, has been established by Hertle et al.[70]

The RE used within this work is a tungsten wire with a gold coating which is covered by a tin layer representing the RE. To be correct this electrode is actually a pseudo-reference electrode. What is meant by that is, that a "real" reference electrode must have a defined potential, which is known without being measured in the system, and alternatively carry the same charge carriers as the electrode to which it refers. To create a real RE an *in situ* sodiation of the tin wire could be performed. In this work a stable potential for the sodiated tin RE was, however, not reached. Reasons could be that the phase diagram of sodium–tin shows several voltage plateaus during alloying. For fabrication and geometry reasons the amount of tin throughout the wire is a) not completely homogeneous and b) fairly low. This can lead to fast changes of phases while alloying. Furthermore, a reaction of the newly forming alloy during sodiation of the tin alloy with the electrolyte could result in the depletion of sodium in the wire. The as mentioned reasons could lead to the unstable potential of the RE. The most important point for a RE, however, is a stable potential. This stable potential is reached in this work for an unsodiated tin electrode as can be seen in the supporting information of Publication 1. The fact that the potential of the RE only reaches a stable potential with time can be attributed to slow kinetics of the alloying at the surface of the RE or rather the SEI formation.

More generally, the concept of a "pseudo" reference electrode is explained in the following. Considering first of all a symmetric sodium ion battery cell with a RE and liquid electrolyte (LE). Upon current flow one of the sodium metal electrodes oxidizes releasing sodium-ions and an electron:

$$\mathrm{Na} \rightleftharpoons \mathrm{Na}^{+} + \mathrm{e}^{-} \tag{3}$$

The open circuit potential of the two sodium electrodes can be described by the Nernst equation:

$$E(\mathrm{Na}) = E^{0}(\mathrm{Na}) + \frac{RT}{zF}\ln\left(\frac{a(\mathrm{Na}^{+})}{a(\mathrm{Na})}\right) = const \tag{4}$$

If the RE is a non-sodiated electrode such as a tin electrode, the following reaction can occur upon contact with the LE:

$$\mathrm{Sn} \rightleftharpoons \mathrm{Sn}^{n+} + n\mathrm{e}^{-} \tag{5}$$

And at the same time due to charge neutrality and with respect to the phase diagram (see Figure 3), at the same electrode:

$$n\mathrm{Na}^{+} + n\mathrm{e}^{-} + m\mathrm{Sn} \rightleftharpoons n\mathrm{NaSn}_{6} + (m - 6n)\mathrm{Sn} \tag{6}$$

The open circuit potentials of these reactions are:

$$E(\mathrm{NaSn_6}|\mathrm{Sn}) = E^0(\mathrm{NaSn_6}|\mathrm{Sn}) + \frac{RT}{zF}\ln\left(\frac{a(\mathrm{Na^+})}{a(\mathrm{NaSn_6})}\right) \tag{7}$$

$$E(\mathrm{Sn}) = E^0(\mathrm{Sn}) + \frac{RT}{zF}\ln\left(\frac{a(\mathrm{Sn}^{n+})}{a(\mathrm{Sn})}\right) \tag{8}$$

However, they are not defined since the activity α of the sodium on the tin electrode and the activity α of the tin ions with the electrolyte is not known and very low and arises from impurities on the electrode. The following reaction can takes place during sodiation of the reference wire:

$$\mathrm{Sn} + n\mathrm{Na^+} \rightleftharpoons \mathrm{Sn}^{n+} + n\mathrm{NaSn_6} + (m - 6n)\mathrm{Sn} \tag{9}$$

Combining the potentials from equation (7) and (8) leads to the following voltage:

$$\Delta E = \Delta E^0 + \frac{RT}{zF}\ln\left(\frac{a(\mathrm{Na^+})a(\mathrm{Sn})}{a(\mathrm{NaSn_6})a(\mathrm{Sn}^{n+})}\right) \tag{10}$$

If the activity is high enough to induce a reaction such as alloying of the sodium into the reference tin electrode, a stable but unknown potential vs. the two sodium electrodes is expected.

These assumptions are valid for cells with LEs. For solid electrolytes, two additional aspects have to be taken into account. Considering that SEs do not have a charge charrier concentration gradient this would imply that a depletion of sodium ions at the RE|SE interface occurs, creating additional voids and changing the hopping mechanism of the ion migration. As this depletion can only be marginal due to charge neutrality, this phenomenon would only occur at the RE|SE interface and since the activity is low this will not change the overall bulk conductivity of the electrolyte. Considering that for charge neutrality the tin ions would have to "diffuse" into the electrolyte, the probability of a side reaction at the interface forming the stable but undefined potential is very likely.

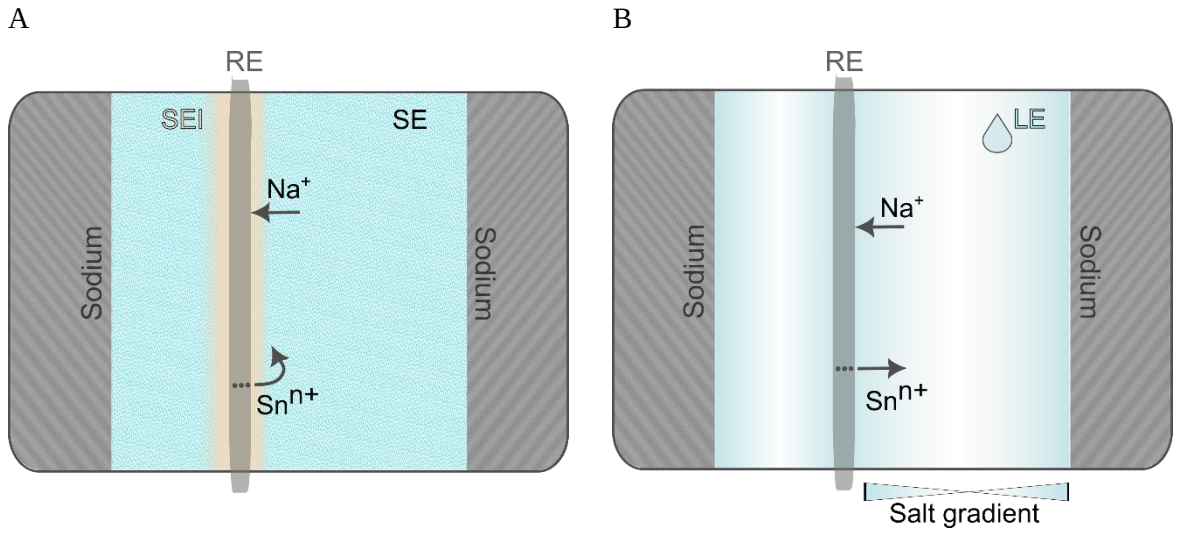

Figure 6: A) Representative symmetric sodium all-solid-state battery cell with a tin reference electrode, two sodium electrodes, a solid electrolyte (turquoise). The interphase area (light orange) here labelled

solid electrolyte interface (SEI) at the reference electrode that must be depleted from sodium ions and enriched with Sn^{n+} ions. B) Representative symmetric sodium ion battery cell with a reference electrode, two sodium metal electrodes, a liquid electrolyte (light turquoise) with an increased concentration of ions at the electrochemical double layer.

2.6. Analytical tools and their limits for sodium solid-state battery studies

2.6.1. Electrochemical Impedance Spectroscopy

Electrochemical impedance spectroscopy is a powerful tool to measure non-destructively *in situ* changes in the resistance of the studied probe. However, the interpretation of the retrieved impedance data necessitates a good knowledge of the studied system. The more complex the system the more information intermix which can create false conclusions. Even if the processes contributions to the impedance cannot be resolved, a quantitative analysis of the spectrum can serve diagnostic purposes giving insight into changes of the probe. This chapter will provide helpful information to understand the use of the impedance measurements within this work.

During an impedance measurement, a small periodic sinusoidal voltage signal is applied to a system. It is essential that the system remains stable throughout the course of the measurement to accurately measure the relationship between the signal and the response. If a degradation process is, however, studied, this is not given. Especially for a long signal input, ergo low frequencies, the sample can a) experience changes on its own which are then difficult capture and b) might be influenced by even the long input time.

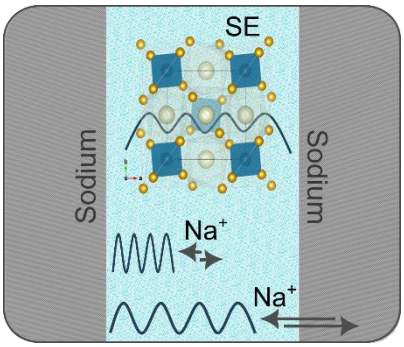

Figure 7: Exemplary sketch of a symmetric cell setup with the crystal structure of the used sulphur based solid electrolyte and the hopping mechanism of the Na^+ ions. The upper and lower wave represent the sinusoidal voltage signal input upon impedance measurement with high (upper) and low (lower) frequencies. Additionally the representative trajectory of Na^+ ions in one wavelength is symbolised by the arrows explaining a stronger influence of the cell with low frequency.

Apart from degradation processes, also open voltage relaxation after current flow can lead to significant changes within a measurement, especially at low frequencies. The appropriate amount of relaxation time until the system reached an equilibrium has to be added after current flow and prior to the impedance

measurement. Depending on the voltage drop this, however, signifies that the resistance measured is not necessary the one of the cell at the moment the current was stopped.

Upon cycling and consecutive impedance measurements after each charge and discharge step, not only the aforementioned degradation products or contact losses can change the impedance but the state of charge alters the resistance as well. Reason is the hopping probability on sodium-ions in the electrode material. TMO intercalation CAMs are synthesized in the sodiated state. A galvanostatic intermittent titration technique (GITT) where sodium ions are removed from the active material and reinserted step-wise can clearly show this phenomenon. The sodium-ions within the lattice are kinetically hindered and with increasing depletion hopping gets easier. Once a threshold is reached the hopping mechanism slows down due to the deficiency of available sodium-ions for hopping.

Three electrode impedance measurements

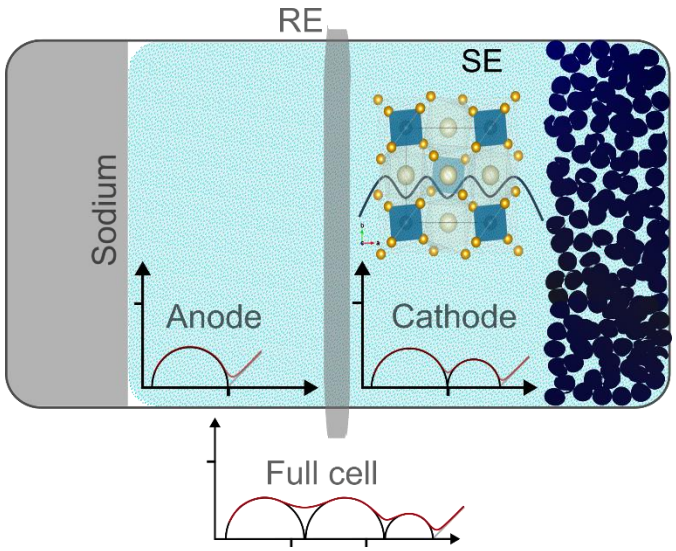

Figure 8: Exemplary sketch of reference full cell with included impedance spectra. The anode in this example would only have a contribution from the SE|Anode interface with an additional offset due to the bulk SE resistance. The cathode impedance is depicted with an offset due to the bulk SE resistance and at least 2 additional contributions, e.g. SE|CAM interface and constriction.

Apart from three electrode measurements, the separation of processes can be achieved by changing the samples to a measurable extent. This can be the thickness of a layer, the use of either blocking or non-blocking electrodes or via the use of temperature as certain processes have different activation energies.

The processes described within this work are

a) Interfaces – fitted by a R-CPE element (R = Resistor, CPE = Constant Phase Element).
b) Interphases – fitted by two R-CPE elements if the bulk resistance of it cannot be resolved.
c) Diffusion – fitted by a CPE, as anomalies such as electrode morphologies lead to values that differ from the −0.45° for the classical Warburg element used to fit diffusion.
d) Electronic conductivity – fitted by an R-CPE element if ion blocking electrodes are used or R if electronic blocking electrodes are used.

e) Ionic conductivity of solid electrolytes – fitted by an R-CPE element if ionically blocking and by an R if non-blocking.

The latter process is a good example of why single measurements can hardly give enough information to extract all information from a single impedance spectrum. Knowledge of the impedance of the bulk solid electrolyte from Figure 9A can give valuable information for fitting a spectrum of a symmetrical cell with additional electron conducting electrodes. The interface between the SE and sodium can hence be determined more precisely.

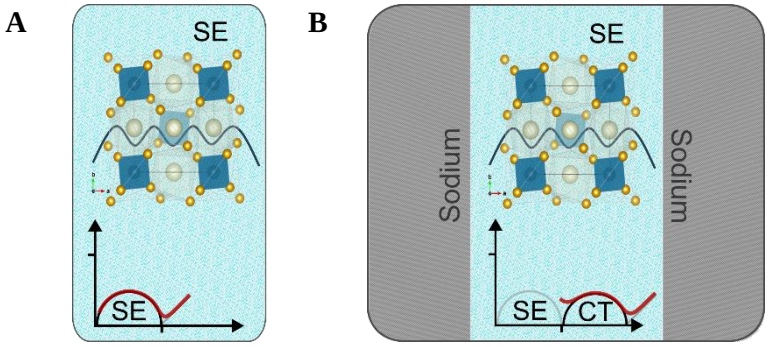

Figure 9: Comparison of impedance measurements of a SE electrolyte with electron blocking electrodes giving the clear magnitude of the resistance and the behavior in a cell with non-blocking electrodes. The measurement with blocking electrodes can be used to fit the impedance of the symmetrical cell where only the contributions from the charge transfer between the electrodes and the SE is visible.

2.6.2 Surface analysis via XPS, ToF-SIMS, EDX

Figure 10 clearly shows that some of the analysis techniques used within this work (coloured) are more suited to detect degradation products at the interface than others. Whereas X-ray diffraction (XRD) can detect structural changes the detection limit for most interface reaction products is too small. X-ray photoelectron spectroscopy (XPS) and time-of-flight secondary ion mass spectrometry (ToF-SIMS) analysis with a resolution suitable for interface reactions are surface sensitive methods that can expand their penetration depth via sputtering. Depending on the material, the energy input during sputtering can generate enough energy to cause reactions and may falsify the analysis of degradation products caused through chemical or electro-chemical reactions prior to analysis. Sputtering a reference material can be one method to avoid these pitfalls. In ToF-SIMS analysis, the collision cascade can introduce fragments that are typical of degradation products, which in the individual reference materials would not be detected. Therefore, trends between two samples of the same composition, such as a cycled and an uncycled composite, can strongly indicate whether the detected fragment is a reaction product or induced by the collision cascade. For a comprehensive overview of the constraints associated with the investigation of cathode composites via XPS and ToF-SIMS, the dissertation by Felix Walther is to be consulted.

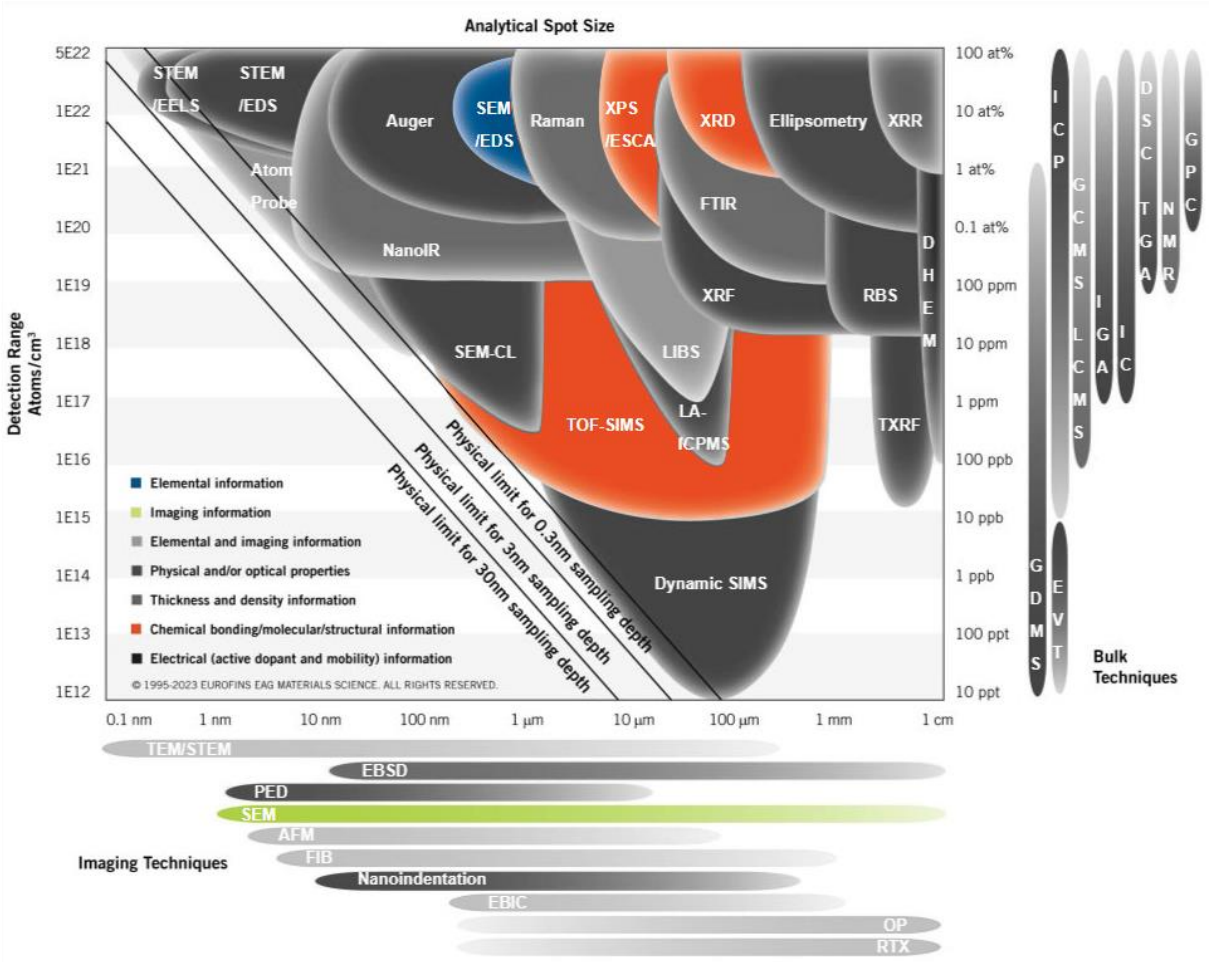

Figure 10: In colour, the analysis techniques – ToF-SIMS, XPS, XRD, SEM, energy-dispersive X-ray spectroscopy (EDS or abbreviated EDX in this work) – used within this work to study *in situ* and post mortem degradation processes, structural and morphological properties. Modified from © Eurofins Scientific (www.eurofinsEAG.com)

Together with SEM imaging, energy-dispersive X-ray spectroscopy (EDX) is a fast and easily available analysis technique to retrieve elemental information of a sample. The penetration depth of the incident beam is dependent on the voltage. The higher the voltage, the deeper the information can be extracted from the material by the incident beam. The elemental information is dependent on the energy that is released in form of X-rays, also called radiation energy, that the relaxation of an electron from an outer shell to an inner shell emits. This relaxation takes place as an electron hole is filled where an electron was ejected by the incident beam. Elements such as zirconium with 2.042 eV for the L_α radiation and phosphorus with 2.013 eV for the K_α radiation have close to identical radiation energy and are therefore hardly distinguishable. To detect the K_α radiation energy of zirconium one would have to increase the incident beam voltage to more than 15.776 kV which would increase the penetration depth and decrease the resolution significantly. It is therefore not possible to distinguish between a surface layer of Na_3PO_4 or $Na_xZr_yP_zO$ by EDX analysis, the relevance of which will be demonstrated in the first publication.

3. Results and Discussion (Publications)

At the beginning of this work studies on full cell sodium all-solid-state batteries have been scarce. The individual cell components such as solid electrolytes, cathode active materials for liquid based cells as well as alloy materials, however, had been increasingly researched. As the lithium solid-state battery counterpart has attracted increasing interest even in industry the case study for the more complex sodium system became the aim of this work.

The two following chapters introduce the two publication providing the base for this doctor thesis. They each lay focus on different parts of the sodium all-solid-state battery both studying primarily the interface reactions via analytical and electrochemical methods. The first publication sheds light on the reactions at the interface of sulfide-based solid electrolytes and oxide-based electrolytes with sodium metal or a sodium-tin alloy anode, primarily in half cells. The second publication emphasizes on the cathode side and the reactions at the interface with sodium oxide cathode active materials with sulfide-based or halide-based electrolytes.

3.1. Protective NaSICON Interlayer between a Sodium–Tin Alloy Anode and Sulfide-Based Solid Electrolytes for All-Solid-State Sodium Batteries (1st Publication)

In this publication the strong capacity fading of a full cell with the configuration Na–Sn|Na_3SbS_4|$Na_{2.4}Er_{0.4}Zr_{0.6}Cl_6$:$Na_{0.66}Fe_{0.4}Mn_{0.5}Mg_{0.1}O_2$:C65 is investigated. One of the reasons is the reaction of the sulfur-based electrolytes Na_3SbS_4 and $Na_{2.9}Sb_{0.9}W_{0.1}S_4$ with the sodium-tin anode studied via impedance spectroscopy and X-ray photoelectron spectroscopy. The introduction of an oxide-based NaSICON solid electrolyte between the sulfide separator and the anode leads to a blocked degradation inducing a stable resistance. However, the NaSICONs mechanical rigidity and at the same time the need to apply high pressure, to ensure a good contact within the cathode, does not lead to an increased cycling stability.

The experiments presented in this publication were designed and executed by the first author under the supervision of F. H. Richter and J. Janek. P. Till synthesized the sulfide electrolytes, Rietveld-refined the Na-Sn material and fitted all remaining XRD data with Pawley-fits obtaining the lattice parameter and space group under the supervision of W. G. Zeier. N. Nazer synthesized the cathode active materials and prepared a reference liquid electrolyte cell provided in the supporting information for the $Na_{0.66}Fe_{0.4}Mn_{0.5}Mg_{0.1}O_2$ cathode active material under the supervision of P. Adelhelm. M. Bhardwaj synthesized the NaSICON disks and provided the cross section SEM image as well as the density characterization in the supporting information under supervision of F. Tietz.

This study was part of the NASEBER project funded by the BMBF.

Reprinted with permission from L. E. Goodwin, P. Till, M. Bhardwaj, N. Nazer, P. Adelhelm, F. Tietz, W. G. Zeier, F. H. Richter and J. Janek. Protective NaSICON Interlayer between a Sodium–Tin Alloy Anode and Sulfide-Based Solid Electrolytes for All-Solid-State Sodium Batteries, *ACS Appl. Mater. Interfaces*, **2023**, 15, 50457-50468, DOI: 10.1021/acsami.3c09256.

ACS APPLIED MATERIALS & INTERFACES

www.acsami.org Research Article

Protective NaSICON Interlayer between a Sodium–Tin Alloy Anode and Sulfide-Based Solid Electrolytes for All-Solid-State Sodium Batteries

Laura E. Goodwin, Paul Till, Monika Bhardwaj, Nazia Nazer, Philipp Adelhelm, Frank Tietz, Wolfgang G. Zeier, Felix H. Richter, and Jürgen Janek*

Cite This: *ACS Appl. Mater. Interfaces* 2023, 15, 50457–50468 Read Online

ACCESS | Metrics & More | Article Recommendations | Supporting Information

ABSTRACT: This paper presents a suitable combination of different sodium solid electrolytes to surpass the challenge of highly reactive cell components in sodium batteries. The focus is laid on the introduction of ceramic $Na_{3.4}Zr_2Si_{2.4}P_{0.6}O_{12}$ serving as a protective layer for sulfide-based separator electrolytes to avoid the high reactivity with the sodium metal anode. The chemical instability of the anodelsulfide solid electrolyte interface is demonstrated by impedance spectroscopy, X-ray photoelectron spectroscopy, and scanning electron microscopy. The $Na_{3.4}Zr_2Si_{2.4}P_{0.6}O_{12}$ disk shows chemical stability with the sodium metal anode as well as the sulfide solid electrolyte. Impedance analysis suggests an electrochemically stable interface. Electron microscopy points to a reaction at the $Na_{3.4}Zr_2Si_{2.4}P_{0.6}O_{12}$ surface toward the sulfide solid electrolyte, which does not seem to affect the performance negatively. The results presented prove the chemical stabilization of the anode-separator interface using a $Na_{3.4}Zr_2Si_{2.4}P_{0.6}O_{12}$ interlayer, which is an important step toward a sodium all-solid-state battery. Due to the applied pressure that is mandatory for battery cells with sulfide-based cathode composite, the use of a brittle ceramic in such cells remains challenging.

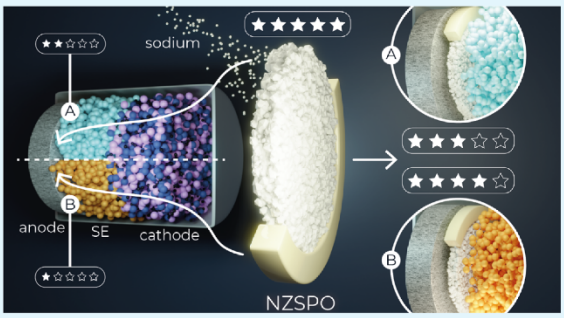

KEYWORDS: *NaSICON, NZSPO, solid electrolyte, sodium battery, all-solid-state battery, protection layer, anode, sodium tin*

INTRODUCTION

As the need for resource-efficient and sustainable electrochemical energy storage increases, the development of sodium-ion batteries with either liquid or solid electrolytes is pushed forward. One of the predominant questions in all-solid-state battery (ASSB) research is what type of electrolyte to use. As solid electrolytes are mechanically rigid, different electrolytes can be employed as, e.g., separator and catholyte without the risk of intermixing, thereby optimizing the cell function. Suitable solid electrolytes (SEs) must provide a high ionic and low electronic conductivity, a mechanical, chemical, and electrochemical stability, and must be safe to handle and use.[1] Sodium-based batteries are increasingly studied due to similar cell concepts compared to the lithium-ion battery (LIB), as well as the high elemental abundance of sodium and high energy density.[2−4] Sodium SEs can reach an ionic conductivity comparable to commonly used lithium or sodium liquid electrolytes.[5] They can be grouped into sulfides, oxides (including phosphates), halides, and *closo*-borates, among others.[6,7] The advantages of sulfide-type SEs such as $Na_{2.9}Sb_{0.9}W_{0.1}S_4$ are their mechanical softness and their potential to reach ionic conductivities $\sigma(Na^+)$ >10 mS·cm^{-1} at room temperature, making them highly attractive as SEs for composite cathodes. Their disadvantage is their strong reactivity with typical anode and cathode materials.[8] Chloride and oxide solid electrolytes are chemically more stable; however, oxides as typical ceramics feature high Young's and shear moduli,[9] and halides do not show sufficient ionic conductivities.[10] Borohydrides require an intricate synthesis procedure and are not easily available. At present, the most commonly used type of sodium SEs are NaSICON-phases (Na$^+$ SuperIonic CONductor) with the formula $Na_{1+x}Zr_2Si_xP_{3-x}O_{12}$, with $0 < x < 3$. The NaSICON-type $Na_{3.4}Zr_2Si_{2.4}P_{0.6}O_{12}$ solid electrolyte shows a high ionic conductivity but is a typical ceramic.[11]

For LIB, the most common anode material is graphite. The Na$^+$ ion ($r(Na^+)$ = 102 pm) has a larger ion radius than Li$^+$

Received: June 29, 2023
Accepted: September 18, 2023
Published: October 19, 2023

https://doi.org/10.1021/acsami.3c09256
ACS Appl. Mater. Interfaces 2023, 15, 50457−50468

($r(Li^+)$ = 76 pm), and its intercalation into the graphite layered structure has been perceived thermodynamically impossible.[12] Recently, studies have shown a method of cointercalation with solvent molecules, which, however, in a solid electrolyte battery is not applicable.[13,14] For sodium ASSB studies, sodium metal is used most commonly as the anode material.[11,15] The use of sodium as anode is most attractive for maximizing the energy density of the cell, but its application is difficult for the same reasons that are known from lithium. In particular, side reactions with the solid electrolyte and the formation of dendrites during charging remain key challenges. As an alternative, the use of sodium alloys is increasingly studied as anode material.[16−18] Elemental tin (Sn) as anode material experiences a volume increase of up to 525% during sodiation to $Na_{15}Sn_4$.[19] In addition, a partially irreversible sodiation occurs at the Sn anode in the first few cycles, leading to a sodium ion deficiency at the cathode and a subsequent loss of capacity.[20,21] This can be solved using a sodium−tin alloy as an anode starting material. Considering the phase diagram of sodium−tin and the work of Ellis et al.,[22] the two-phase couple $Na_3Sn/Na_{15}Sn_4$ (for the sake of simplicity, hereafter named as Na−Sn anode) offers a stable potential of 0.2 V vs Na^+/Na both upon sodiation and desodiation when used in sufficient excess. Passing the single-phase intermetallic $Na_{15}Sn_4$ during extended sodiation, the anode enters into a two-phase $Na/Na_{15}Sn_4$ mixture with a potential of 0 V vs Na^+/Na upon sodium ion intake. Using the Na−Sn anode, irreversible sodium uptake by the SE and SEI formation is reduced.[22] As synthesized by ball milling and consecutive grinding, the Na−Sn alloy is harder and less ductile than the sodium metal. The handling during cell assembly is therefore facilitated.

The highly conductive, soft sulfide-type SEs like Na_3SbS_4 are chemically unstable in contact with a sodium or sodium alloy anode at room temperature.[23] The formation of a resistive and ion-blocking interface caused by chemical decomposition can be detected with impedance measurements and X-ray photoelectron spectroscopy experiments.[24−26] The proposed solution to the above-mentioned problem is an interlayer of $Na_{3.4}Zr_2Si_{2.4}P_{0.6}O_{12}$ (NZSPO), which prevents the deterioration of the sulfide SE in contact with the sodium anode material. It consequently also minimizes the overpotential of the anode during cycling and improves the overall impedance of the whole cell.

In this work, we demonstrate improved stability and stable resistance using a NZSPO interlayer between the sulfide separator SE and the Na−Sn anode. We present the capacity fading of a cell of the type $Na-Sn|Na_3SbS_4|Na_{2.4}Er_{0.4}Zr_{0.6}Cl_6:Na_{0.66}Fe_{0.4}Mn_{0.5}Mg_{0.1}O_2$:C65 and the separate cathode and anode contributions to the impedance buildup using a three-electrode cell. Focusing on the anode contributions, we study the impedance increase over time due to SE decomposition when in contact with the Na−Sn alloy anode. The decomposition products forming at the anode|SE interface are resistive, which leads to a decreasing cycling performance. The focus of the paper is the stabilization of the resistance to avoid high overpotentials during battery cycling. For this purpose, a NZSPO interlayer is inserted at the anode|separator interface, which prevents the SE from decomposition. The successful combination of a ceramic SE with a relatively soft sulfide-based SE (which allows cold sintering of the cathode composite) in a press cell setup is one of the key novelties of this work. Supported by the impedance results, we prove that NZSPO is chemically stable toward both sodium and the sulfide SEs. An overview of the studied interfaces is given in Figure 1.

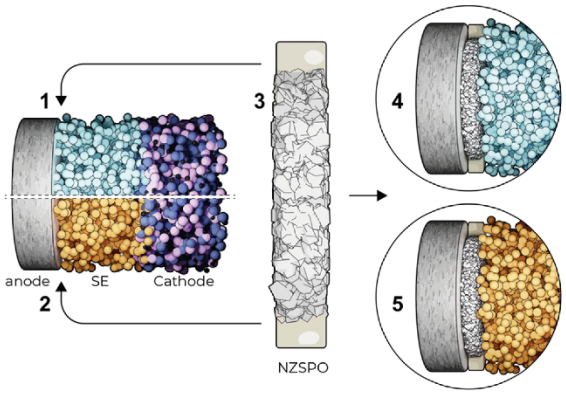

Figure 1. Representation of the studied interfaces in this work. Focus within the full cell was on (1) the anode (Na−Sn)|solid electrolyte (SE) Na_3SbS_4 interface and (2) the anode|SE $Na_{2.9}Sb_{0.9}W_{0.1}S_4$ interface. (3) Surface of NZSPO under in situ deposition of sodium. Interfaces and impedance behavior after insertion of a protective NZSPO interlayer between the anode (Na−Sn) and sulfur electrolyte (4) Na_3SbS_4 and (5) $Na_{2.9}Sb_{0.9}W_{0.1}S_4$, respectively.

METHODS/EXPERIMENTAL SECTION

The following materials were synthesized, as described in the Supporting Information: $Na_3Sn/Na_{15}Sn_4$, $Na_{2.4}Er_{0.4}Zr_{0.6}Cl_6$, $Na_{0.66}Fe_{0.4}Mn_{0.5}Mg_{0.1}O_2$, Na_3SbS_4, $Na_{2.9}Sb_{0.9}W_{0.1}S_4$, and $Na_{3.4}Zr_2Si_{2.4}P_{0.6}O_{12}$.

Cell Assembly. All cells were assembled in an argon atmosphere. A special cell casing was used to avoid water, nitrogen, or oxygen contamination and to maintain a constant pressure of 25 MPa, as described in a previous paper.[27] − (A) **Symmetric cells.** The symmetric cells for the electrolyte stability tests were prepared with 50 mg of Na_3SbS_4 or $Na_{2.9}Sb_{0.9}W_{0.1}S_4$ SE powder, respectively, which was compacted in a uniaxial press at 380 MPa for 3 min at room temperature in a polyether ether ketone (PEEK) cell casing with a diameter of 10 mm. For the cells without a protection layer, 50 mg of Na−Sn was added on each side of the SE and compacted with a uniaxial hand-press. The cell was consequently kept at a pressure of 25 MPa. A preparation scheme is presented in Table 1.

For the symmetric cells with a protection layer, two 1 mm thick and 0.94 mm high silicon O-rings were placed on each side of the pressed SE powder and filled with 30 mg of SE that is evenly distributed within the ring. Two NZSPO disks with a diameter of 8 mm and a thickness of 100−200 μm are then placed on top of each side of the solid electrolyte within the O-rings. Subsequently, each side is contacted with a stainless steel rod as the current collector. The

Table 1. Preparation Scheme for Symmetric Cells without the NZSPO Interlayer[a]

50 mg; 380 MPa		Hand-pressed and kept at 25 MPa
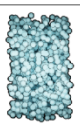	+ 2 x 50 mg Na-Sn	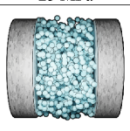

[a]The preparation with Na_3SbS_4 (here and hereafter illustrated in light blue) is also representative for the preparation with $Na_{2.9}Sb_{0.9}W_{0.1}S_4$.

https://doi.org/10.1021/acsami.3c09256
ACS Appl. Mater. Interfaces 2023, 15, 50457−50468

Table 2. Preparation Scheme for Symmetric Cells with the NZSPO Interlayer[a]

50 mg; 380 MPa		Hand-pressed and kept at 25 MPa		Hand-pressed and kept at 25 MPa
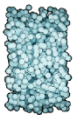	+ O-ring + 30 mg sulfide SE + NZSPO	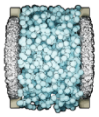	+ 2 x 50 mg Na-Sn	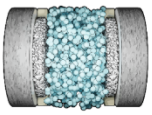
		Measurement 1		Measurement 2

[a]The preparation procedure for Na_3SbS_4 shown here in light blue is representative of the preparation procedure with $Na_{2.9}Sb_{0.9}W_{0.1}S_4$ (represented in yellow in the Results and Discussion section).

cell was loaded with 25 MPa, and impedance measurements were conducted. For the addition of the anodes, the stainless steel rods were removed, 50 mg of Na−Sn was evenly distributed on the NZSPO disk and the O-ring, the steel rods contacted again, and the impedance measurements were conducted. A preparation scheme is presented in Table 2.

The symmetric cell for the stability test of the anode potential was prepared with 50 mg of Na_3SbS_4 SE powder, compacted at 380 MPa for 3 min in a hydraulic press in a PEEK cell casing with a diameter of 10 mm. On one side, 20 mg and on the other side, 100 mg of Na−Sn were added onto the SE and compacted with a uniaxial hand-press. The cell was consequently kept at a pressure of 25 MPa. **(B) Na-ASSB cells.** Three Na-ASSB cell types were prepared. For each 50 mg of SE, Na_3SbS_4 or $Na_{2.9}Sb_{0.9}W_{0.1}S_4$, respectively, was compacted with a uniaxial hand-press in the same cell casing as described above. For the cathode composite, the NFMM, the NEZC, and an electronic conductor (C65, Imerys Graphite & Carbon Switzerland Ltd.) were mixed. The cathode composite (CC) was freshly prepared by mortaring a 100 mg batch with weight ratios of 66:30:4 of NFMM:NEZC:C65 for 20 min. 14 mg of CC were evenly distributed on the pressed SE separator, and the combination of separator and cathode was compacted in a uniaxial press at 380 MPa for 3 min at room temperature. Following this, we distinguish between the cell without (a) and with (b) a NZSPO interlayer. For cell type (a), 50 mg of Na−Sn was evenly distributed on the SE separator. For the cell type (b), a 1 mm thick and 0.94 mm high silicon O-ring was placed on the pressed SE separator and filled with 30 mg of SE that is evenly distributed within the ring. The 8 mm in diameter and 100−200 μm thick NZSPO disks are each placed on top of the solid electrolyte within the ring. Consecutively, 50 mg of Na−Sn was evenly distributed on the NZSPO disk and O-ring. All cells are contacted with stainless steel rods and compacted with a uniaxial hand-press, and the cell casing was kept at a constant pressure of 25 MPa. **(C) Three-electrode (3E) cell.** For the 3E cell, a reference electrode (RE) was prepared by the electrochemical deposition of tin on a gold-coated tungsten wire (Goodfellow, 10 μm in diameter). Therefore, 500 mg of Brij® 35 (an acid-resistant emulsifier), 60 mg of 4-diethylamino-benzaldehyde, and 4 g tin(II)sulfate were dissolved in 7 mL sulfuric acid, 4 mL of formaldehyde, and 100 mL distilled water. Tin foil with an area of 3 cm × 1 cm (thickness 0.127 mm, 99% Sigma-Aldrich) and a 5 mm long gold wire already attached to the peak inlet using Kapton tape was immersed into the solution. With a Biologic SP-200 potentiostat and a current of 450 μA, Sn was plated electrochemically onto the gold wire for 155 s to reach a thickness of 5 μm. The 3E cell with the described reference electrode was assembled according to Hertle et al.[28] by compacting 100 mg of SE separator (Na_3SbS_4) on both sides of the Sn-plated wire attached to a peak inlet, with a uniaxial hand-press. Subsequently, the steps of the cathode and anode addition are carried out as described for the Na-ASSB cells, including the loading with 25 MPa pressure. **(D) Three-electrode symmetric cell.** The RE as prepared for the 3E cell was also used in 3E symmetric cells. 100 mg of SE separator (Na_3SbS_4) was compacted on both sides of the RE attached to the peak inlet, with a uniaxial hand-press. Subsequently, 50 mg of Na−Sn was hand-pressed on each side of the Na_3SbS_4 separator, and the cell was constrained with 25 MPa pressure. The OCV was measured for 33 h with a break of 170 min after 15 h.

Electrochemical Impedance Spectroscopy. For all measurements, a potentiostat (BioLogic VMP 300, Seyssinet-Pariset, France) was used, and the RelaxIS 3 software package (rhd Instruments, Darmstadt, Germany) was used for fitting of the data. All measurements were conducted at 25 °C. The pressure loading of all cells was 25 MPa, using a spring to compensate for pressure relaxation due to the elastic deformation of individual components. An amplitude of 10 mV was chosen. For the symmetric cells and Na-ASSB cells, the current range was set to "auto," and the frequency range was 7 MHz to 10 mHz. The symmetric cells were assembled, and the impedance was measured over time (55 h). Impedance spectra were recorded immediately after cell assembly and repeated every 5 h. The Na-ASSB cell impedance was measured directly after cell assembly, after the first and second charge and discharge. For the three-electrode cell, two different connections were used to measure the impedance directly after cell assembly (pristine), after the first and second charge and discharge. For the measurement of the impedance between anode and cathode as well as the impedance of the cathode contributions, the cathode was connected as working electrode (WE), the anode as counter electrode (CE), and the Sn-plated wire as reference electrode (RE). For the anode contributions, the anode was connected as WE and the cathode as CE. For the latter, the current range was set to 10 mA. The frequency range for the measurements with RE was 200 kHz to 10 mHz.

Cell Cycling. Cycling was conducted at 25 °C and a constant pressure of 25 MPa using a Biologic VMP 300. For testing the electrolyte stability with symmetric cells, a unidirectional current of 24 $\mu A \cdot cm^{-2}$ was applied for 10 h. For testing the anode potential stability with symmetric cells, a unidirectional current of 24 $\mu A \cdot cm^{-2}$ was applied for 100 h, sodiating the 20 mg of binary $Na_3Sn/Na_{15}Sn_4$ phase. The Na-ASSB cells and 3E cells were charged to 4 V and discharged to 1.5 V with a current density of 24 $\mu A \cdot cm^{-2}$ for 20 cycles for the Na-ASSB cell and two cycles for the 3E cells. To enable relaxation of the cell prior to impedance measurements, intermittent open-circuit voltage (OCV) steps of 3 h for the Na-ASSB cell and 5 h for the three-electrode cells were added after each charge and discharge step. To charge with 0.01C, a theoretical capacity of 172 $mAh \cdot g^{-1}$ for the cathode active material was assumed.

X-ray Photoelectron Spectroscopy (XPS). During all measurements, the pressure in the XPS chamber was in the range of 10^{-7}−10^{-6} Pa, and the sample surface was charge-neutralized with slow electrons and argon ions. The transfer of the samples was conducted using a transfer shuttle, avoiding cross-contamination with oxygen from the glovebox to the analysis chamber. The samples were prepared in the same glovebox as for the cell assembly with oxygen and water content of $p(O_2)/p < 0.1$ ppm, $p(H_2O)/p < 0.1$ ppm. Data analysis was carried out with CasaXPS software.

Stability of Na_3SbS_4. XPS measurements in this section were conducted with a PHI Versaprobe 4 with a monochromatized Al K_α X-ray source (beam diameter 200 μm, X-ray power of 50 W). For the reference measurement, 50 mg of Na_3SbS_4 and Na−Sn were

https://doi.org/10.1021/acsami.3c09256
ACS Appl. Mater. Interfaces 2023, 15, 50457−50468

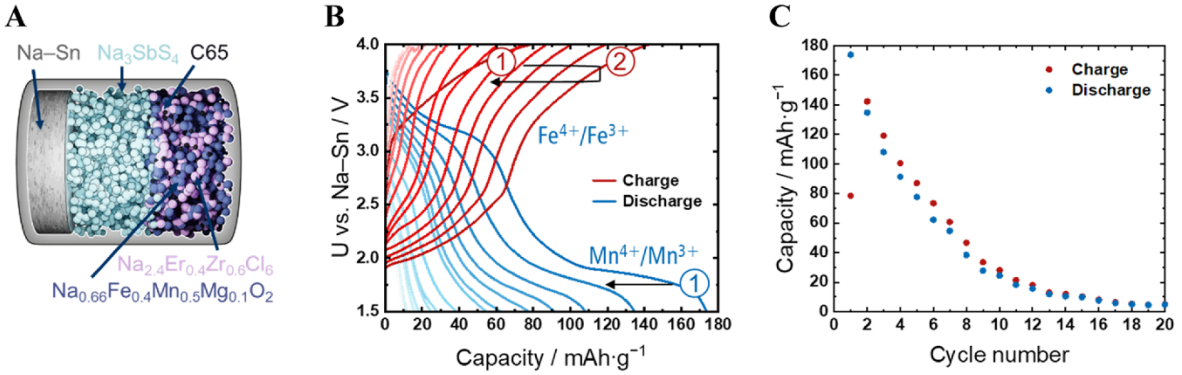

Figure 2. Cycling performance of a Na–Sn|Na_3SbS_4|NEZC:NFMM:C65 cell (A). Plotted are the cycling curves (B) and the corresponding capacities per cycle (C) for charging (red) and discharging (blue) steps at 0.01C between 1.5 and 4 V. The numbers in circles in graph (B) indicate the first and second cycle.

compacted in a powder sample holder cup made of PTFE with an inner diameter of 3 mm. For the stability test of Na_3SbS_4 vs Na–Sn, 50 mg of each powder was mixed and ground in a mortar for 10 min and compacted, likewise, in a powder sample holder cup. Pass energies were set to 27 eV apart from the Sb 3p signal, which was set to 55 eV for better intensity. The step size was 0.2 eV, and the step time was 30 ms. A sputter setting of 2 kV with a raster size of 2 mm × 2 mm was applied 10 times for 240 s each for Na–Sn as for the mortared Na_3SbS_4 with Na–Sn. The sputter step of 240 s was repeated 4 times for Na_3SbS_4.

In Situ Deposition of Sodium on NZSPO. XPS measurements in this section were conducted with a PHI 5000 Versaprobe II Scanning ESCA Microprobe (Physical Electronics) with a monochromatized Al Kα X-ray source (beam diameter 200 μm, X-ray power of 50 W). Experimental details for the *in situ* XPS technique have been reported by Wenzel et al.[29] Minor changes to the original technique are mentioned below. The analyzer pass energy for detail spectra was set to 46.95 eV, with a step time of 50 ms and step size of 0.2 eV. The sodium foil was prepared by cutting a piece of approximately 5 mm × 5 mm with a 1 mm thickness and bent over the L-shaped target holder. The mechanically soft sodium metal showed sufficient adhesion. A NZSPO disk was attached to the sample holder by using double-sided adhesive tape. The angle between the sputter gun and the sample surface was 33°. Sputtering of the sodium foil was performed using an acceleration voltage of 4 kV, 20 cycles with 3 min each. Before each sputtering step, a spectrum of NZSPO was measured to monitor spectral changes upon sodium deposition.

X-ray Diffraction (XRD). X-ray diffraction patterns of NEZC, NFMM, Na_3SbS_4, and $Na_{2.9}Sb_{0.9}W_{0.1}S_4$ were recorded on the Empyrean Series 2 X-ray diffractometer by PANanalytic in reflection mode. The diffractometer operated with a monochromatic Cu Kα X-ray beam with wavelengths of λ_1 = 154.06 pm (Kα_1) and λ_2 = 154.44 pm (Kα_2). The measurements were carried out at an operation voltage of 40 kV and 40 mA. The step size was 0.026°, with 180 s per step. Kapton foil was used to protect the measured powders from oxidation. All obtained XRD data were analyzed using HighScore Plus and fitted with Pawley-fits. A weight fraction analysis of the P2 and O3 phases of the NFMM by Rietveld refinements was not possible since only unreliable fitting parameters were obtained due to overlapping and partially low-intensity reflections. The X-ray diffraction pattern of Na–Sn was recorded on the Empyrean 3 diffractometer by PANanalytic in transmission mode. The diffractometer operates with a monochromatic Mo Kα X-ray beam at a wavelength of 72 pm. The measurements were carried out at an operation voltage of 60 kV and 40 mA. The step size was 0.014°, with 38 s per step. The capillary used had a diameter of 0.5 mm and a glass thickness of 0.01 mm. The capillary was prepared in a glovebox and sealed with wax to avoid contaminations during measurement. A reference diffractogram of an empty capillary was measured to enable the subtraction of the background prior to refinement.

Scanning Electron Microscopy (SEM). The samples were investigated using a Merlin SEM instrument by Carl Zeiss. The reference electrode was measured with a 3 kV and 100 pA setting and an InLens Detector. A Leica transfer shuttle was used to transport the NZSPO samples from the glovebox to the SEM. Different adjustments were set to retrieve optimized imaging and are specified in the following. SEM images of NZSPO from the Na-ASSB cell after cycling were measured with a SE2 detector with 8 kV acceleration voltage and 2 nA emission current. SEM images of NZSPO from symmetric cells after current flow were measured with an InLens detector for the cell with Na_3SbS_4 and a SE2 detector for a cell with $Na_{2.9}Sb_{0.9}W_{0.1}S_4$, each at 3 kV acceleration voltage and 100 pA emission current. For characterization of the elemental distribution on the surface, energy-dispersive X-ray (EDX) spectroscopy measurements were conducted. Therefore, an X-Max 50 Silicon Drift Detector by Oxford Instruments was used, and the obtained data were analyzed with Aztec 3.2.

RESULTS AND DISCUSSION

The two-phase $Na_3Sn/Na_{15}Sn_4$ (Na–Sn) alloy used as the anode showed the expected specific reflections for $Na_{15}Sn_4$ in the XRD pattern (Figure S1). In view of the Na–Sn phase diagram and the very narrow phase fields of the binary phases Na_3Sn and $Na_{15}Sn_4$, the anode alloy will exist as either a $Na_3Sn/Na_{15}Sn_4$ or $Na/Na_{15}Sn_4$ two-phase mixture. In the first case, the potential will be 0.2 V vs Na^+/Na, and in the second case, it will be 0 V vs Na^+/Na. Thus, measuring a potential of 0.2 V is direct and unequivocal proof of the presence of Na_3Sn. As we do not see direct evidence for this phase in the XRD, we have to assume that it is amorphous, as previously reported in the literature[30,22] and is not detected by XRD.

Considering the sodium–tin phase diagram and the work of Ellis et al.,[22] the two-phase $Na_3Sn/Na_{15}Sn_4$ (Na–Sn) mixture with a potential of 0.2 V vs Na^+/Na can only take up a certain amount of sodium until it reaches the two-phase $Na/Na_{15}Sn_4$ mixture, which has the potential of 0 V vs Na^+/Na. To ensure a stable potential of 0.2 V vs Na^+/Na during cycling, the potential stability of the anode material was tested electrochemically (Figure S2). It revealed a stable potential throughout the course of 100 h, and for simplicity, the anode material is, as mentioned above, only noted as Na–Sn instead of the correct but rather long sum formula $Na_3Sn/Na_{15}Sn_4$.

https://doi.org/10.1021/acsami.3c09256
ACS Appl. Mater. Interfaces 2023, 15, 50457−50468

ACS Applied Materials & Interfaces www.acsami.org Research Article

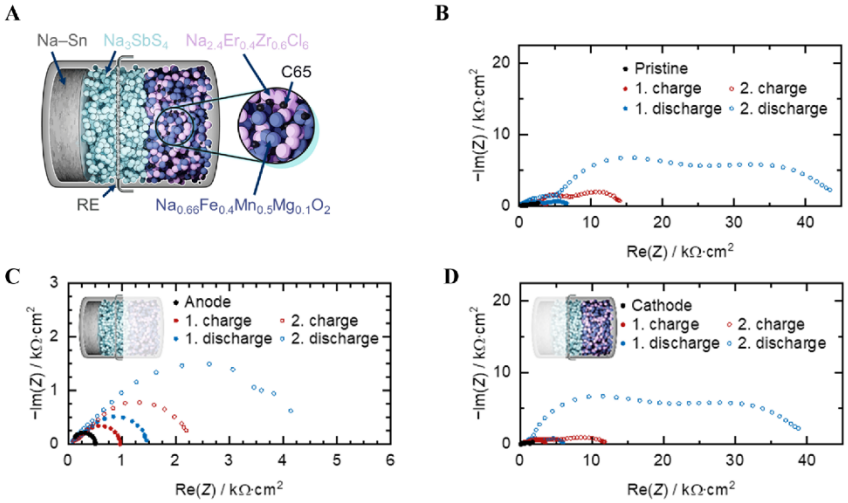

Figure 3. Impedance results of the Na-ASSB cell using a setup with RE as graphically depicted (A). Impedance spectra of the 3E cell (B), of the anode half-cell (C), and the cathode half-cell (D). The cells were charged and discharged twice. Impedance spectra were recorded in the pristine state of the cell (black), in the charged state (red), and in the discharged state (blue) with increasing resistance from first to second cycle.

The XRD patterns of the synthesized sulfide electrolytes Na_3SbS_4 and $Na_{2.9}Sb_{0.9}W_{0.1}S_4$, the NEZC catholyte, and the active material NFMM are shown in Figures S3–S6. The XRD studies of the electrolytes and active material did not reveal any secondary products or impurities, indicating that the impurities are less than 2–3 vol %, i.e., the XRD detection limit.

Capacity Fading of Na-ASSB Cells. For an overview of the cycling performance of the sodium ASSB, data of the cell type with Na_3SbS_4 as the separator are presented in Figure 2. The cycling curves for the cell, schematically presented in Figure 2A, are shown in Figure 2B. Corresponding impedance data for the pristine cell and after the first two cycles are shown in Figure S7.

The redox activity for the active material $Na_{0.66}Fe_{0.5}Mn_{0.5}O_2$ has been reported to be located at around 3.9 V for Fe^{4+}/Fe^{3+} and 2.0 V for Mn^{4+}/Mn^{3+} using cycling voltammetry.[31] The magnesium-substituted NFMM was already studied in cells with liquid electrolyte (Figure S8) and showed a redox activity at 3.5 V and at 2 V vs Na^+/Na, respectively, which corresponds to 3.3 and 1.8 V in our case if we assume a constant potential of 0.2 V for Na–Sn vs Na^+/Na. A more detailed electrochemical study of NFMM in cells with liquid electrolyte will be part of a forthcoming study. The two resulting redox plateaus are especially distinct during the first discharge. The Mn^{4+}/Mn^{3+} redox plateau fits well to the expected redox potential. However, Figure 2C shows the steady decrease of capacity with increasing cycle number, indicating deterioration phenomena, such as degradation reactions at the interfaces.

Separation of Anodic and Cathodic Contributions to Cell Failure Using a Three-Electrode Setup. In order to identify the origin of cell degradation and impedance increase in the above cell configuration, 3E measurements were carried out. The separation of anode and cathode contributions in the impedance measurement was enabled by adding a third (reference) electrode. As the electrode is a tin-coated gold wire and therefore does not contain Na^+ ions, it is, per definition, not a real RE, due to the lack of a defined redox couple. Experiments (Figure S9), however, revealed a stable potential vs Na–Sn and can be regarded as a pseudo reference electrode. For simplicity, the tin-coated gold wire is, as of now, only noted as RE instead of pseudo reference electrode. The electrochemical deposition and morphology of the tin coating can be seen in Figures S10 and S11, respectively. The impedance contributions of the cell with RE are presented in Figure 3.

The impedance data of the 3E cell served only diagnostic purposes and were not fitted. The anode resistance increases significantly during each charge/discharge step from ≈500 Ω·cm² in the pristine state to ≈4400 Ω·cm² after the second discharge. This is very likely due to severe decomposition of the sulfide SE at the anode/separator interface. Likewise, the cathode resistance increased with each cycling step. Compared to the anode side, where the impedance roughly doubled from the first to the second charge, the resistance at the cathode increased even more by about 400%, and the cathode resistance is, in general, much higher. The cathode and anode contributions add up well to the values measured in the full 3E cell (Figure S12), which demonstrates the proper function of the RE. The main contribution to the overall resistance of the 3E cell is caused by the cathode, as can be clearly seen when comparing the three impedance measurements (anode, cathode, 3E cell) after the second discharge (blue) in Figure 3B–D.

Chemical Instability of Na_3SbS_4 vs Na–Sn. XPS measurements were carried out to differentiate between electrochemical instability due to cycling and chemical instability of the Na–Sn|Na_3SbS_4 interface. Figure 4 shows the S 2p signal of a mixture of Na_3SbS_4 and Na–Sn. The reference spectra for Na_3SbS_4 and Na–Sn are provided in Figures S13 and S14.

The signal of Na_3SbS_4 is a doublet peak with a spin–orbit splitting of 1.18 eV[32] highlighted in turquoise. The strong decomposition reaction caused a doublet peak at lower binding energies, shown in light brown. A similar decomposition product forms for pristine Na_3SbS_4 during sputtering (Figure S13). The sulfur spectrum of the mixed materials before sputtering, however, already showed this side product, which proves a chemically unstable SE upon contact with the alloy

https://doi.org/10.1021/acsami.3c09256
ACS Appl. Mater. Interfaces 2023, 15, 50457–50468

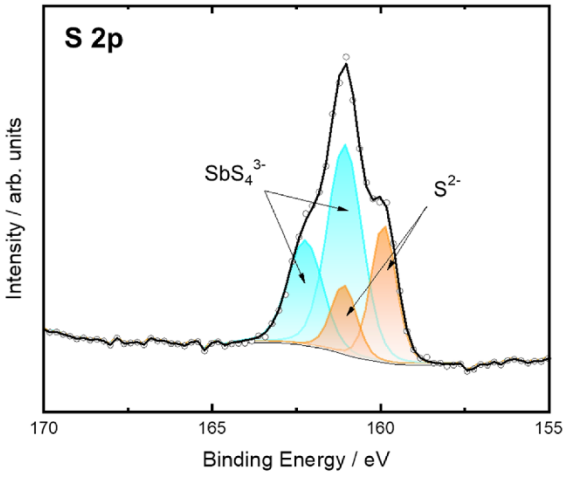

Figure 4. XP spectrum (S 2p range) of Na_3SbS_4 after grinding with anode material Na−Sn. The contribution from the unreacted SbS_4^{3-} is shown in a turquoise color. Degradation products indicative of the formation of Na_2S (S^{2-}) are shown in light brown.

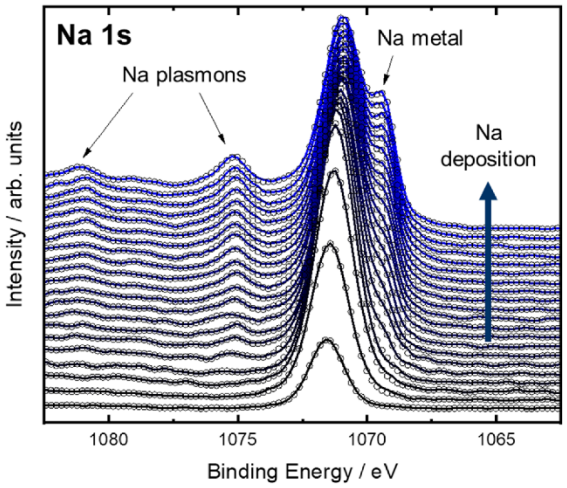

Figure 5. XP spectra of the Na 1s region evolving during sodium deposition on the NZSPO interlayer material.

anode. This phenomenon was already reported for an Na_9Sn_4 alloy.[26] In addition to Na_2S, reduced Sb or Sn compounds have thus to form. As we do not have sufficient analytical information to specify the reduction products, we refrain ourselves from hypothesizing about a specific degradation reaction. A reduction of Sb is difficult to observe since the Sb 3d signal strongly overlaps with the O 2p signal, and the Sb 3p signal has a low intensity, especially for mixed materials. In the case of tin, the Sn $3d_{3/2}$ peak overlaps with the Na KLL Auger lines. The Sn $3d_{5/2}$ peak shows three different chemical states for Na−Sn during sputtering. No additional chemical state is detected in the mixed materials but a different ratio of the peaks. That the surface of the Na−Sn material does not show any sign of Sn can be attributed to an oxygenated surface being the most probable Na_2O. The corresponding spectra are provided in Figure S15. Obviously, Na_3SbS_4 and Na−Sn react chemically as proven by XPS, and show additional electrochemical instability visible in impedance measurements during cycling.

Therefore, a NZSPO disk was introduced as an interlayer between the anode and the separator SE. In previous stripping experiments, NZSPO has already shown electrochemical stability against metallic sodium as well as sodium−tin alloys, and thus, is not reduced at low potentials.[9,33,34] By insertion of the relatively thick and 95% dense NZSPO interlayer, a model electrode/interlayer combination was formed that protects the promising sulfide SE from chemical decomposition. To investigate the applicability, chemical stability, and potentially improved stability of the sulfide electrolyte, the following tests were conducted.

Stable SEI of NZSPO Interlayer in Contact with Sodium Metal. To analyze the performance of the NZSPO disk toward the anode, *in situ* XPS measurements were carried out. As the Na−Sn alloy used as the anode material could not be deposited *in situ*, elemental sodium was used, which is even more reactive. A stable NZSPO interface during sodium deposition implicates a stable interface with the Na−Sn alloy. XP spectra of the NZSPO surface after sodium sputtering are presented in Figures 5 and 6.

Figure 5 shows the Na 1s signal during sodium deposition measured on the NZSPO. The initial peak originates from the Na^+ ions in $Na_{3.4}Zr_2Si_{2.4}P_{0.6}O_{12}$. With increasing deposition of sodium, as highlighted by the arrow, the characteristics of sodium metal are detected on the NZSPO disk. These are the plasmons at 1075 and 1081 eV, as well as the peak of sodium with an oxidation state 0 at a binding energy lower than the sodium peak with an oxidation state +1. Clearly, the sputtered sodium metal does not react continuously with the NZSPO, and thus forms a stable metal film on the NZSPO surface.

The silicon and phosphorus signals show no changes during deposition of sodium metal apart from the expected intensity decrease (see Figure S16). The zirconium spectrum, however, changes, as shown in Figure 6A,6B. The initial doublet peak with an expected spin−orbit splitting of 2.43 eV is located at 182.41 eV after calibration to carbon. The doublet peak shifts to higher binding energies during the first sodium deposition step. According to Maibach et al.,[35] this effect is related to the calibration on the C 1s adventitious carbon species. Due to surface effects, the binding energies of this carbon species shift and therefore alter the position of other surface species when calibrated to the C 1s signal. After covering the surface species and getting a constant signal for all species, the binding energy of the NZSPO surface is 182.76 eV. The zirconium double peak indicates a partial reduction of zirconium due to sodium deposition.

The intensity of the zirconium lines decreases with sodium metal deposition. The shoulder at lower binding energies, only absent in the first spectrum after deposition, indicates a reduced species and the formation of an SEI. The fact that the intensity of the SEI component does not increase with time confirms a stable SEI, as already reported in the literature by Ortmann et al.[36] Figure 6B highlights the overall changes, presenting the spectrum before deposition and the last spectrum after deposition.

Improved Stability of Na_3SbS_4 Separator with NZSPO Interlayer. The comparison of symmetric cells with and without a protection NZSPO interlayer showed a significant increase in stability. For symmetric cells with Na_3SbS_4 as a separator and without a protecting layer (Figure 7A), the

https://doi.org/10.1021/acsami.3c09256
ACS Appl. Mater. Interfaces 2023, 15, 50457−50468

ACS Applied Materials & Interfaces www.acsami.org Research Article

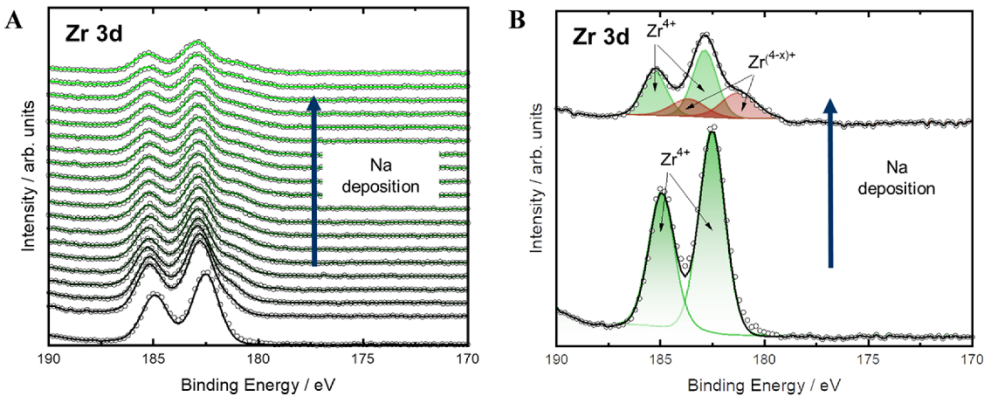

Figure 6. XP spectra of the Zr 3d region (A) evolving during the elemental sodium deposition, (B) before and after sodium deposition with the corresponding fit for the pristine Zr^{4+} signal and the evolving and stabilizing reduced species $Zr^{(4-x)+}$.

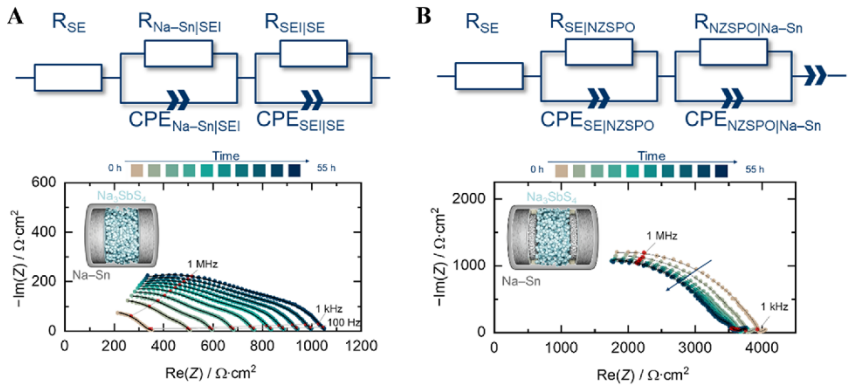

Figure 7. Impedance spectra of symmetric cells over time (55 h). The schematics of the cells show (A) the solid electrolyte Na_3SbS_4 (light blue) and the Na−Sn anode (gray) on both sides and (B) additionally the NZSPO disks (white) fixed with an O-ring (light yellow). The equivalent circuits for the impedance fitting are shown above. They consist of the resistance of the solid electrolyte (R_{SE}) and then two contributions, both fitted with a resistance connected in parallel with a constant phase element (CPE). For cell type (A), the interfacial resistance between the Na−Sn anode and the SEI and the interfacial resistance between the SEI and the SE are each represented by one (R)(CPE) element. For cell type (B), the interfacial resistance between the Na−Sn anode and NZSPO disk as well as the interfacial resistance between NZSPO disk and the SE are represented by one (R)(CPE) element each. Cell type (B) was additionally fitted with a constant phase element (CPE).

resistance increased over time (beige to blue). After 55 h, it is about 3 times higher compared to the state directly after assembly. The resistance of 39 Ω·cm^2 (Table S3) of the sulfide SE (R_{SE}) shifted the spectrum at the high-frequency side. The formation of an SEI layer due to decomposition of the electrolyte results in two contributions that shape the impedance. The contributions are the resistance between the Na−Sn anode and the SEI ($(R)(CPE)_{Na-Sn|SEI}$) and the resistance on the other side from the SEI toward the solid electrolyte ($(R)(CPE)_{SEI|SE}$). The corresponding two fitted semicircles and the data for equivalent circuits are shown in Figure S17 and Table S2. It can be noted that the resistances of the SEI|SE and Na−Sn|SEI contributions increase equally over time to reach a total impedance of 1053 Ω·cm^2 after 55 h.

The symmetric cell with Na_3SbS_4 solid electrolyte as a separator and a NZSPO protection layer has an overall higher but stable impedance (Figure 7B) of 3537 Ω·cm^2. The first two measurements after cell assembly (beige) and 5 h (light green) show higher overall impedances of 3954 and 3777 Ω·cm^2, respectively, than the following spectra (up to dark blue). This could be explained by an equilibration process that takes place after pressure has been applied. The resistance of the sulfide SE (R_{SE}) was fixed to 235 Ω·cm^2 as determined from impedance measurements of the cell prior to adding the Na−Sn electrodes (Figure S19 and Table S5). Reasons for higher resistances of the sulfide SE compared to the cell without the NZSPO layer are the exceeded amount of material used and the decreased density and therefore lower conductivity of the SE. The NZSPO resistance is negligible due to its high ionic conductivity of 3.5 mS·cm^{-1}. In the case of the insertion of the NZSPO layers, the contribution leading to the overall higher resistance is the interface resistance between NZSPO and the Na_3SbS_4 electrolyte ($(R)(CPE)_{SE|NZSPO}$) (see Figure S19). We assume that the interface resistance is high due to a constriction effect.[37] Once the interface contact is poor, the resistance of the contact points can be described by constriction resistances. According to $R_{Cstr} = \sum_i \alpha_i \cdot 1/\sigma_i$ with R_{Cstr} as the constriction resistance, α_i the activation parameter, and σ_i the conductivity, as described by Eckhardt et al.,[38] the constriction resistance depends on the conductivity of the lower conducting phase, i.e., Na_3SbS_4 in the present case. The contribution fitted with $(R)(CPE)_{NZSPO|Na-Sn}$ is the resistance

https://doi.org/10.1021/acsami.3c09256
ACS Appl. Mater. Interfaces 2023, 15, 50457−50468

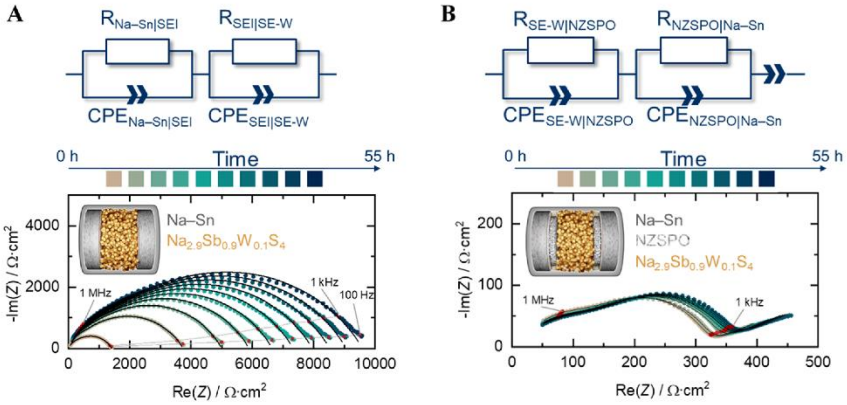

Figure 8. Time-dependent impedance spectra (up to 55 h) of the symmetric cells. The schematics of the cells show (A) the SE $Na_{2.9}Sb_{0.9}W_{0.1}S_4$ (yellow) and the Na−Sn anode (gray) on both sides, (B) additionally the NZSPO disks (white) fixed with an O-ring (light yellow). The equivalent circuits for the impedance fitting are shown above. They consist of two contributions, both fitted with a resistance connected in parallel with a constant phase element (*R*)(CPE). For cell type (A), the interfacial resistance between the Na−Sn anode and the solid electrolyte interface (SEI), as well as the interfacial resistance between SEI and the solid electrolyte SE are each represented by one (*R*)(CPE). For cell type (B), the interfacial resistance between the Na−Sn anode and NZSPO disk as well as the interfacial resistance between the NZSPO disk and the solid electrolyte are represented each by one (*R*)(CPE). Cell type (B) additionally was fitted with a constant phase element (CPE).

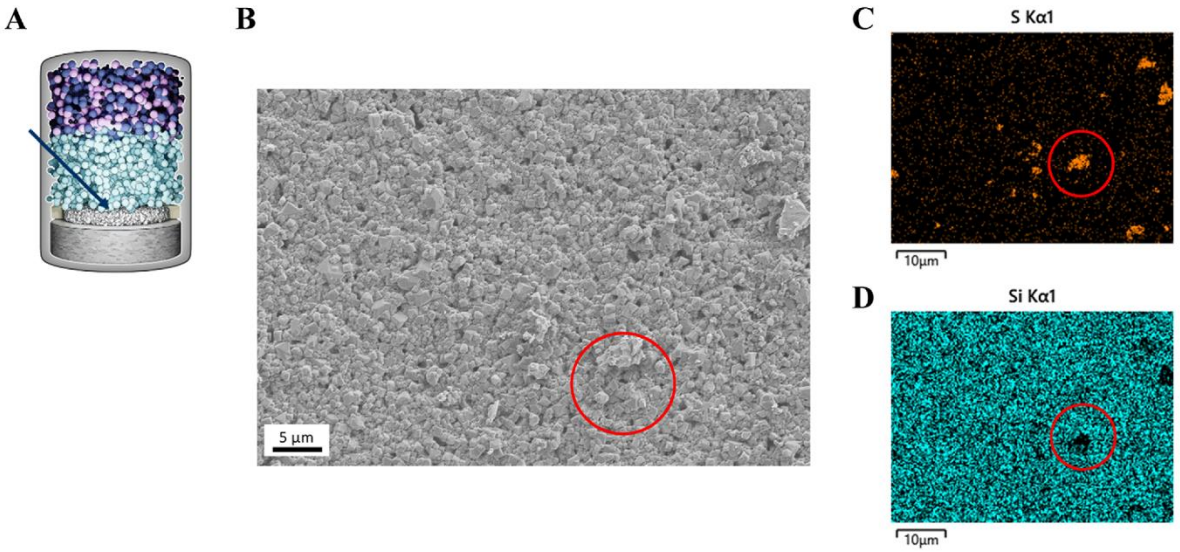

Figure 9. SEM image (B) and EDX mappings (C, D) of a NZSPO surface that was in contact with Na_3SbS_4 during cycling, as shown in schematic (A). The solid electrolyte Na_3SbS_4 is represented by the $K_{\alpha 1}$ line of sulfur, whereas the $L_{\alpha 1}$ line of silicon represents the NZSPO disk. The red circles show individual Na_3SbS_4 particles on top of the NZSPO layer.

of the interface between the anode material Na−Sn and the NZSPO disk, which is around 20 times smaller than the SEI NZSPO resistance. The last contribution has already been observed in garnet-type symmetric lithium cells as presented by Connell et al.[39] The roughness of the garnet, in this case, NZSPO, modifies the capacitive component of the low-frequency impedance[40] and is therefore fitted with an additional *CPE* element.

The stabilization of the impedance by inserting a NZSPO interlayer becomes even more apparent when studying the tungsten-substituted sulfide electrolyte $Na_{2.9}Sb_{0.9}W_{0.1}S_4$ as presented in Figure 8. This special sulfide SE reaches ionic conductivities of (41 ± 8) mS·cm^{-1} at room temperature and therefore represents a perfect candidate as a catholyte. However, in contact with the Na−Sn anode, $Na_{2.9}Sb_{0.9}W_{0.1}S_4$ decomposes rapidly, increasing the impedance drastically from 1415 to 9594 Ω·cm^2 in 55 h, as shown in Figure 8A. The first impedance measurement after cell assembly (Figure 8A, beige) already shows a higher resistance than the measurement of the symmetric cell with Na_3SbS_4 (Figure 7A). This phenomenon indicates a very fast and strong decomposition of the tungsten-substituted SE at the anode interface, resulting in the observed high impedance. With increasing time, the impedance rises, indicating a growing SEI. Compared to the cells without tungsten substitution, the equivalent circuit for modeling the spectra does not include a resistor for the electrolyte due to the

https://doi.org/10.1021/acsami.3c09256
ACS Appl. Mater. Interfaces 2023, 15, 50457−50468

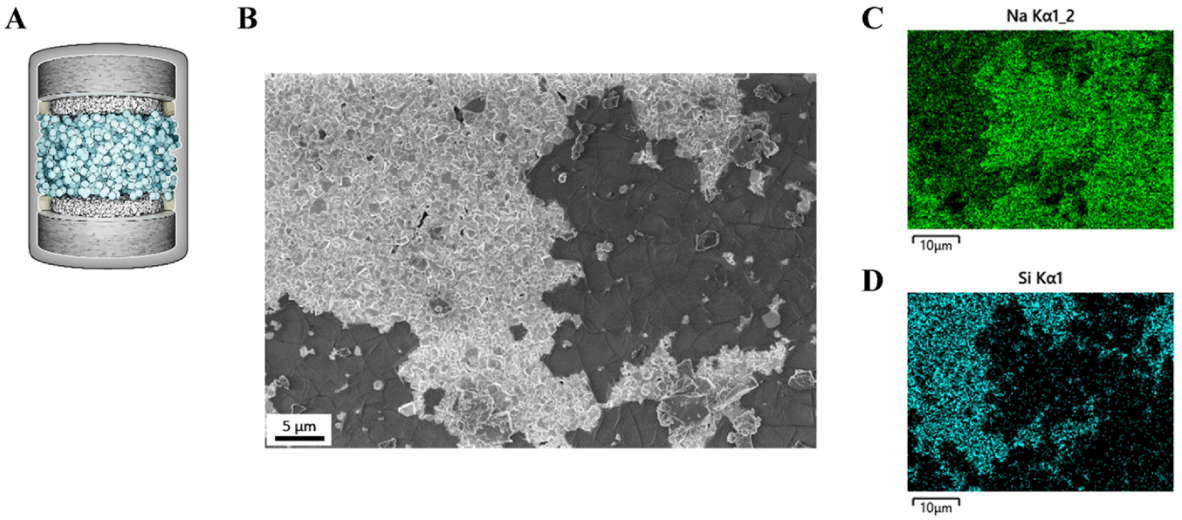

Figure 10. SEM (B) and EDX mappings (C, D) of a NZSPO disk taken from a symmetric cell after exposure to current. The NZSPO disk was in contact with Na_3SbS_4, as shown in schematic (A). The $K_{\alpha 1}$ signal of sodium (C) on the NZSPO surface shows an increased intensity at the islands, whereas the $K_{\alpha 1}$ signal of silicon (D) represents the NZSPO disk with a decreased intensity at the islands.

high ionic conductivity of $Na_{2.9}Sb_{0.9}W_{0.1}S_4$. However, for the symmetric cell with Na_3SbS_4 without NZSPO, the formation of an SEI layer due to decomposition of $Na_{2.9}Sb_{0.9}W_{0.1}S_4$ results in two contributions that shape the impedance. The contributions are the resistance between the Na−Sn anode and the SEI $((R)(CPE)_{Na-Sn|SEI})$ and on the other side from the SEI toward the solid electrolyte $((R)(CPE)_{SEI|SE})$. The corresponding two fitted semicircles are shown in Figure S21. The NZSPO interlayer clearly prevents this decomposition. With the insertion of a NZSPO layer (Figure 8B), two contributions can be clearly distinguished. The corresponding fitted semicircles as well as the fitting data for each impedance spectrum are shown in Figure S22 and Table S8. One is the interfacial resistance between NZSPO and the $Na_{2.9}Sb_{0.9}W_{0.1}S_4$ electrolyte $((R)(CPE)_{SEI|NZSPO})$, and the other is the resistance of the interface between the anode material Na−Sn toward the NZSPO interlayer $((R)(CPE)_{NZSPO|Na-Sn})$. The interfacial resistance, assumed to be a constriction resistance, may also explain why the resistance of the interface between NZSPO and $Na_{2.9}Sb_{0.9}W_{0.1}S_4$ is much lower than in the Na_3SbS_4 cell with NZSPO. As can be deducted by $R_{Cstr} = \sum_i \alpha_i \cdot 1/\sigma_i$, the several orders of magnitude higher conductivity of $Na_{2.9}Sb_{0.9}W_{0.1}S_4$ compared to Na_3SbS_4 leads to a lower constriction resistance. Equal to the symmetric cell with NZSPO and the Na_3SbS_4 electrolyte, the first two impedance measurements show the greatest discrepancies to the consecutive measurements, which only reach 354 $\Omega \cdot cm^2$ after 55 h. Three major points make the combination of the NZSPO protective interlayer with $Na_{2.9}Sb_{0.9}W_{0.1}S_4$ a promising choice for Na-ASSBs. First, the overall much lower resistance due to the high conductivity of the sulfide SE; second, the low interfacial resistance between NZSPO and $Na_{2.9}Sb_{0.9}W_{0.1}S_4$; and third, the stability over time.

The XPS results, where the intensity of the SEI component in the Zr spectrum does not increase with time, in combination with the impedance measurements, with no significant increase in resistance with NZSPO, underline the hypothesis of a stable SEI.

Evolution of the NZSPO/Na_3SbS_4 and NZSPO/$Na_{2.9}Sb_{0.9}W_{0.1}S_4$ Interfaces after Cycling. To test the structural stability of the rigid NZSPO interlayer, the surface, previously in contact with the sulfide SE and after cycling in a cell (Figure S23B), was studied with SEM and EDX. In the SEM images, the sulfide particles can be well distinguished from the highly crystalline NZSPO surface. The cell setup is shown in Figure 9A, and the direction of analysis of the NZSPO layer is indicated by an arrow. In Figure 9B, the SEM image is presented. The particles with different morphologies, as highlighted with a red circle, are Na_3SbS_4 SE particles that remained on the surface after cell disassembly. The EDX images in Figure 9C,9D support this observation, showing sulfur intensity and lack of intensity in the silicon spectrum at the corresponding positions. Complementary elements from the EDX measurements are shown in Figure S24. The surface of the NZSPO interlayer seems to be unchanged. A pristine NZSPO sample is shown in Figure S25.

In the 3E impedance measurements, the cathode showed a strong influence on cell performance. To remove the cathode contribution and study only the effect of the newly introduced NZSPO layer, symmetric cells with anode material on both sides were subjected to a unidirectional stripping/plating experiment. The applied current was chosen to be equal to the current used in Na-ASSB cell cycling. The voltage response is shown in Figure S26. The impedance of the symmetric cell remained equal before and after stripping (Figure S27). The NZSPO surface, after having been in contact with Na_3SbS_4 and after exposure to current, is presented in Figure 10. The SEM image, supported by EDX results, shows—apart from the pure NZSPO—islands with increased sodium and oxygen signal intensities (see Figure S28). The silicon signal in these areas was decreased (Figure 10D), whereas phosphorus and zirconium signals neither increased nor decreased in intensity compared to the pristine NZSPO surface. A decomposition product of Na_3SbS_4 can be excluded since the sulfur signal only appears locally where single Na_3SbS_4 particles remained on the surface after cell disassembly. Formation of a $Na_xP_yZr_zO$-phase

https://doi.org/10.1021/acsami.3c09256
ACS Appl. Mater. Interfaces 2023, 15, 50457−50468

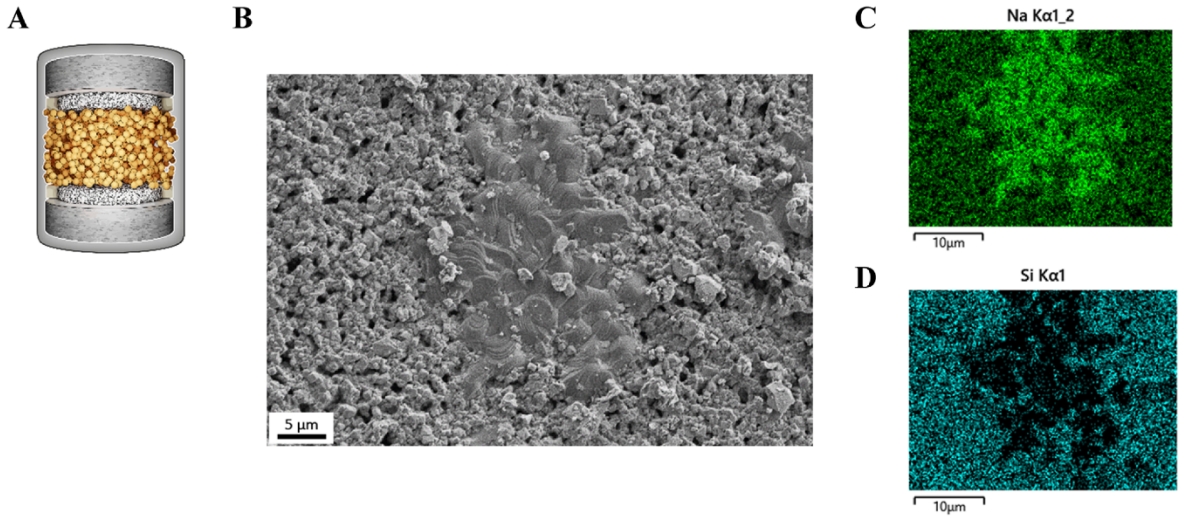

Figure 11. SEM (B) and EDX mappings (C, D) of a NZSPO disk taken from a symmetric cell after exposure to current. The NZSPO disk was in contact with $Na_{2.9}Sb_{0.9}W_{0.1}S_4$, as shown in schematic (A). The $K_{\alpha 1}$ signal of sodium (C) on the NZSPO surface shows an increased intensity at the islands, whereas the $K_{\alpha 1}$ signal of silicon (D) represents the NZSPO disk with a lack of intensity at the islands.

can be explained by the increased signals of Na, O, P, and Zr and the decreased signal of Si. Since Zr and P have a nearly overlapping characteristic kinetic energy of $Zr_{L\alpha}$ = 2.042 keV and $P_{K\alpha}$ = 2.013 keV, a product with only one of the two elements is possible, even though they show both signal intensities in EDX. Previously, the islands were studied to be Na_3PO_4.[41]

As in the case of the NZSPO|Na_3SbS_4 interface, the NZSPO surface also exhibited islands after contact with $Na_{2.9}Sb_{0.9}W_{0.1}S_4$ and after exposure to current, as shown in Figure 11 and additionally in Figures S29 and S30. The islands showed an increase in sodium and oxygen intensities and a decrease in the silicon signal intensity.

As reported previously, the NZSPO surface exhibits Na_3PO_4 coverage after synthesis. Low-energy ion scattering spectroscopy revealed an overall nanometer-thin coverage,[41] whereas others see islands already detectable with electron microscopy. The role of the Na_3PO_4 coverage, according to Quérel et al.,[41] is reported to even improve the affinity toward sodium metal, leading to lower interface resistances. However, studies with Na−Sn or the effect of removal of this coverage on the stability of the Na|NZSPO interface have not been reported to our knowledge. An increase of the islands/coverage upon current flow has also not been confirmed to our knowledge until now. We hypothesize that the high resistance of the NZSPO|sulfide SE interface caused by constriction leads to small local hotspots during the current flow. These hotspots induce the decomposition of NZSPO, resulting in an increased Na_3PO_4 island formation at these constriction hotspots. Since neither sulfur nor antimony was detected in the islands, a partial restructuring of the NZSPO leading to an increased Na_3PO_4 concentration is likely. Since the impedance does not change before and after current flow in the symmetric cell, the islands, however, might not negatively affect the cell performance, as is in accordance with the literature.[41]

CONCLUSIONS

Na-ASSB cells with a sulfide SE separator and Na−Sn as anode were cycled and showed a continuous increase of overvoltage and capacity fading. The use of a reference electrode in 3E-electrode cells allowed the separation of anode and cathode contributions to the increasing cell resistance. The reason for the increasing anode impedance is the decomposition of the sulfide electrolyte in contact with the Na−Sn anode, as confirmed by XPS measurements. The impedance increase at the anode side can be mitigated by an NZSPO interlayer, preventing the formation of a steadily growing interphase. The use of symmetric cells with and without protective NZSPO disks enabled a direct comparison. The overall resistance, especially for the cell with NZSPO and Na_3SbS_4, increased. The use of the NZSPO interlayer, however, provided the solution for the decomposition at the anode side, hindering the chemical decomposition, especially for the highly conductive tungsten-substituted sulfide electrolyte ($Na_{2.9}Sb_{0.9}W_{0.1}S_4$) at the Na−Sn anode. *In situ* XPS measurements underline the development of a stable interface between sodium and NZSPO. As an outlook, the use of the rigid NZSPO may pose mechanical issues, especially in all-solid-state full cells upon volume changes of the CAM, as already indicated in this work for the full cells with and without NZSPO. The good performance in symmetric cells, however, shows a very positive electrochemical effect: the NZSPO allows the use of sodium metal as anode, which otherwise would strongly react with the sulfide electrolyte. The improvement of the stability of the cathode composite is a problem that must be addressed independently in the future. Clearly, oxide cathode materials need to be coated, as in the case of lithium cathode materials, to avoid oxidative degradation of the sulfide electrolyte.

ASSOCIATED CONTENT

Supporting Information

The Supporting Information is available free of charge at https://pubs.acs.org/doi/10.1021/acsami.3c09256.

https://doi.org/10.1021/acsami.3c09256
ACS Appl. Mater. Interfaces 2023, 15, 50457−50468

Material synthesis and XRD of Na−Sn (with structural data from refinement), NEZC, NFMM, Na_3SbS_4 and $Na_{2.9}Sb_{0.9}W_{0.1}S_4$, and NZSPO with obtained lattice parameters from Pawley-fits. Electrochemical stability test of Na−Sn. Complementary impedance spectra of Na−Sn|Na_3SbS_4|NEZC:NFMM:C65 cell and 3E cell. Complementary fitted impedance spectra of symmetric cells over time and before/after current flow. List of equivalent circuit parameters for symmetric cells. Voltage profile of NFMM cycled with liquid electrolyte vs Na metal, of pseudo Sn RE after cell assembly, during deposition of Sn on reference gold wire, of cells with NZSPO interlayer, of the symmetric cell. SEM of Sn-coated gold wire, of NZSPO before/after contact with sulfide electrolyte. SEM and EDX of NZSPO from symmetric cells before/after stripping/plating. XP spectra of Na_3SbS_4, Na−Sn, Na_3SbS_4 and Na−Sn after mixing, NZSPO during Na deposition (PDF)

AUTHOR INFORMATION

Corresponding Author

Jürgen Janek − *Institute for Physical Chemistry, Justus Liebig University Giessen, 35392 Giessen, Germany; Center for Materials Research (ZfM), Justus Liebig University Giessen, 35392 Giessen, Germany;* orcid.org/0000-0002-9221-4756; Email: juergen.janek@phys.chemie.uni-giessen.de

Authors

Laura E. Goodwin − *Institute for Physical Chemistry, Justus Liebig University Giessen, 35392 Giessen, Germany; Center for Materials Research (ZfM), Justus Liebig University Giessen, 35392 Giessen, Germany*

Paul Till − *Institute for Inorganic and Analytical Chemistry, University of Münster, 48149 Münster, Germany*

Monika Bhardwaj − *Forschungszentrum Jülich GmbH, Institute of Energy and Climate Research, Materials Synthesis and Processing (IEK-1), 52425 Jülich, Germany*

Nazia Nazer − *Institute of Chemistry, Humboldt University Berlin, 12489 Berlin, Germany*

Philipp Adelhelm − *Institute of Chemistry, Humboldt University Berlin, 12489 Berlin, Germany;* orcid.org/0000-0003-2439-8802

Frank Tietz − *Forschungszentrum Jülich GmbH, Institute of Energy and Climate Research, Materials Synthesis and Processing (IEK-1), 52425 Jülich, Germany*

Wolfgang G. Zeier − *Institute for Inorganic and Analytical Chemistry, University of Münster, 48149 Münster, Germany; Institut für Energie- und Klimaforschung (IEK), IEK-12: Helmholtz-Institut Münster, Forschungszentrum Jülich, 48149 Münster, Germany;* orcid.org/0000-0001-7749-5089

Felix H. Richter − *Institute for Physical Chemistry, Justus Liebig University Giessen, 35392 Giessen, Germany; Center for Materials Research (ZfM), Justus Liebig University Giessen, 35392 Giessen, Germany;* orcid.org/0000-0002-6587-7757

Complete contact information is available at: https://pubs.acs.org/10.1021/acsami.3c09256

Notes

The authors declare no competing financial interest.

ACKNOWLEDGMENTS

Financial support from the Federal Ministry of Education and Research (BMBF) within the NASEBER consortium (03XP0187) is gratefully acknowledged. The authors thank Joachim Sann, Felix Hartmann, Philip Minnmann, Jonas Hertle, and Ronja Haas for the helpful discussions. The authors take responsibility for the content of this publication.

REFERENCES

(1) Culver, S. P.; Koerver, R.; Krauskopf, T.; Zeier, W. G. Designing Ionic Conductors: The Interplay between Structural Phenomena and Interfaces in Thiophosphate-Based Solid-State Batteries. *Chem. Mater.* **2018**, *30* (13), 4179−4192.

(2) Hwang, J.-Y.; Myung, S.-T.; Sun, Y.-K. Sodium-Ion Batteries: Present and Future. *Chem. Soc. Rev.* **2017**, *46* (12), 3529−3614.

(3) Vaalma, C.; Buchholz, D.; Weil, M.; Passerini, S. A Cost and Resource Analysis of Sodium-Ion Batteries. *Nat. Rev. Mater.* **2018**, *3* (4), 18013.

(4) Escher, I.; Ferrero, G.; Goktas, M.; Adelhelm, P. In Situ (Operando) Electrochemical Dilatometry as a Method to Distinguish Charge Storage Mechanisms and Metal Plating Processes for Sodium and Lithium Ions in Hard Carbon Battery Electrodes. *Adv. Mater. Interfaces* **2022**, *9* (8), No. 2100596.

(5) Fuchs, T.; Culver, S. P.; Till, P.; Zeier, W. G. Defect-Mediated Conductivity Enhancements in $Na_{3-x}Pn_{1-x}W_xS_4$ (Pn = P, Sb) Using Aliovalent Substitutions. *ACS Energy Lett.* **2020**, *5* (1), 146−151.

(6) Ohno, S.; Banik, A.; Dewald, G. F.; Kraft, M. A.; Krauskopf, T.; Minafra, N.; Till, P.; Weiss, M.; Zeier, W. G. Materials Design of Ionic Conductors for Solid State Batteries. *Prog. Energy* **2020**, *2* (2), 022001.

(7) Ma, Q.; Tietz, F. Solid-State Electrolyte Materials for Sodium Batteries: Towards Practical Applications. *ChemElectroChem* **2020**, *7* (13), 2693−2713.

(8) Minnmann, P.; Quillman, L.; Burkhardt, S.; Richter, F. H.; Janek, J. Editors' Choice—Quantifying the Impact of Charge Transport Bottlenecks in Composite Cathodes of All-Solid-State Batteries. *J. Electrochem. Soc.* **2021**, *168* (4), 040537.

(9) Wolfenstine, J.; Go, W.; Kim, Y.; Sakamoto, J. Mechanical Properties of NaSICON: A Brief Review. *Ionics* **2023**, *29* (1), 1−8.

(10) Qie, Y.; Wang, S.; Fu, S.; Xie, H.; Sun, Q.; Jena, P. Yttrium-Sodium Halides as Promising Solid-State Electrolytes with High Ionic Conductivity and Stability for Na-Ion Batteries. *J. Phys. Chem. Lett.* **2020**, *11* (9), 3376−3383.

(11) Ma, Q.; Tsai, C.-L.; Wei, X.-K.; Heggen, M.; Tietz, F.; Irvine, J. T. S. Room Temperature Demonstration of a Sodium Superionic Conductor with Grain Conductivity in Excess of 0.01 S•cm^{-1} and its Primary Applications in Symmetric Battery Cells. *J. Mater. Chem. A* **2019**, *7* (13), 7766−7776.

(12) Wen, Y.; He, K.; Zhu, Y.; Han, F.; Xu, Y.; Matsuda, I.; Ishii, Y.; Cumings, J.; Wang, C. Expanded Graphite as Superior Anode for Sodium-Ion Batteries. *Nat. Commun.* **2014**, *5*, No. 4033.

(13) Jache, B.; Adelhelm, P. Use of Graphite as a Highly Reversible Electrode with Superior Cycle Life for Sodium-Ion Batteries by Making Use of Co-Intercalation Phenomena. *Angew. Chem., Int. Ed.* **2014**, *53* (38), 10169−10173.

(14) Escher, I.; Freytag, A. I.; Del López Amo, J. M.; Adelhelm, P. Solid-State NMR Study on the Structure and Dynamics of Graphite Electrodes in Sodium-Ion Batteries with Solvent Co-Intercalation. *Batteries Supercaps* **2023**, *6* (2), No. e202200421.

(15) Zhao, C.; Liu, L.; Qi, X.; Lu, Y.; Wu, F.; Zhao, J.; Yu, Y.; Hu, Y.-S.; Chen, L. Solid-State Sodium Batteries. *Adv. Energy Mater.* **2018**, *8* (17), No. 1703012.

(16) Lao, M.; Zhang, Y.; Luo, W.; Yan, Q.; Sun, W.; Dou, S. X. Alloy-Based Anode Materials toward Advanced Sodium-Ion Batteries. *Adv. Mater.* **2017**, *29* (48), No. 1700622, DOI: 10.1002/adma.201700622.

(17) Qian, J.; Xiong, Y.; Cao, Y.; Ai, X.; Yang, H. Synergistic Na-Storage Reactions in Sn_4P_3 as a High-Capacity, Cycle-Stable Anode of Na-Ion Batteries. *Nano Lett.* **2014**, *14* (4), 1865−1869.
(18) Palaniselvam, T.; Goktas, M.; Anothumakkool, B.; Sun, Y.-N.; Schmuch, R.; Zhao, L.; Han, B.-H.; Winter, M.; Adelhelm, P. Sodium Storage and Electrode Dynamics of Tin−Carbon Composite Electrodes from Bulk Precursors for Sodium-Ion Batteries. *Adv. Funct. Mater.* **2019**, *29* (18), No. 1900790.
(19) Mou, H.; Xiao, W.; Miao, C.; Li, R.; Yu, L. Tin and Tin Compound Materials as Anodes in Lithium-Ion and Sodium-Ion Batteries: A Review. *Front. Chem.* **2020**, *8*, 141.
(20) Wang, J.; Fan, F.; Liu, Y.; Jungjohann, K. L.; Lee, S. W.; Mao, S. X.; Liu, X.; Zhu, T. Structural Evolution and Pulverization of Tin Nanoparticles during Lithiation-Delithiation Cycling. *J. Electrochem. Soc.* **2014**, *161* (11), F3019−F3024.
(21) Zhang, W.-J. A Review of the Electrochemical Performance of Alloy Anodes for Lithium-Ion Batteries. *J. Power Sources* **2011**, *196* (1), 13−24.
(22) Ellis, L. D.; Ferguson, P. P.; Obrovac, M. N. Sodium Insertion into Tin Cobalt Carbon Active/Inactive Nanocomposite. *J. Electrochem. Soc.* **2013**, *160* (6), A869−A872.
(23) Tian, Y.; Sun, Y.; Hannah, D. C.; Xiao, Y.; Liu, H.; Chapman, K. W.; Bo, S.-H.; Ceder, G. Reactivity-Guided Interface Design in Na Metal Solid-State Batteries. *Joule* **2019**, *3* (4), 1037−1050.
(24) Wenzel, S.; Leichtweiss, T.; Weber, D. A.; Sann, J.; Zeier, W. G.; Janek, J. Interfacial Reactivity Benchmarking of the Sodium Ion Conductors Na_3PS_4 and Sodium β-Alumina for Protected Sodium Metal Anodes and Sodium All-Solid-State Batteries. *ACS Appl. Mater. Interfaces* **2016**, *8* (41), 28216−28224.
(25) Zhang, S.; Zhao, Y.; Zhao, F.; Zhang, L.; Wang, C.; Li, X.; Liang, J.; Li, W.; Sun, Q.; Yu, C.; Luo, J.; Doyle-Davis, K.; Li, R.; Sham, T.-K.; Sun, X. Gradiently Sodiated Alucone as an Interfacial Stabilizing Strategy for Solid-State Na Metal Batteries. *Adv. Funct. Mater.* **2020**, *30* (22), No. 2001118.
(26) Deysher, G.; Chen, Y.-T.; Sayahpour, B.; Lin, S. W.-H.; Ham, S.-Y.; Ridley, P.; Cronk, A.; Wu, E. A.; Tan, D. H. S.; Doux, J.-M.; Oh, J. A. S.; Jang, J.; Nguyen, L. H. B.; Meng, Y. S. Evaluating Electrolyte-Anode Interface Stability in Sodium All-Solid-State Batteries. *ACS Appl. Mater. Interfaces* **2022**, *14* (42), 47706−47715.
(27) Zhang, W.; Weber, D. A.; Weigand, H.; Arlt, T.; Manke, I.; Schröder, D.; Koerver, R.; Leichtweiss, T.; Hartmann, P.; Zeier, W. G.; Janek, J. Interfacial Processes and Influence of Composite Cathode Microstructure Controlling the Performance of All-Solid-State Lithium Batteries. *ACS Appl. Mater. Interfaces* **2017**, *9* (21), 17835−17845.
(28) Hertle, J.; Walther, F.; Mogwitz, B.; Schröder, S.; Wu, X.; Richter, F. H.; Janek, J. Miniaturization of Reference Electrodes for Solid-State Lithium-Ion Batteries. *J. Electrochem. Soc.* **2023**, *170*, No. 040519.
(29) Wenzel, S.; Leichtweiss, T.; Krüger, D.; Sann, J.; Janek, J. Interphase Formation on Lithium Solid Electrolytes — An in Situ Approach to Study Interfacial Reactions by Photoelectron Spectroscopy. *Solid State Ionics* **2015**, *278*, 98−105.
(30) Stratford, J. M.; Mayo, M.; Allan, P. K.; Pecher, O.; Borkiewicz, O. J.; Wiaderek, K. M.; Chapman, K. W.; Pickard, C. J.; Morris, A. J.; Grey, C. P. Investigating Sodium Storage Mechanisms in Tin Anodes: A Combined Pair Distribution Function Analysis, Density Functional Theory, and Solid-State NMR Approach. *J. Am. Chem. Soc.* **2017**, *139* (21), 7273−7286.
(31) Nayak, P. K.; Yang, L.; Pollok, K.; Langenhorst, F.; Wondraczek, L.; Adelhelm, P. Electrochemical Performance and Ageing Mechanisms of Sol-Gel Synthesized $Na_{2/3}[Mn_{3/5}Fe_{2/5}]O_2$ for Sodium-Ion Batteries. *Batteries Supercaps* **2019**, *2* (1), 104−111.
(32) Chastain, J.; Moulder, J. F. *Handbook of X-ray Photoelectron Spectroscopy: A Reference Book of Standard Spectra for Identification and Interpretation of XPS Data*; Perkin-Elmer Corporation, 1995.
(33) Zhang, Z.; Wenzel, S.; Zhu, Y.; Sann, J.; Shen, L.; Yang, J.; Yao, X.; Hu, Y.-S.; Wolverton, C.; Li, H.; Chen, L.; Janek, J. $Na_3Zr_2Si_2PO_{12}$: A Stable Na^+-Ion Solid Electrolyte for Solid-State Batteries. *ACS Appl. Energy Mater.* **2020**, *3* (8), 7427−7437.
(34) Oh, J. A. S.; Sun, J.; Goh, M.; Chua, B.; Zeng, K.; Lu, L. A Robust Solid−Solid Interface Using Sodium−Tin Alloy Modified Metallic Sodium Anode Paving Way for All-Solid-State Battery. *Adv. Energy Mater.* **2021**, *11* (32), No. 2101228.
(35) Maibach, J.; Lindgren, F.; Eriksson, H.; Edström, K.; Hahlin, M. Electric Potential Gradient at the Buried Interface between Lithium-Ion Battery Electrodes and the SEI Observed Using Photoelectron Spectroscopy. *J. Phys. Chem. Lett.* **2016**, *7* (10), 1775−1780.
(36) Ortmann, T.; Burkhardt, S.; Eckhardt, J. K.; Fuchs, T.; Ding, Z.; Sann, J.; Rohnke, M.; Ma, Q.; Tietz, F.; Fattakhova-Rohlfing, D.; Kübel, C.; Guillon, O.; Heiliger, C.; Janek, J. Kinetics and Pore Formation of the Sodium Metal Anode on NASICON-Type $Na_{3.4}Zr_2Si_{2.4}P_{0.6}O_{12}$ for Sodium Solid-State Batteries. *Adv. Energy Mater.* **2023**, *13* (5), No. 2202712.
(37) Eckhardt, J. K.; Klar, P. J.; Janek, J.; Heiliger, C. Interplay of Dynamic Constriction and Interface Morphology between Reversible Metal Anode and Solid Electrolyte in Solid State Batteries. *ACS Appl. Mater. Interfaces* **2022**, *14* (31), 35545−35554.
(38) Eckhardt, J. K.; Fuchs, T.; Burkhardt, S.; Klar, P. J.; Janek, J.; Heiliger, C. Guidelines for Impedance Analysis of Parent Metal Anodes in Solid-State Batteries and the Role of Current Constriction at Interface Voids, Heterogeneities, and SEI. *Adv. Mater. Interfaces* **2023**, *10* (8), No. 2202354.
(39) Connell, J. G.; Fuchs, T.; Hartmann, H.; Krauskopf, T.; Zhu, Y.; Sann, J.; Garcia-Mendez, R.; Sakamoto, J.; Tepavcevic, S.; Janek, J. Kinetic versus Thermodynamic Stability of LLZO in Contact with Lithium Metal. *Chem. Mater.* **2020**, *32* (23), 10207−10215.
(40) Armstrong, R. D.; Burnham, R. A. The Effect of Roughness on the Impedance of the Interface between a Solid Electrolyte and a Blocking Electrode. *J. Electroanal. Chem. Interfacial Electrochem.* **1976**, *72* (3), 257−266.
(41) Quérel, E.; Seymour, I. D.; Cavallaro, A.; Ma, Q.; Tietz, F.; Aguadero, A. The Role of NaSICON Surface Chemistry in Stabilizing Fast-Charging Na Metal Solid-State Batteries. *J. Phys. Energy* **2021**, *3* (4), 044007.

https://doi.org/10.1021/acsami.3c09256
ACS Appl. Mater. Interfaces 2023, 15, 50457−50468

3.2. Halide and Sulfide Electrolytes in Cathode Composites for Sodium All-Solid-State Batteries and their Stability (2nd Publication)

In this work the reason of the capacity fading of Na–Sn|Na_3SbS_4| Na_3SbS_4:$Na_{0.66}Fe_{0.4}Mn_{0.5}Mg(/Ti)_{0.1}O_2$:C65 is studied focusing on influences of the cathode. Upon first electrochemical cycling experiments together with impedance measurements the high resistance leading to a lack of cyclability was detected. Using TOF-SIMS and XPS measurements the reason for this high resistance was exposed which is the reaction of the Na_3SbS_4 with the cathode active material. A change in catholyte to the less ion conductive $Na_{2.4}Er_{0.4}Zr_{0.6}Cl_6$ proved the degradation of Na_3SbS_4 to be the main problem. Even though studies from the first publication showed an unstable anode, the 3-Electrode measurement shows the primary problem to be still in the cathode. Studies of the halide-based catholyte after cell cycling with the oxide based cathode active material showed the formation of an iron-chloride species which, however, cannot be identified as the reason for the capacity fading but might be a stable SEI. Three studies to make an effort to improve the cycling performance were made. 1. Introducing vapor grown nano fibers to increase the percolation pathway in the cathode which showed a worse performance probably due to an insufficient electronic contact. 2. Increase the temperature to 60°C to improve the ionic conductivity of the catholyte which showed a worse performance probably to an increased reaction at the anode. 3. Include/exclude the redox-activity of manganese by choosing different lower cut-off voltages. That showed the instability and probably phase transformation of the cathode active material upon use of manganese as a redox partner as the capacity fading was much stronger for these cells.

The experiments presented in this publication were designed and executed by the first author under the supervision of F. H. Richter and J. Janek. M. Ziegler helped in the fabrication of cells for the case study testing the same cell to different lower cut-off potentials. P. Till synthesized the sulfide electrolytes under the supervision of W. G. Zeier. N. Nazer synthesized the cathode active materials under the supervision of P. Adelhelm.

This study was part of the NASEBER project funded by the BMBF and the POLiS Cluster of Excellence.

ACS APPLIED MATERIALS & INTERFACES

www.acsami.org Research Article

Halide and Sulfide Electrolytes in Cathode Composites for Sodium All-Solid-State Batteries and their Stability

Laura E. Goodwin, Maya Ziegler, Paul Till, Nazia Nazer, Philipp Adelhelm, Wolfgang G. Zeier, Felix H. Richter, and Jürgen Janek*

Cite This: https://doi.org/10.1021/acsami.4c01652 Read Online

ACCESS | Metrics & More | Article Recommendations | Supporting Information

ABSTRACT: Sodium all-solid-state batteries may become a novel storage technology overcoming the safety and energy density issues of (liquid-based) sodium ion batteries at low cost and good resource availability. However, compared to liquid electrolyte cells, contact issues and capacity losses due to interface reactions leading to high cell resistance are still a problem in solid-state batteries. In particular, sulfide-based electrolytes, which show very high ionic conductivity and good malleability, exhibit degradation reactions at the interface with electrode materials and carbon additives. A new group of solid electrolytes, i.e., sodium halides, shows wider potential windows and better stability at typical cathode potentials. A detailed investigation of the interface reactions of Na_3SbS_4 and $Na_{2.4}Er_{0.4}Zr_{0.6}Cl_6$ as catholytes in cathodes and their cycling performance in full cells is performed. X-ray spectroscopy, time-of-flight spectrometry, and impedance spectroscopy are used to study the interface of each catholyte with a transition metal oxide cathode active material. In addition, impedance measurements were used to study the separator electrolyte Na_3SbS_4 with the catholyte $Na_{2.4}Er_{0.4}Zr_{0.6}Cl_6$. In conclusion, cathodes with $Na_{2.4}Er_{0.4}Zr_{0.6}Cl_6$ show a higher stability at low C-rates, resulting in lower interfacial resistance and improved cycling performance.

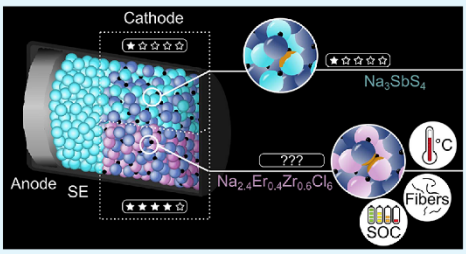

KEYWORDS: *solid electrolyte, sodium battery, all-solid-state battery, cathode composite*

INTRODUCTION

As the need for alternative battery technologies increases, sodium all-solid-state batteries (ASSBs) might be a new technology that will not replace but can usefully complement lithium and sodium ion batteries. The main advantages of sodium batteries in general are the overall lower cost[1] and higher abundance of sodium compared to lithium.[2] The lower volumetric and gravimetric energy density can either be compensated by the low cost, its relevance reduced in electric vehicles with short-range, or neglected in large-scale grid storage. It is also more reactive than lithium,[3] which leads to more side products, which in liquid cells, however, kinetically prevents thermal runaway.[4] Studies of lithium solid-state batteries have already been good indicators of potential material properties for their sodium-based counterparts. Thiophosphate-based solid electrolytes, for example, have shown significant instabilities with high operating potential cathodes[5,6] whereas halides have shown an increased stability as catholyte in lithium solid-state cells.[7]

In an ASSB, the three major components are the anode, the separator electrolyte, and the cathode composite. The cathode composite consists of a redox-active material, e.g., a layered oxide in the present case,[8] which ideally has a high redox potential and a high capacity. These layered oxides form the mixed conducting phase (with a high electronic partial conductivity) in the cathode composite. Carbon additives, even though they have been proven to accelerate degradation in lithium cathode composites,[9−11] are still needed to form a sufficient electron-conducting network for cell cycling. The solid electrolyte used in the cathode, the so-called catholyte, is the ion-conducting phase (assuming that most cathode active materials (CAM) have considerably lower ionic conductivity). In the composite, there are not only the redox-relevant interfaces for electron and ion charge transfer but also grain boundaries in the solid electrolyte and newly formed interfaces of passivation layers as well as pores.[12] It was shown that stability and charge transfer kinetics at the interfaces between cathode and solid electrolyte is crucial for the lifetime and rate capability of the cells.[3]

The key problems of solid electrolytes are the lacking control of particle size distribution, contact issues, and degradation in contact with the active electrode materials. Changes in microstructure and morphology can rarely be compensated for by rigid solid electrolytes. There are three main problems of degradation that can occur in ASSBs: First,

Received: January 29, 2024
Revised: March 28, 2024
Accepted: March 29, 2024

https://doi.org/10.1021/acsami.4c01652
ACS Appl. Mater. Interfaces XXXX, XXX, XXX−XXX

structural degradation of cathode active material leading to loss of contact[6] and irreversible desodiation; second, chemical degradation, and third, electrochemical degradation at high potentials with respect to the solid electrolyte.[5,11] Very often, degradation at the SE|CAM interface leads to high charge transfer resistances. From lithium ASSBs, it is known that sulfide-based electrolytes show severe decomposition at the CAM surface[13,5] which is further enhanced by the use of carbon.[11] As an old class of materials that recently attracts new interest,[14,15] the ternary and higher rare earth halides, like $Na_{2.4}Er_{0.4}Zr_{0.6}Cl_6$ (NEZC) for example in the case of sodium,[16] appear to show less reactions with the active materials and offer good processability and ease of synthesis.

In this work, we investigate sodium ASSB full-cells with two different catholytes at room temperature. Na_3SbS_4 as a sulfide catholyte is studied in a cathode composite with intercalation-type transition metal oxide cathode active materials. The strong degradation of the catholyte, leading to a high resistance in electrochemical measurements, is confirmed by TOF-SIMS and XPS measurements. Its replacement by NEZC catholyte shows an increased stability compared to Na_3SbS_4 and allows a more detailed electrochemical investigation. TOF-SIMS and XPS data show a chemical reaction of the catholyte with the electrode material, giving, however, no definite insight into whether this is the main reason for capacity fading over time.

EXPERIMENTAL SECTION

$Na_3Sn|Na_{15}Sn_4$ (Na−Sn). Na−Sn anodes were prepared as reported under argon atmosphere in batches of 2 g by ball milling.[17] Tin powder (100 mesh, 99.999% from Fisher Scientific GmbH) was alloyed with elemental sodium (BASF SE) in a stoichiometric ratio with a 1.05 wt % excess of sodium. The media-to-sample ratio was 40:1, the media being 5 mm ZrO_2 balls in a 45 mL ball milling cup. The synthesis was carried out for 20 h with 10 min of milling and 10 min of resting time at 510 rpm. The powder was subsequently ground for 20 min.

$Na_{2.4}Er_{0.4}Zr_{0.6}Cl_6$. $Na_{2.4}Er_{0.4}Zr_{0.6}Cl_6$ (NEZC) was prepared under argon atmosphere as described by Schlem et al.[16] resulting in a catholyte with an ionic conductivity of 0.04 $mS{\cdot}cm^{-1}$. NaCl (Merck, 99.5% predried at 200 °C for 48 h under dynamic vacuum), $ErCl_3$ (Sigma-Aldrich, 99%) and $ZrCl_4$ (Alfa Aesar, 99.5%) were mixed with an excess of $ErCl_3$ of 5−10 wt % and brought to reaction by ball milling. With a 30:1 mass ratio between milling media (5 mm ZrO_2 balls) and precursor-powder, the reaction was conducted in 99 milling cycles with 15 min running time and 5 min rest at 500 rpm.

$Na_{0.66}Fe_{0.5}Mn_{0.5}O_2$. High energy ball milling (Fritsch PULVERISETTE 7) was used for the synthesis of $Na_{0.66}Fe_{0.5}Mn_{0.5}O_2$ (NFM). Stoichiometric amounts of the precursors Na_2CO_3 (Alfa Aesar), Mn_2O_3 (Alfa Aesar) and Fe_2O_3 (Fulka) were ball milled at 450 rpm for 1 h in a zirconia jar (180 mL) using zirconia balls (10 mm diameter) and a ball to powder ratio of 10:1. The ball milled powder was calcinated at 450 °C for 6 h, followed by a 900 °C calcination step for 12 h in air. An additional 5% sodium precursor was added to compensate for the sodium loss during calcination.

$Na_{0.66}Fe_{0.4}Mn_{0.5}Mg_{0.1}O_2$. The layered oxide $Na_{0.66}Fe_{0.4}Mn_{0.5}Mg_{0.1}O_2$ (NFMM) was synthesized by carbonate coprecipitation. The reaction vessel was heated to 55 °C in a water bath. Stoichiometric amounts of $FeSO_4{\cdot}7H_2O$ (Merck), $MnSO_4{\cdot}H_2O$ (Alfa Aesar), and $MgSO_4$ (Sigma-Aldrich) were dissolved in water to obtain a 2 M aqueous solution. This solution was added dropwise using a dropping funnel to the reactor vessel. 2 M Na_2CO_3 (Alfa Aesar)−0.2 M NH_4OH (Sigma-Aldrich) base solution was prepared and added dropwise to the reaction vessel, so that the pH of the reaction mixture, monitored with a SevenCompact pH meter S220 (Mettler Toledo) was always kept between 7.5 and 8. Afterward, the precipitated (Fe, Mn, and Mg) carbonate was allowed to mature with continuous stirring at room temperature and then washed with water using a centrifuge (Rotina 380, Hettich) to remove the sulfate anions. The precipitate was then predried at 60 °C under air atmosphere, before drying overnight under vacuum at 120 °C. Then, the as-obtained metal carbonate precursor was mixed with Na_2CO_3 in the required stoichiometry, ground and heated to 500 °C for 6 h (5 °C/min heating rate, air atmosphere, oven: Nabertherm). Subsequently, the material was reground and heated to 900 °C, for 12 h (5 °C/min). The calcination product was allowed to cool to room temperature (1 °C/min) prior to being transferred into an argon-filled glovebox (Braun, $p(O_2)/p < 0.1$ ppm, $p(H_2O)/p < 0.1$ ppm).

Na_3SbS_4. Na_3SbS_4 was synthesized by a solid-state reaction under inert atmosphere in a sealed ampule. Before use, the ampules were dried under dynamic vacuum at 800 °C for 2 h to remove all traces of water. Syntheses were carried out in argon atmosphere glove boxes. The precursors Na_2S (Sigma-Aldrich), S (Acros Organics, 99.999%) and Sb_2S_3 were mixed in stoichiometric ratios in an agate mortar for 20 min. The mixture was then pressed into a pellet, loaded into an ampule, and sealed under vacuum. The sample was heated in a tube furnace up to 550 °C with a heating ramp of 30 °C/h and dwelled for 20 h and was left in the furnace afterward to cool down naturally. The ampule was then transferred to a glovebox, and the obtained pellet was ground into a powder for further use.

Cell Assembly. All cells were assembled and compacted under an argon atmosphere and at room temperature. The special cell casing used to avoid water, nitrogen or oxygen contamination and keep a constant pressure of 25 MPa was described previously.[18] All powders were distributed evenly by using a spatula and turning the steel stamps upon closing the cell.

A. Full Cells. Full cells were prepared with 50 mg of solid electrolyte Na_3SbS_4 powder that was compacted in a polyether ether ketone (PEEK) cell casing with a diameter of 10 mm by using a spindle press. The cathode composite was freshly prepared by grinding for 20 min a 100 mg batch with weight ratios of 66:30:4 of NFM:Na_3SbS_4:C65. The same weight ratio applies to the full cells with magnesium (NFMM) doped CAM. The composites for full cells with NECZ as catholyte were prepared in the same way with the ratio of 66:30:4 for NFMM:NEZC:C65 and with the carbon additive VGCF (NFMM:NEZC:VGCF), respectively. C65 was purchased from Imerys Graphite & Carbon Switzerland Ltd., VGCF (iron free) from Sigma-Aldrich and the CAM and catholyte synthesized as mentioned above. 14 mg of cathode composite were evenly distributed on the prepressed solid electrolyte separator and the combination of separator and cathode compacted in a uniaxial press at 380 MPa for 3 min at room temperature. Following this, 50 mg of Na−Sn were evenly distributed on the sulfide solid electrolyte separator interface and contacted with stainless steel rods. A constant stack pressure of 25 MPa was applied to the cell upon measurement.

B. Symmetrical Cells. The symmetric cells were prepared with 200 mg of solid electrolyte Na_3SbS_4 powder that was compacted in a uniaxial press at 380 MPa for 3 min at room temperature in a PEEK cell casing with a diameter of 10 mm. For the cell with Na−Sn as the anode material, 50 mg of Na−Sn was added on each side of the sulfide solid electrolyte and then compacted using a spindle press. The cell was consequently constrained at 25 MPa. For the symmetric cells with sodium metal anodes, a piece of sodium metal was cut from a sodium block (BASF SE) and pressed in between the cling film using a spindle press. Punched out Na foils with 0.5 mm thickness and 6 mm diameter were used. The two sodium metal foils were placed on each side of the prepressed solid electrolyte surface, and a stack pressure of 25 MPa was applied during measurements.

C. SE Cells. The solid electrolyte cells for impedance measurements were prepared by compacting 100 mg of Na_3SbS_4 in the as mentioned cell casing and adding 100 mg of NEZC. Both electrolytes were then compacted in a uniaxial press at 380 MPa for 3 min at room temperature and a stack pressure of 50 MPa was applied.

D. Three-Electrode Cell. For the three-electrode cell, a quasi-reference electrode (RE) was prepared. The RE was prepared by the electrochemical deposition of tin on a gold-coated tungsten wire (Goodfellow, 10 μm in diameter). Therefore, 500 mg of Brij 35 (an acid resistant emulsifier), 60 mg of 4-diethylamino-benzaldehyde and

https://doi.org/10.1021/acsami.4c01652
ACS Appl. Mater. Interfaces XXXX, XXX, XXX−XXX

4 g tin(II) sulfate were dissolved in 7 mL sulfuric acid, 4 mL of formaldehyde and 100 mL distilled water. Tin foil with an area of 3 × 1 cm^2 (thickness 0.127 mm, 99% Sigma-Aldrich) and a 5 mm long gold wire, already attached to the peak inlet using kapton tape, were immersed into the solution. With a Biologic SP-200 potentiostat and a current of 450 μA, tin was plated electrochemically onto the gold wire for 155 s to reach a thickness of 5 μm. The three-electrode cell with the as mentioned RE was assembled according to Hertle et al.[19] by compacting 100 mg of the SE separator (Na_3SbS_4) on both sides of the previously reported Sn plated wire attached to a peak inlet, using a spindle press. Subsequently, the steps of the cathode and anode addition were carried out as described for the full cell, including the constant load of 25 MPa.

Cell Cycling. Each cycling procedure, apart from the indicated 60 °C measurement, was conducted at 25 °C. For the (A) full cells, a constant pressure of 25 MPa during cycling was used. A Biologic VMP 300 potentiostat was used to charge and discharge with intermittent open circuit voltage (OCV) steps. The full cells were charged with a current density of 24 μA cm^{-2} to 4.0 V and discharged to either 1.5 V or (see Figure 14) 2.4, 2.2, 2.0, or 1.8 V, respectively. To enable a relaxation of the cell prior to impedance measurements intermittent OCV steps of 3 h were added after each charge and discharge step. To calculate the C-rate, a theoretical capacity of q_{th} = 172 mAh g^{-1} for the CAM was used. For the Galvanostatic Intermittent Titration Technique (GITT) measurement, the cell was charged for 6 h at 24 μA cm^{-2}, relaxed for 3.5 h until the upper cutoff voltage was reached. Subsequently, the cell was discharged for 6 h at 24 μA cm^{-2} and was relaxed for 3.5 h. The lower cutoff potential was set to E = 0 V and the cell repeatedly discharged to this potential. For the (B) symmetric cell with sodium metal and Na−Sn, respectively, an alternating current of 39.25 μA cm^{-2} was applied for 35 h each with 600 s of charging and discharging with 10 s of the OCV steps in between. The cutoff potential was set to ±3 V. The (D) three-electrode cell was charged to 4 V and discharged to 1.5 V with a current density of 24 μA cm^{-2} for two cycles. To enable a relaxation of the cell prior to impedance measurements, intermittent OCV steps of 5 h were added after each charge and discharge step. To charge with 0.01C, a theoretical capacity of q_{th} = 172 mAh g^{-1} for the cathode active material was assumed.

Electrochemical Impedance Spectroscopy (EIS). For all measurements, a potentiostat (BioLogic VMP 300, Seyssinet-Pariset, France) was used and the RelaxIS 3 software package (rhd Instruments, Darmstadt, Germany) was used for fitting of the data. All measurements were conducted at 25 °C. The pressure loading of all full cells was 25 MPa by using a spring to compensate for pressure relaxation occurring due to elastic deformation of individual components. For the symmetric cells and the SE cell the same setup was used with a pressure loading of 25 and 50 MPa, respectively. An amplitude of 10 mV was chosen. For the (A) full cells and the (C) SE cell the current range was set to "auto" and the frequency range was set from 7 MHz to 10 mHz. The full cell impedances were measured directly after cell assembly after the first and second charge and discharge. For the SE cell, impedances were measured every 2 h. For the (D) three-electrode cell two different connections were used to measure the impedance directly after cell assembly (pristine), after the first and second charge and discharge. For the measurement of the impedance between the anode and cathode as well as the impedance of the cathode contributions, the cathode was connected as the working electrode (WE), the anode as the counter electrode (CE) and the RE as the reference electrode. For the anode contributions, the anode was connected as WE and the cathode as CE. For the latter, the current range was set to 10 mA. The frequency range for the measurements with RE was 200 kHz to 10 mHz.

X-ray Photoelectron Spectroscopy (XPS). For each measurement, pellets or powders pressed into Teflon cups were transferred to the XPS under an inert atmosphere. A neutralizer was used for each measurement. As analyzer monochromatic Al K_α radiation (1486.6 eV) was used. XPS measurements for the pristine solid electrolytes Na_3SbS_4 and NEZC as well as the cathode composites were conducted with a PHI 5000 Versa Probe II system (Physical Electronics GmbH). The power of the X-ray source was 50 W with a voltage of 15 kV for the samples containing Na_3SbS_4 and 100 W with a voltage of 15 kV for the samples containing NEZC. The pass energy for detail spectra was set to 23.5 eV for the samples containing Na_3SbS_4 and 46.95 eV for the samples containing NEZC. Depth profiling of 60 s for the Na_3SbS_4 electrolyte and of 540 s for the composite NFM:Na_3SbS_4:C65 was performed using an Ar^+ ion sputter gun with an acceleration voltage of 0.5 kV. Data evaluation was performed with the software CasaXPS (version 2.3.25, Casa Software Ltd.). The calibration for Na_3SbS_4 and the composite NFM:Na_3SbS_4:C65 was set to 284.8 eV of adventitious carbon. For NEZC and the composite NFMM:NEZC:C65, the calibration was set to 182.6 eV of zirconium. Signal fitting was performed using a Shirley background and a GL(30) line shape for samples containing Na_3SbS_4 and a LA(1.53, 243) line shape for samples containing NEZC. Published values for spin−orbit splitting were used as fitting restrictions. The stability test (SI) of Na_3SbS_4 vs NEZC with XPS was conducted with a PHI Versaprobe 4 with monochromatized Al K_α X-ray source (beam diameter 200 μm, X-ray power of 50 W). Therefore, 30 mg of each powder were mixed and ground in a mortar for 10 min and compacted, in a powder sample holder cup. Pass energies were set to 27 eV for the Na 1s and Cl 2p signals and 55 eV for the Zr 3d and Cl 2p signal. The step size was 0.2 eV and the step time was 25 ms.

Time-of-Flight Secondary Ion Mass Spectrometry (TOF-SIMS). TOF-SIMS measurements were performed with a M6 hybrid instrument by IonTOF GmbH, Germany. For each measurement, pellets were transferred to the SIMS under an inert atmosphere using a Leica transfer station. All data were analyzed with the software SurfaceLab 7.2 (IONTOF GmbH, Germany) and measured with a Bi_3^{+2} primary ion gun (30 kV acceleration voltage) in negative polarity and a raster size of 512 × 512 pixels. The measurement of the cathode composite NFM:Na_3SbS_4:C65 post mortem from a full cell after charging the cell to 4 V and discharging it to 1.5 V was performed in imaging mode for the liquid metal ion gun (LMIG) with a primary ion current of 0.4 pA. The analyzer was used in delayed extraction mode with a cycle time of 45 μs. The analyzed sample area was 50 × 50 μm^2 with 1 shot per pixel for 10 min per scan. The sputter crater was set to 400 × 400 μm^2 and sputtered with a 2 keV Cs^+ gun with noninterlaced sputtering and a current of 146 nA with sputter times of 100 s in between scans. The presented images were taken after 34 scans and sputtering of in total ∼1 h. The measurements were conducted of NEZC pressed as a pellet, a cathode composite NFMM:Na_3SbS_4:C65 in an uncycled (pristine), a discharged to 2.4 V and a discharged to 1.5 V state. They were all performed in spectrometry mode for the LMIG with a primary ion current of 0.4 pA. The analyzer was set to spectrometry mode, and the cycle time was set to 110 μs. The analyzed sample area was 100 × 100 μm^2 with a raster size of 512 × 512 pixels with 1 shot per pixel and 13 scans. Secondary ion images were all normalized to the total ion signal to minimize the topographic effects. Four different spots on each sample were measured and plotted as box plots.

Scanning Electron Microscopy (SEM). The samples were investigated using a Merlin SEM instrument by Carl Zeiss. A Leica transfer shuttle was used to transport the samples from the glovebox to the SEM. For the SEM images of the composite cathodes NFMM:Na_3SbS_4:C65 and NFMM:Na_3SbS_4:VGCF, prepared as mentioned above, a compacting step with 380 MPa followed the grinding. They were measured with an SE2 detector with 3 kV acceleration voltage and 100 pA emission current (SI). For the characterization of the elemental distribution on the surface, energy-dispersive X-ray (EDX) spectroscopy measurements were conducted. Therefore, an X-Max 50 Silicon Drift Detector by Oxford Instruments was used, and the obtained data was analyzed with Aztec 3.2 software.

RESULTS AND DISCUSSION

Cells with Na_3SbS_4 Separator and Na_3SbS_4 Catholyte. For an overview of the interfaces studied under different

https://doi.org/10.1021/acsami.4c01652
ACS Appl. Mater. Interfaces XXXX, XXX, XXX−XXX

conditions within this work a schematic illustration is presented in Figure 1. The present study of sodium all-solid-state full cells started with building and testing a cell made of Na−Sn as the anode material, Na_3SbS_4 as the separator material, and a cathode composite. The cathode composite consisted of redox active cathode material (CAM), ion-conducting sulfide catholyte (Na_3SbS_4) and electron-conducting carbon (C65). The weight ratio in the cathode was adopted from studies performed on lithium solid-state cathode composites with a sulfide-based electrolyte resulting in a mass ratio of 66:30:4 for CAM:Na_3SbS_4:C65.[20] With the chosen weight ratio, the best percolation for both ions and electrons was achieved for the lithium based system but could differ for the studied system in this work depending on the partial ionic and electronic conductivities of the cathode active material. The tested CAMs are transition metal oxides $Na_{0.66}Fe_{0.5}Mn_{0.5}O_2$ (NFM) and $Na_{0.66}Fe_{0.4}Mn_{0.5}Mg_{0.1}O_2$ (NFMM). NFMM has previously been studied in cells with liquid electrolyte and analyzed for its structure and electrochemical properties using XRD and impedance spectroscopy.[17] The theoretical capacities are q_{th} = 173 mAh g^{-1} for NFM and q_{th} = 178 mAh g^{-1} for NFMM.

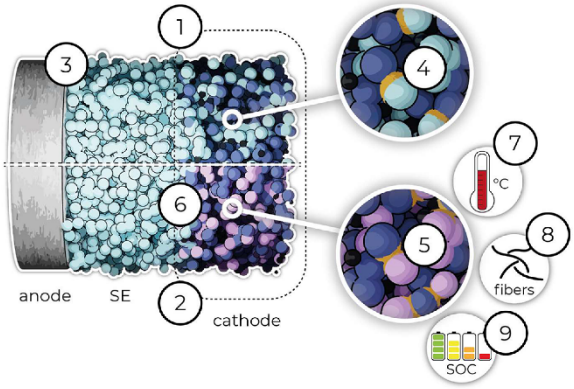

Figure 1. Representation of the studied interfaces in this work. Focus was on the cell (1) with Na_3SbS_4 (turquoise) as catholyte studied with different active materials and (2) with $Na_{2.4}Er_{0.4}Zr_{0.6}Cl_6$ (pink) as catholyte during cell cycling. (3) The anodelsolid electrolyte (SE) interface was studied and an in-depth analysis of the catholyte/CAM interface reaction with (4) Na_3SbS_4 and (5) $Na_{2.4}Er_{0.4}Zr_{0.6}Cl_6$ was conducted. (6) The stability between the separator electrolyte Na_3SbS_4 and the halide catholyte $Na_{2.4}Er_{0.4}Zr_{0.6}Cl_6$ was tested. With $Na_{2.4}Er_{0.4}Zr_{0.6}Cl_6$ as the catholyte, cell cycling was conducted (7) at 60 °C, (8) with carbon fibers as electron conducting additive, and (9) to different lower cutoff potentials, in-/excluding the manganese redox activity.

Electrochemical cycling as well as impedance spectroscopy measurements after cell assembly (uncycled) and after the first charge and discharge step for the cells with each CAM are presented in Figure 2. Only a low first charge capacity was obtained for each CAM with a maximum of 15 mAh g^{-1} for NFMM and only 7 mAh g^{-1} for NFM. The discharge capacity was 5 mAh g^{-1} for NFMM and 2 mAh g^{-1} for NFM.

The reason for the poor cycling performance in these cells is the high overpotential caused by the high internal resistance of these cells. For example, the impedance measurement for NFM shown in Figure 2B indicates an initial resistance of around 1.2 kΩ cm^2 and of 65 kΩ cm^2 after the first charging step. The latter corresponds to an overpotential of 1.56 V considering the applied current density of 24 μA cm^{-2}. Upon discharge, the cells run into the lower cutoff potential very fast and do not deliver a notable discharge capacity. Surprisingly, the discharge current of 24 μA cm^{-2}, until the cutoff potential of 1.5 V is reached, is sufficient to reduce the impedance significantly, but not enough for further cell cycling. The magnesium-doped CAM (Figure 2C, D) presented similar cell cycling results with only minor capacity increase and resistance decrease compared to the other CAMs.

To investigate the source of the high resistance upon charge and associated with the high overpotential, GITT measurements were conducted.

Figure 3 shows the voltage profile with time and the full cell setup with the cathode composite NFM:Na_3SbS_4:C65 schematically. After the first 6 h of charging, the overpotential reached 0.25 V, which increased to 1.5 V after only 18 h of charge. A cutoff voltage at the original cell voltage of 2.25 V would not have given any discharge. Therefore, a lower cutoff voltage of 0 V was chosen to compensate for the major overpotential. After a discharge capacity of more than 314 mAh g^{-1} was reached, the discharge was stopped. The high capacity of 314 mAh g^{-1} compared to the theoretical capacity of 173 mAh g^{-1} is a result of the decomposition of the sulfide solid electrolyte at low voltages.[3]

Symmetric Na−Sn | Na_3SbS_4 | Na−Sn and Na | Na_3SbS_4 | Na Cells. The causes of high internal cell resistances can be numerous. Apart from high contact resistances, decomposition reactions at interfaces forming insulating degradation products (chemical degradation) are a common source for such high impedances. However, blocked or interrupted percolation pathways for ion or electron transport as well as contact loss (chemomechanical degradation) can also be the reason for high resistances. To rule out certain factors for the high resistance, the Na_3SbS_4 sulfide separator electrolyte was cycled in a symmetric cell made of two Na−Sn alloy electrodes to obtain increased chemical and higher mechanical stability. The Na−Sn alloy electrode is a two-phase Na_3Sn|$Na_{15}Sn_4$ alloy.[17,21,22] The necessity to apply external pressure in all-solid-state batteries to primarily compact the cathode composite becomes critical at the anode[23] side because of the ductility of sodium metal.

The stability of symmetrical cell cycling with Na−Sn alloy electrodes is compared to that of sodium metal electrodes in Figure 4. While the symmetrical cell with Na−Sn electrodes shows only a small voltage increase in the lower second decimal places, the symmetrical cell with sodium metal anodes shows an increase from 0.05 to 3 V in 30 h. The 50 mg of Na−Sn powder used as anode material in Figure 4A, however, showed a much lower increase, underlining the higher stability of the Na−Sn alloy electrode.

The inset for the symmetric cell with the Na−Sn alloy in Figure 4A shows a different charge and discharge behavior than the inset for the symmetric cell with sodium in Figure 4B. This phenomenon suggests that the de-/sodiation of the alloy has slower kinetics compared to the dissolution/deposition of sodium metal, respectively.

Degradation of Na_3SbS_4/CAM Composites. The degradation of sulfide solid electrolytes in contact with transition metal oxides in cathode composites has been previously reported extensively.[18] The complementary use of TOF-SIMS and XPS can detect local compositional changes and allows characterization and visualization of decomposition

https://doi.org/10.1021/acsami.4c01652
ACS Appl. Mater. Interfaces XXXX, XXX, XXX−XXX

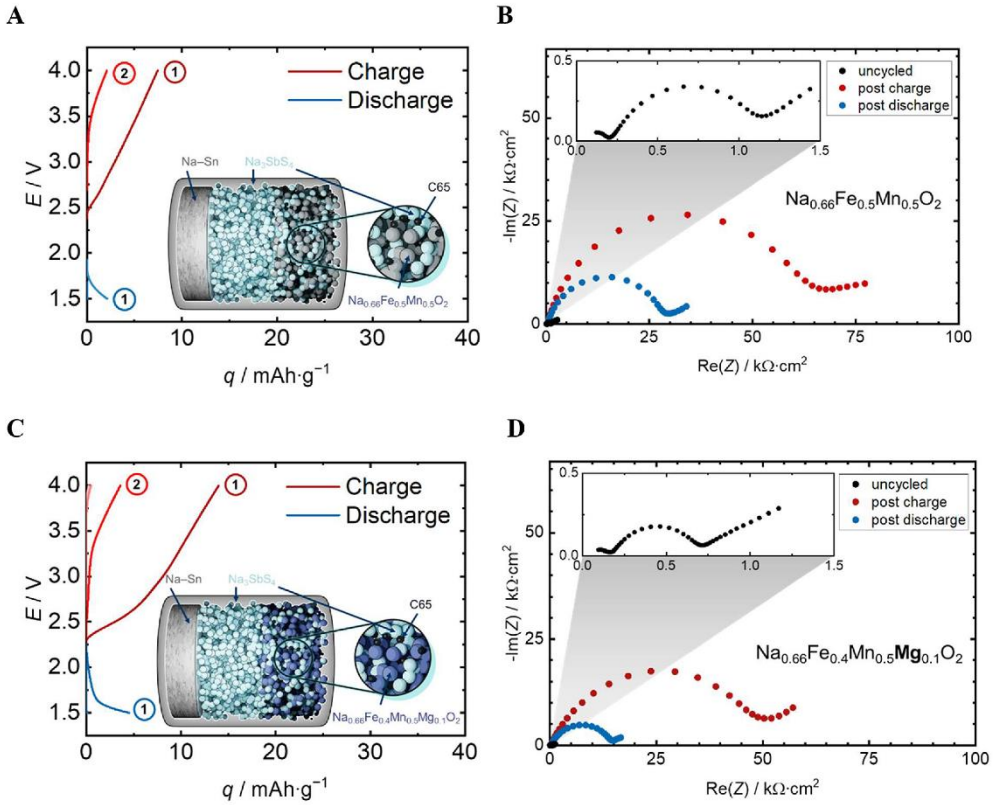

Figure 2. Charge (red) and discharge (blue) curves of Na-ASSB Na−Sn|Na_3SbS_4|CAM:Na_3SbS_4:C65 with Na−Sn as anode, Na_3SbS_4 as separator electrolyte, and a cathode composite comprisng C65, Na_3SbS_4, and (A) NFM or (C) NFMM, respectively. Impedance measurements for the full cells with the CAMs (B) NFM and (D) NFMM for the pristine cell (black) with zoom-in/magnification in the inset (same axes notation), after charge to 4.0 V (red), and after discharge to 1.5 V (blue).

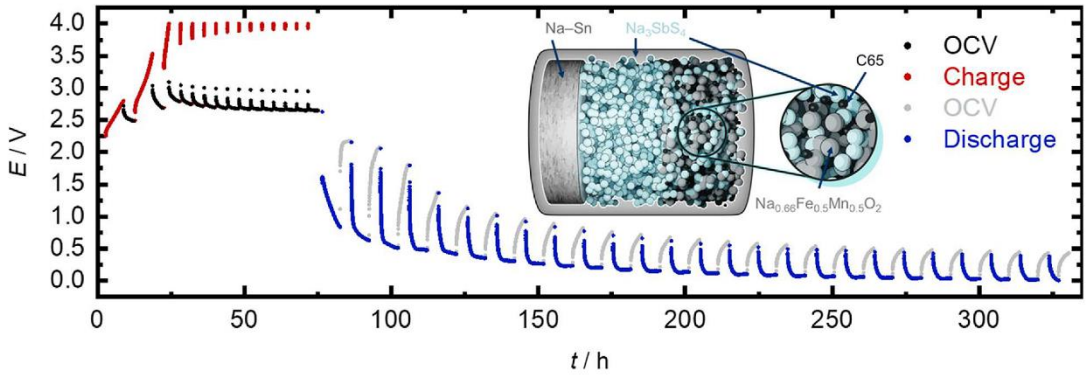

Figure 3. GITT measurement of a full cell Na−Sn|Na_3SbS_4|NFM:Na_3SbS_4:C65 with charging (red) and discharging (blue) steps and set cutoff potentials of E = 4.0 and 0 V. After a maximum of 6 h charge/discharge an intermediate relaxation step of 3.5 h (black/gray) followed. After reaching 4 V as the upper cutoff potential, the charging steps were repeated 12 times. The discharge was stopped after 26 steps without reaching the lower cutoff potential.

products. Whereas XPS offers information on the chemical composition or decomposition of the samples, TOF-SIMS can compensate for the relatively low lateral resolution and low detection limit of XPS. It is very sensitive for compounds with high ionization probabilities and also dependent on the surrounding components.

TOF-SIMS measurements of a cathode composite NFM:Na_3SbS_4:C65 are shown in Figure 5 and revealed the degradation of the sulfide electrolyte in contact with the oxide material after cycling. The S_2^- fragment is representative for the Na_3SbS_4 electrolyte (turquoise) and the FeO_2^- fragment for the $Na_{0.66}Fe_{0.5}Mn_{0.5}O_2$ CAM (blue). The SO_3^- fragment (orange) corresponds to a degradation product of Na_3SbS_4

https://doi.org/10.1021/acsami.4c01652
ACS Appl. Mater. Interfaces XXXX, XXX, XXX−XXX

ACS Applied Materials & Interfaces www.acsami.org Research Article

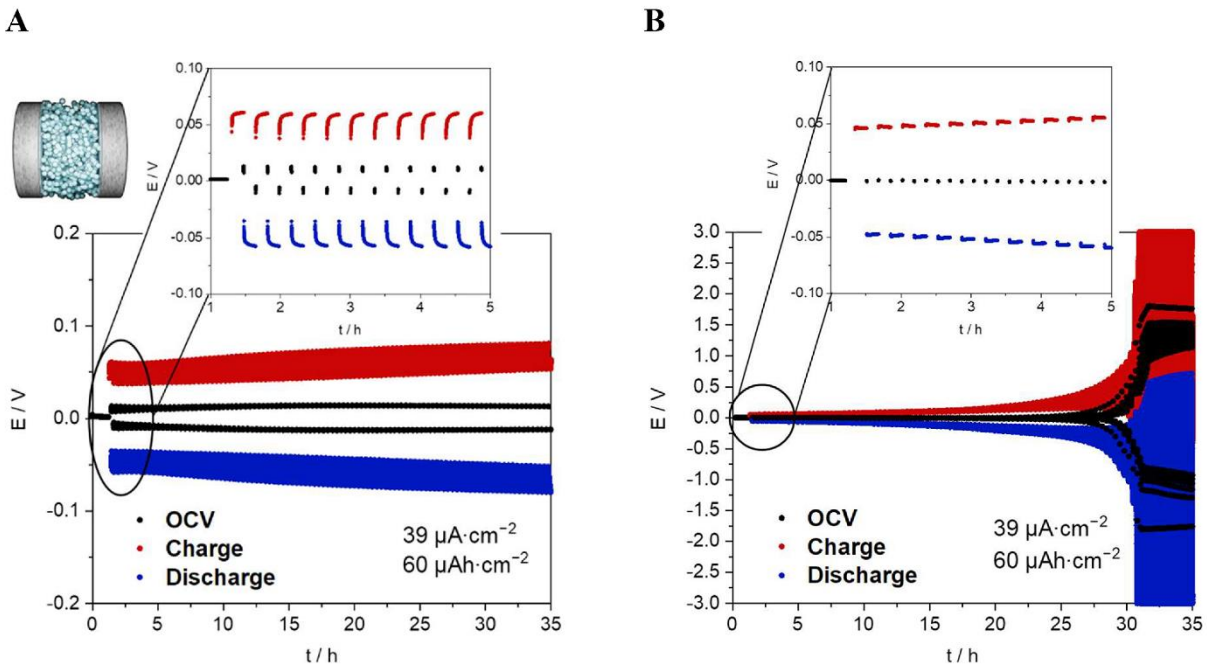

Figure 4. Stripping and plating experiments of symmetrical cells with Na_3SbS_4 as separator electrolyte with (A) Na−Sn and (B) sodium metal as electrode material.

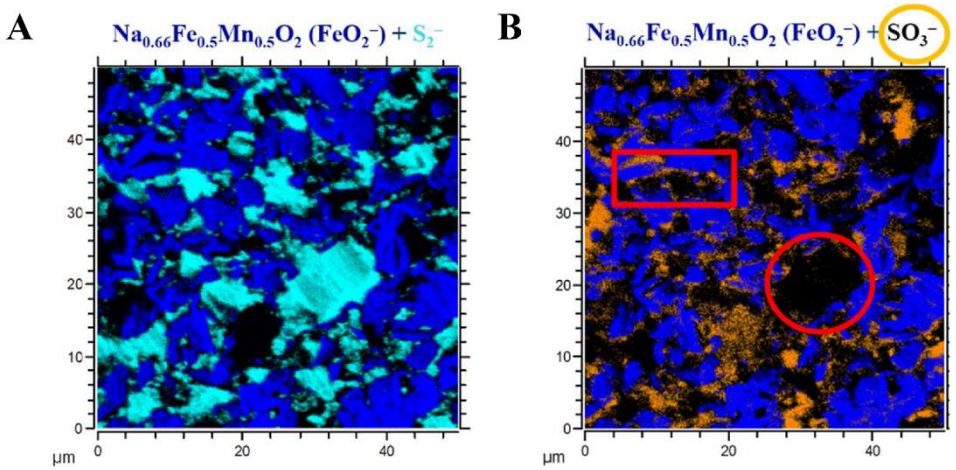

Figure 5. TOF-SIMS measurements of a cathode composite (NFM:C65:Na_3SbS_4) after cycling. (A) In turquoise the signals are shown for the sulfide electrolyte Na_3SbS_4 (S_2^-) and in dark blue for the CAM $Na_{0.66}Fe_{0.5}Mn_{0.5}O_2$ (FeO_2^-). (B) Additionally to the CAM (FeO_2^-) signal the sulfoxide degradation products (SO_3^-) in orange at the CAM interface are marked with a red rectangle. No SO_3^- signal intensity was detected at the Na_3SbS_4 spot (red circle).

with NFM being sulfate or sulfite species. In Figure 5B the SO_3^- fragment (orange) shows no intensity in the spot where an approximately 10 μm × 10 μm Na_3SbS_4 particle is located (red circle) and mainly shows intensity at the edge of the CAM (blue) marked with a red rectangle.

To support these findings, XPS measurements were conducted on pristine Na_3SbS_4 as reference and on a composite containing Na_3SbS_4, NFMM, and C65 after cycling. The spectra for the S 2p signal are shown in Figure 6. The signal expected for Na_3SbS_4 is a doublet peak with spin-orbit splitting of 1.18 eV[24] highlighted in turquoise in Figure 6A. The small doublet peak (brown) at higher binding energies are most probably polysulfide contaminations $S_{X,1}$ already present in the uncycled Na_3SbS_4 reference spectra.

The strong decomposition in the cathode composite forms doublet peaks highlighted in different shades of brown. Due to the oxidation of sulfur, the intensity of the peak attributed to polysulfides already present in the Na_3SbS_4 reference sample increases. With increasing chain length of the polysulfides, the signal intensity shifts to higher binding energies, explaining the additionally fitted polysulfide doublet peak labeled $S_{X,2}$. At binding energies of 170 eV sulfoxide species are detected,

https://doi.org/10.1021/acsami.4c01652
ACS Appl. Mater. Interfaces XXXX, XXX, XXX−XXX

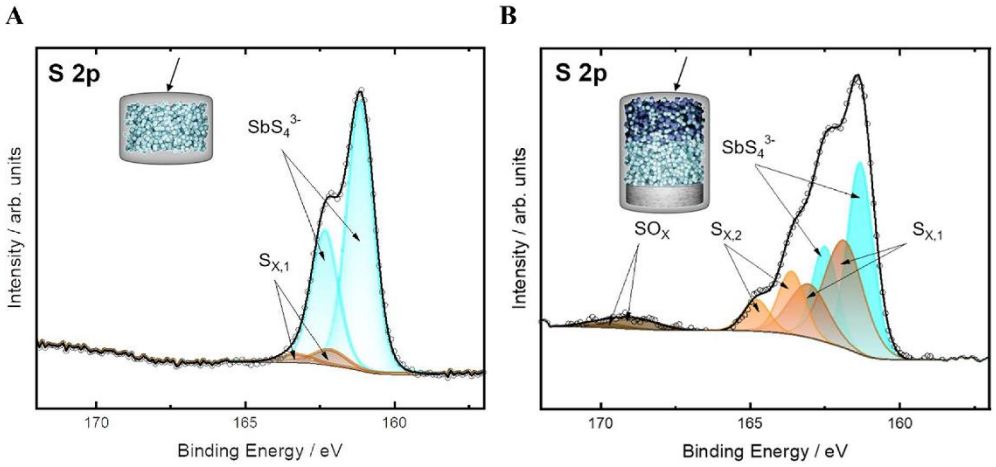

Figure 6. S 2p XP spectra of (A) Na_3SbS_4 solid electrolyte and (B) the cathode composite NFMM:Na_3SbS_4:C65. In turquoise is the expected sulfur peak for the SbS_4^{3-}. The pristine sample (A) shows polysulfide ($S_{X,1}$) contaminations from the synthesis in brown. The composite (B) shows additional degradation products corresponding to the formation of polysulfides ($S_{X,1}$ and $S_{X,2}$) and sulfoxides (SO_x) (different shades of brown).

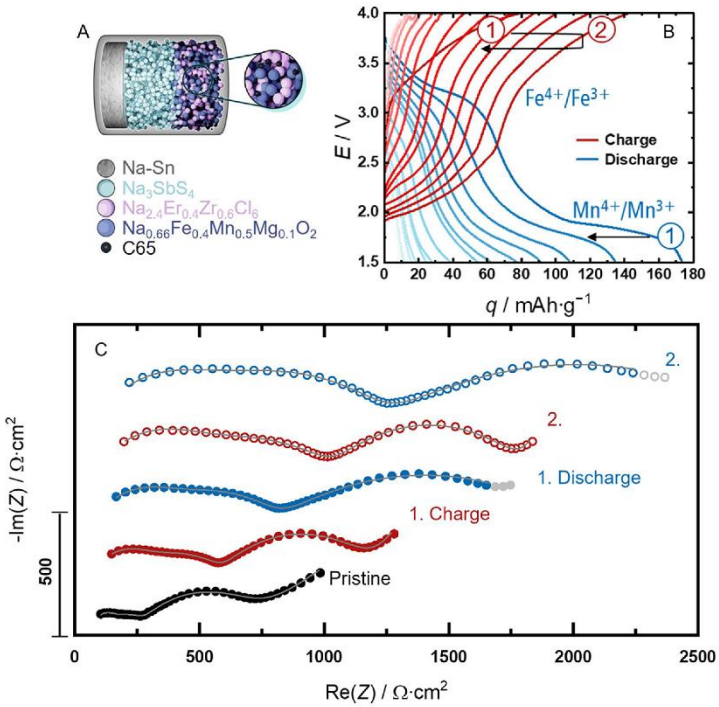

Figure 7. (A) Cell type Na−Sn|Na_3SbS_4|NFMM:NEZC:C65 with (B) the corresponding cycling curves obtained at a C-rate of 0.01C. The first and second charging (red) profiles and the first discharge step (blue) are labeled, and the arrows indicate the decreasing capacity retention with consecutive charge and discharge cycles. (C) The corresponding fitted impedance spectra show the pristine state (black), the impedance after the first charge (red), the first discharge (blue), the second charge step (open red), and the second discharge step (open blue). The fit contributions for each spectrum are shown in Figure S3.

which corroborates degradation of the sodium sulfide electrolyte at the interface with the CAM.

Cells with Na_3SbS_4 Separator and $Na_{2.4}Er_{0.4}Zr_{0.6}Cl_6$ Catholyte. One of the main advantages of solid-state batteries is the possibility to use different electrolytes as separator and catholyte depending on the specific needs. Overall, electrolytes should have a high ionic and low electronic conductivity, but solid electrolytes differ in their stability toward either the anode or the cathode (Figures S1 and S2). The decomposition of the sulfide electrolyte Na_3SbS_4 in the cathode composite was proven with TOF-SIMS and XPS. Hence, a different material was tested as the catholyte, namely $Na_{2.4}Er_{0.4}Zr_{0.6}Cl_6$ (NEZC). Lithium halide solid electrolytes have already been studied and show quite high stability at high potentials.[14,15] However,

https://doi.org/10.1021/acsami.4c01652
ACS Appl. Mater. Interfaces XXXX, XXX, XXX−XXX

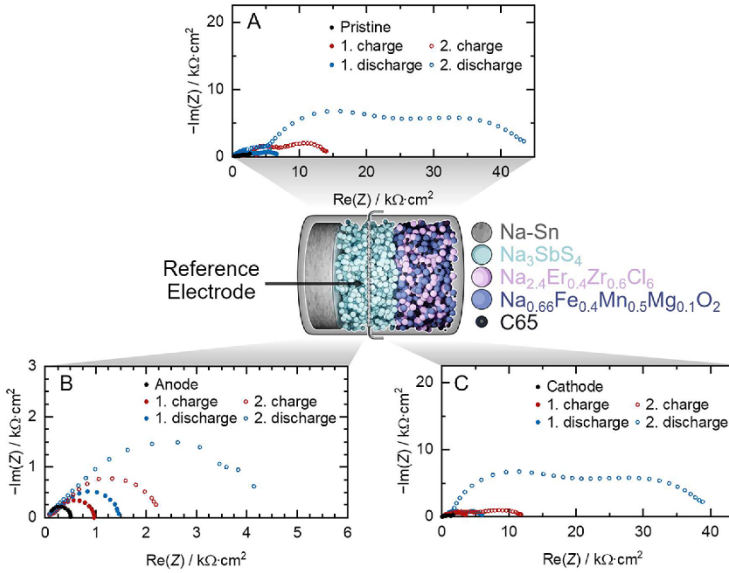

Figure 8. (A–C) Impedance measurements of a three-electrode cell with a reference electrode (RE) as sketched. Separated into (A) 3E full cell impedance, (B) anode impedance, and (C) cathode impedance, each shows the pristine case (black), after the first and second charge (red), and after the first and second discharge (blue) with increasing impedance per cycle. The data were published previously.[17]

compared with sulfide electrolytes, they suffer primarily from comparably low ionic conductivity.

Introducing NEZC as the catholyte enabled the cycling performance to reach the theoretical capacity of the CAM. It also made the comparison of voltage profiles of the CAM upon sodiation and desodiation with liquid electrolyte-based cells possible. Figure 7B shows the ASSB full cell (Na–Sn|Na_3SbS_4| NFMM:NEZC:C65) cycling performance.[17] The full cell is composed of the same sodium–tin alloy anode (Na–Sn) in contact with the Na_3SbS_4 solid electrolyte separator as used above. The cathode composite consisted of the sodium transition metal oxide NFMM mixed with NEZC as catholyte and carbon (C65) as an electronic conductor. The upper cutoff voltage was 4.0 V and the lower cutoff voltage was 1.5 V.

The shape of the cycling curves depends on the redox activity of the CAM, which is the NFMM in this case. For the cell using Na_3SbS_4 as catholyte, these cycling curves were hardly visible due to the fast reaching of the cutoff potential. The redox activity for the CAM (NFMM) was already studied in liquid cells.[17] It shows a redox activity of Fe^{4+}/Fe^{3+} at 3.5 V vs Na^+/Na and of Mn^{4+}/Mn^{3+} at 2.0 V vs Na^+/Na, which means in our case at 3.3 and 1.8 V if we consider the potential of 0.2 V vs Na^+/Na for the Na–Sn alloy anode. These two redox plateaus are especially distinct during the first discharge. For the first charging step, the capacity is lower than for the first discharge or second charging step since only the iron ions can be oxidized at that point. The redox potential of Fe^{4+}/Fe^{3+} is shifted to lower potentials than known from literature for the unsubstituted active material.[8]

The capacity vs cycle number plot in Figure 7B still shows a steady decrease of capacity with increasing cycle number, indicating unsolved issues such as degradation reactions at the interfaces or contact loss. In addition, the reason for capacity fading can be traced back presumably to an irreversible phase transition of the metal oxide CAM due to the redox reaction of manganese.[8]

3-Electrode Cells with Na_3SbS_4 Separator and $Na_{2.4}Er_{0.4}Zr_{0.6}Cl_6$ Catholyte. Furthermore, to prove that the major issue is caused by the cathode rather than the anode side, a quasi-reference electrode (RE) was introduced as described previously.[17] The RE was a gold wire coated with Sn with the purpose of measuring the cathode and anode impedance individually. A cell setup as introduced by Hertle et al.[19] was used. This setup has the advantage of using exactly the same conditions in terms of pressure as those of the full cells presented in Figure 2. The only difference is a higher separator thickness to avoid contact of the RE with either the anode or cathode.

Figure 8 depicts the three-electrode cell schematically. Figure 8A shows the full cell impedance for the pristine cell after charge and after discharge. Figure 8B and C, respectively, show the anode and cathode contributions in the pristine cell after charge and after discharge. The full cell reaches a resistance of more than 40 kΩ cm^2 that is consistent with adding up contributions of approximately 4 kΩ cm^2 from the anode impedance and close to 40 kΩ cm^2 from the cathode impedance. Even though the impedance of the anode also increases significantly, the major impedance contribution originates at the cathode.

Degradation of $Na_{2.4}Er_{0.4}Zr_{0.6}Cl_6$/CAM Composites. To address the question of contact loss or blocked ionic/electronic pathways in mixed cathode composites, SEM imaging was performed. An overview as well as a close up of a composite pellet of NFMM:C65:NEZC is presented in Figure S4, together with complementary EDX measurements in Figure S5. The SEM images show a homogeneous distribution of particles indicating minimization of blocked pathways. The pores and therefore point contacts, however, might lead to a high tortuosity as well as high resistances and a susceptibility to contact loss in case of volume expansion upon cycling.

To exclude decomposition of the chloride electrolyte from being the reason for capacity fading, TOF-SIMS and XPS

https://doi.org/10.1021/acsami.4c01652
ACS Appl. Mater. Interfaces XXXX, XXX, XXX–XXX

ACS Applied Materials & Interfaces www.acsami.org Research Article

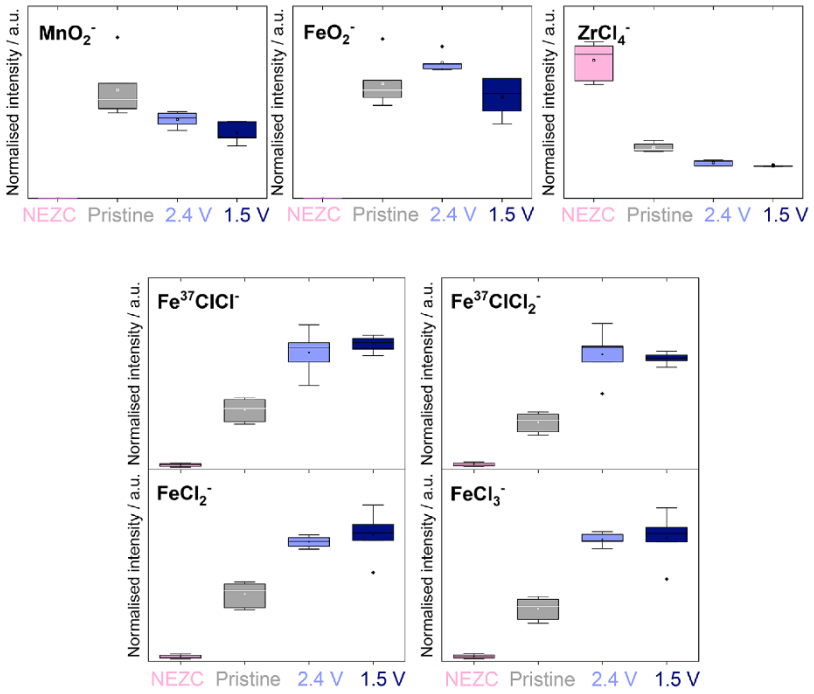

Figure 9. TOF-SIMS boxplot of 5 spots on a NEZC pellet (pink), a pristine NFMM:NEZC:C65 composite pellet (gray), a composite pellet cycled and discharged in a full cell to 2.4 V (light blue) and discharged to 1.5 V (dark blue), respectively. The boxplots for the 5 spots on each sample are shown for the fragments MnO_2^- and FeO_2^- representative for the active material NFMM, $ZrCl_4^-$ representative for the catholyte NEZC, as well as $Fe^{37}ClCl^-$, $Fe^{37}ClCl_2^-$, $FeCl_2^-$, and $FeCl_3^-$ representative for the interphase.

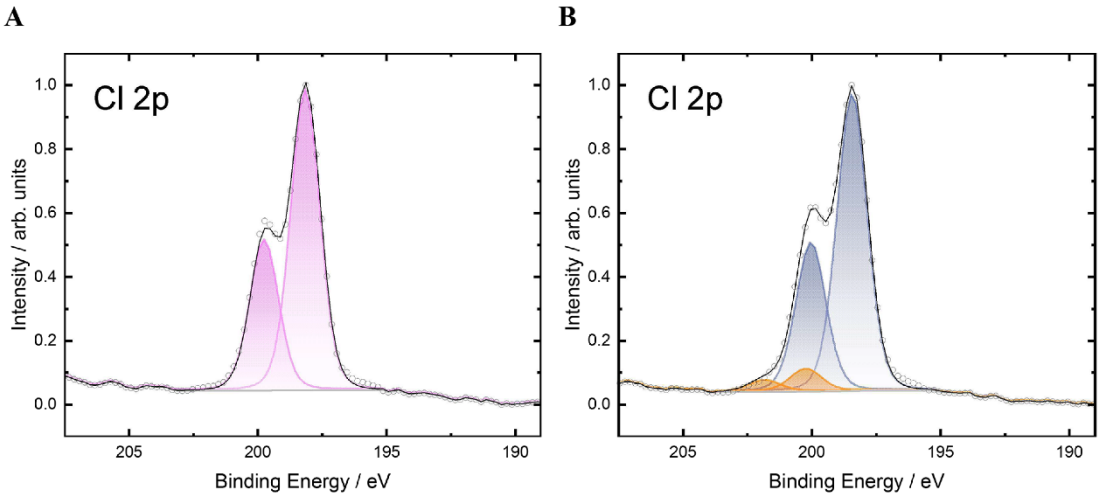

Figure 10. Cl 2p XP spectra calibrated to the Zr 3d signal (see Figure S6) of (A) NEZC and (B) the composite NFMM:NEZC:C65 (purple). The chlorine signal shows an additional doublet peak at higher binding energies for the composite (brown).

analyses were carried out. A selected group of measured fragments are presented in Figure 9. Each boxplot graph is representative for a specific fragment, showing the four different samples: NEZC, pristine cathode composite (NFMM:NEZC:C65), discharged in a full cell to 2.4 V and discharged to 1.5 V. The fragments MnO_2^- and FeO_2^- are expected for the CAM $Na_{0.66}Fe_{0.4}Mn_{0.5}Mg_{0.1}O_2$ and can therefore not be detected in the halide electrolyte NEZC. The $ZrCl_4^-$ is a fragment expected for the halide electrolyte and therefore also present in the composite samples. The fragments $FeCl_2^-$ and $FeCl_3^-$ as well as the respective chlorine isotopes $Fe^{37}ClCl^-$ and $Fe^{37}ClCl_2^-$ are the only fragments that combine the elements of CAM $Na_{0.66}\mathbf{Fe}_{0.4}Mn_{0.5}Mg_{0.1}O_2$ and catholyte $Na_{2.4}Er_{0.4}Zr_{0.6}\mathbf{Cl}_6$ that can be detected. As the precursors of the CAM are all metal sulfates, a signal intensity solely from the CAM with these fragments is excluded.

The method of TOF-SIMS relies on a collision cascade that leads to the detachment of individual surface atoms and

https://doi.org/10.1021/acsami.4c01652
ACS Appl. Mater. Interfaces XXXX, XXX, XXX−XXX

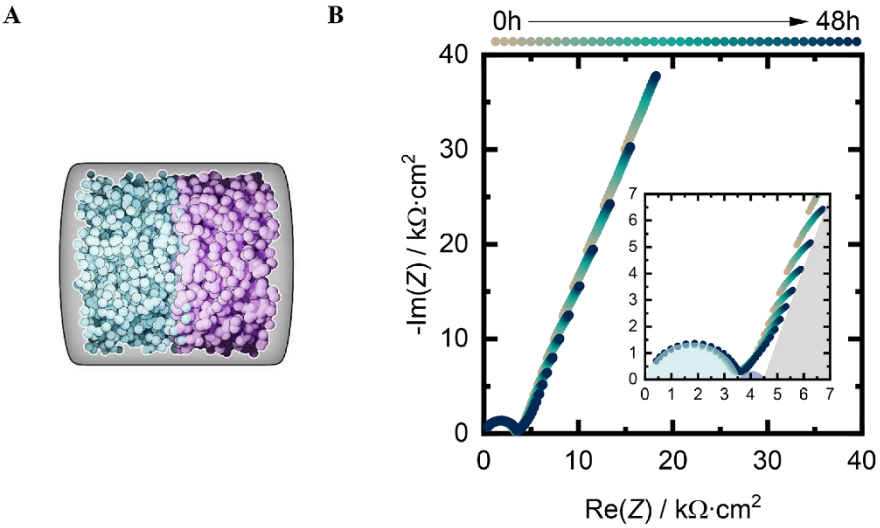

Figure 11. (A) Schematic representation of the cell setup for the impedance measurement of NEZC (pink) contacted with Na_3SbS_4 (blue) whose (B) impedance was measured over a period of 48 h indicated by color (beige to blue). The inlet shows a magnified view along with the corresponding fitted contributions for the measurement taken after 48 h. It includes the (*R*)(CPE) elements for the bulk (light blue) and interface resistance (purple), as well as the CPE element (gray) for the electronic resistance.

molecules. Fragments representing degradation products can be generated through a collision cascade upon bombardment with the primary ions. In the case of the four different fragments, all with the same elements, i.e., $FeCl_2^-$, $FeCl_3^-$, $Fe^{37}ClCl^-$, and $Fe^{37}ClCl_2^-$, a consistent increase in intensity for the cycled composites can be detected. This clearly supports the formation of a degradation product between the CAM and the solid electrolyte during cycling rather than the formation of a Fe_xCl_y species due to a collision cascade. It is noteworthy that the formation of Fe_xCl_y could potentially originate from a Zr−O formation which is known to possess a strong driving force, according to existing literature.[25] With SIMS measurements, however, Zr−O species were not clearly detectable. It is not excluded that these degradation products form a stable cathode electrolyte interface (CEI), which if ion-conducting and stable could even be advantageous.[26]

To support the findings from TOF-SIMS measurements, two different samples were prepared for XPS and the Cl 2 p signals for each are plotted in Figure 10. One sample is NEZC as catholyte as marked in magenta. The other is a cathode composite with NEZC as catholyte, NFMM as CAM and C65 as carbon additive after being cycled in an ASSB with Na_3SbS_4 and Na−Sn to 4.0 V and discharged to 2.4 V. The Cl 2p peak for the composite exhibits a second double peak (brown) at binding energies of 200.2 eV.

The unchanged Na 1s and Zr 3d signals (Figure S6) for the catholyte compared to the cycled composite support the assumption of a stable halide solid electrolyte upon cycling. However, the Cl 2p signal supports the TOF-SIMS measurements, indicating a chlorine species forming at higher binding energies such as a Fe_xCl_y species.

The Na_3SbS_4 | $Na_{2.4}Er_{0.4}Zr_{0.6}Cl_6$ Interface. As all-solid-state batteries allow to use two different electrolytes as separator and catholyte, not only their interface and properties toward the electrodes must be studied but also toward each other.[27,28] Therefore, Na_3SbS_4 and NEZC were contacted with a planar interface in a press cell setup, as it would be the case in a full cell, and the impedance was measured over time. Figure 11 shows the bulk impedance and interface contribution. The bulk impedance corresponds to an ionic conductivity of 0.03 mS cm^{-1} which is comparable to that of NEZC and the interface contribution increases over time (Table S1), indicating a chemical reaction between the catholyte and separator electrolyte. Additionally, the system was tested at −40 °C (Figure S8) and 80 °C (Figure S9) to resolve the process more clearly and to determine the thermodynamic and kinetic stability. At −40 °C the interface of the two electrolytes already shows a thermodynamic instability, which is increased kinetically at 80 °C (Figure S9). The bulk and interfacial resistances over the temperature range with intermediate measurements at 25 °C are shown in Figure S10.

Despite the interphase formation, the resistance for the measurement at 25 °C is comparably low after 48 h, compared to cells with Na_3SbS_4 as catholyte. The introduction of NEZC as the catholyte strongly increased the stability towards the active material, thus enabling the study of the cathode active material voltage profile (Figure 7).

To support this result, both electrolytes were mixed and ground and consequently studied using XPS. The XPS measurement (Figure S11) shows reaction products in the sulfur 2p spectrum and minor reaction products in the zirconium 3d spectrum. Combined with the impedance data, this implies a side reaction and formation of an interphase upon contact that, however, is less detrimental to the cell than the use of Na_3SbS_4 as catholyte.

To further increase the capacity retention, three different attempts were made. (1) The carbon additive C65 was exchanged by a vapor grown carbon fiber (VGCF) to increase the electron percolation network. (2) The full cell was cycled at 60 °C to increase the ionic conductivity of the catholyte. (3) Different lower cutoff voltages were tested to incorporate or exclude the redox activity of manganese.

Carbon Fiber Additives for improved Electron Percolation Network. Since the layered transition metal

https://doi.org/10.1021/acsami.4c01652
ACS Appl. Mater. Interfaces XXXX, XXX, XXX−XXX

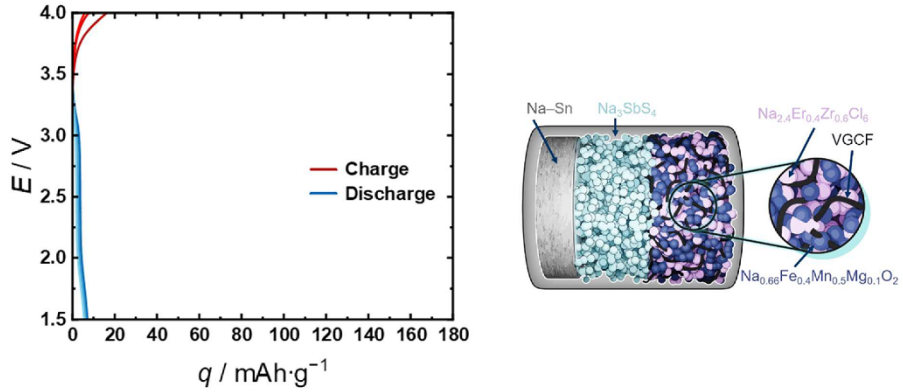

Figure 12. Charge (red) and discharge (blue) curves of a Na-ASSB with Na−Sn as anode, Na_3SbS_4 as separator electrolyte and a cathode composite comprising VGCF as carbon additive, Na_3SbS_4, and NFMM.

oxides with iron and manganese lack good electronic conductivity, carbon additives are essential to enable electronic transport inside the cathode. C65 is a spherical carbon with a large surface area. Especially in batteries with liquid electrolyte, but also in all-solid-state batteries VGCF (vapor grown carbon fibers) ranging in size from 20−200 μm have shown good results in cathodes.[10] VGCF transport the electrons from particles at the separator to the current collector faster than small spherical carbon particles. The use of carbon fibers with a fraction above 3 wt % of the cathode composite has shown to form an electronically well-connected network between the CAM particles. However, avoiding carbon agglomeration that hinders proper electronic transport is one of the challenges when using VGCF.

Simply exchanging C65 with VGCF revealed a poor cycling performance, as can be seen in Figure 12. The cell setup with NEZC as the catholyte and C65 as the carbon additive presented initial charging capacities of 80 mAh g^{-1} and discharge capacities of 172 mAh g^{-1}. On exchange of C65 with VGCF, the cell reaches only 16 mAh g^{-1} upon charge and 7 mAh g^{-1} upon discharge. The reason for such detrimental behavior can be traced back to blocked percolation pathways due to carbon fiber agglomerations combined with a low ionic conductivity of the halide electrolyte. Clearly, an improvement by using the highly favored carbon fibers rather than spherical carbon additive particles could not be achieved.

Imaging the compressed cathode composite pellet showed similar morphologies and distributions as those with C65. On the surface toward the current collector no clear sign of strong agglomeration of VGCF could be detected. However, pores and poor point contacts are clearly visible. Equally to the composite with C65 presented in Figure S3, two SEM magnifications are shown for the NFMM:NEZC:VGCF pellet in Figure S12. The EDX mapping Figure S13 once again shows energies for the elements oxygen (O $K_{\alpha 1}$), iron (Fe $L_{\alpha 1,2}$), manganese (Mn $L_{\alpha 1,2}$), and magnesium (Mg $K_{\alpha 1,2}$) specific for the CAM NFMM. The energies of the elements erbium (Er M_{α}), chloride (Cl $K_{\alpha 1}$), and zirconium (Zr $L_{\alpha 1}$) are specific for NEZC. The energy peak of sodium (Na $K_{\alpha 1,2}$) shows intensities for both the catholyte and the CAM.

The most important EDX mapping, compared to the one shown before, is the C $K_{\alpha 1,2}$ signal, which represents carbon fibers (VGCF). Three examples are marked with yellow circles and a yellow rectangle in the carbon mapping (Figure S13C) and the magnified SEM image (Figure S12). These are examples of the different microstructures that VGCF can form. Straight fibers (yellow rectangle) are the desired microstructure. Coiled and agglomerated fibers (yellow circles) can lead to high tortuosity and ion blocking areas. Compared to the EDX mapping of the C $K_{\alpha 1,2}$ signal for the composite with spherical C65 in Figure S4, the electronic transport network seems to be less homogeneous. The electronic transport is hence provided predominantly by the low electron-conducting CAM leading to a bad cycling performance as shown in Figure 12.

Cycling at 60 °C to Study the Cell Performance with Increased Ionic Conductivity of the Catholyte. As the NEZC catholyte has a low ionic conductivity (0.04 mS cm^{-1}) compared to the sulfide electrolyte Na_3SbS_4 (0.5 mS cm^{-1}), an increase in temperature should improve the cycling performance of the full cell as the ionic conductivity increases with temperature. Furthermore, improved mechanical properties are correlated with an increase in temperature. Sulfide electrolytes have a low Young's modulus (around 20 GPa)[29] which leads to a good distribution around the CAMs under pressure. Although halide electrolytes show comparatively good deformability around the CAM,[30,31] an increase in temperature[32] should be beneficial for a higher capacity retention, due to both, an even better contact of the catholyte to the CAM and, more importantly, faster ionic transport.

Figure 13 shows a full cell cycled at 60 °C at the same current density of 0.026 mA cm^{-2} as for the cell at 25 °C (Figure 7). Na−Sn is the anode material, and Na_3SbS_4 is the separator material. The composite is composed of NEZC as catholyte, NFMM as CAM and C65 as carbon additive. Compared to the cell cycled at 25 °C the initial charge capacity increased by 25 mAh g^{-1} to reach 104 mAh g^{-1}. The first discharge capacity, however, decreased by 35 mAh g^{-1} to reach only 138 mAh g^{-1}. The consecutive cycles also showed no increase in cycling stability.

The reason for that can be the increased decomposition of the Na_3SbS_4 separator at the cathode and anode interface, as well as with the halide catholyte as already mentioned (Figure S9). Another reason could be the imbalance of the higher ionic conductivity of the separator compared to the catholyte conductivity. This leads to a faster discharge/charge of the active particle at the separator side within the cathode composite. This faster de-/sodiation leads to a higher/lower

https://doi.org/10.1021/acsami.4c01652
ACS Appl. Mater. Interfaces XXXX, XXX, XXX−XXX

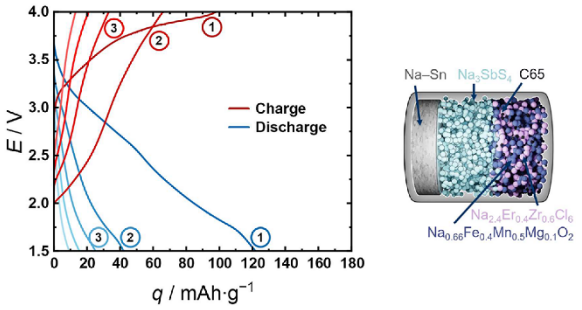

Figure 13. Charge (red) and discharge (blue) curves of a Na-ASSB with Na−Sn as anode, Na_3SbS_4 as separator electrolyte, and a cathode composite comprising C65, Na_3SbS_4, and NFMM cycled at 60 °C.

SOC compared to the rest of the composite cathode, increasing the degradation of the separator in contact with the few active particles at the cathode/separator interface.

Variation of Cutoff Voltage to Study the Redox Activity of Manganese. The role of the phase transition of the CAM discussed in literature upon using manganese as a redox active element was studied in the next step. For this purpose, five cells with the same composition, temperature, and pressure are cycled until different lower cutoff voltages are reached. The full cell composition is the same already shown for 25 °C (Figure 7) and 60 °C (Figure 13) (Na−Sn|Na_3SbS_4| NFMM:NEZC:C65). Figure 14 shows the five different cells. In red are the charge capacities, and in blue are the discharge capacities. The respective lower cutoff voltages are 2.4 V (filled cycle), which is equivalent with the pristine cell voltage, 2.2 V (triangle), 2.0 V (star), 1.8 V (square), and 1.5 V (vacant circle).

At 1.8 V vs Na−Sn manganese is reported to be redox active. As expected, all cells reach a first charge capacity of around 80 mAh g^{-1} upon charging to 4.0 V vs Na−Sn. This gives a good indication of the reproducibility of the cells. The first discharge capacities reach the highest capacities for the lower cutoff voltages 1.5 and 1.8 V, which is also expected as the reduction of manganese provides additional capacity. In the second charging step, the cell cycled to 1.5 V reaches the highest capacity. The other cells (1.8, 2.0, 2.2, and 2.4 V) follow a trend of decreasing capacities with increasing cutoff potential. This trend can be explained by the additional capacity gained from the oxidation of manganese at low potentials. As the cycle number increases, the cells cycled to lower voltages experience the lowest capacity retention. Regarding the discharge capacity within the first 10 cycles, the cell including the manganese redox reaction (1.5 V) exhibited a capacity retention of only 19%. The cell cycled to 2.4 V using only the iron redox reaction, on the other hand, reached a capacity retention of 64%.

As each of these cells was only cycled at 0.01C due to the low ionic conductivity of the relatively stable catholyte NEZC compared to Na_3SbS_4 as catholyte, 10 cycles take up to 820 h. During this time, one has to consider that not only the clearly irreversible redox activity of manganese in ASSBs, but also other processes such as the already mentioned degradation at the anode can lead to a capacity loss. Furthermore, chemical decomposition of the separator electrolyte at low voltages could add to stronger capacity fading. A capacity retention of only 64% therefore does not necessarily indicate an irreversible phase transformation of the CAM. However, when cells using manganese as a redox-active element are compared with cells using only iron as a redox-active element, strong irreversibility is observed.

CONCLUSIONS

Two different sodium solid catholytes were studied in an all-solid-state battery cell. The sulfide electrolyte Na_3SbS_4, also used as separator material, undergoes severe degradation upon contact and cycling with a transition metal oxide CAM as shown by TOF-SIMS, XPS and cycling data, analogous to reports for lithium analogues. The halide catholyte NEZC exhibits a much higher stability upon contact with the CAM. Cycling tests were performed showing the importance of the choice of the cutoff potential. XPS and TOF-SIMS showed only minor degradation products underlining the stability of the halide catholyte. The replacement of the catholyte showed the possibility of combining two different electrolytes as separator and catholyte highlighting one of the advantages of ASSB. However, our work also shows that ultimately stable and

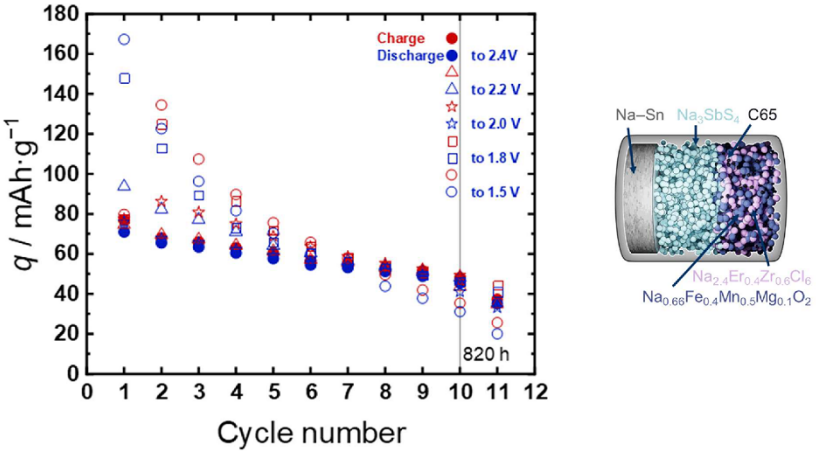

Figure 14. Five cells with the composition Na−Sn|Na_3SbS_4|NEZC:NFMM:C65 cycled 11 cycles at a C-rate of 0.01C at 25 °C. Each one charged to 4.0 V (red) and discharged (blue) to 2.4 V (filled circle), 2.2 V (triangle), 2.0 V (star), 1.8 V (square), and 1.5 V (empty circle), respectively.

https://doi.org/10.1021/acsami.4c01652
ACS Appl. Mater. Interfaces XXXX, XXX, XXX−XXX

highly ion-conducting solid electrolytes are still lacking for the application of sodium solid-state cells with high-voltage cathodes. Before considering studying the role of the composite microstructure in more detail, as done in lithium ASSBs, the future focus must be to achieve stable composites and material combinations of individual components with improved properties.

■ ASSOCIATED CONTENT

Supporting Information

The Supporting Information is available free of charge at https://pubs.acs.org/doi/10.1021/acsami.4c01652.

Stability window tests of Na_3SbS_4; fitted impedance spectra with corresponding resistance contributions for a cell type Na−Sn|Na_3SbS_4|NFMM:NEZC:C65 during cycling; SEM images of the cathode composites NFMM:NEZC:C65 and NFMM:NEZC:VGCF with corresponding EDX images; complementary Na 1s and Zr 3d XP spectra for the composite NFMM:NEZC:C65 and for NEZC; equivalent circuit parameters for the impedance measurement over time of the cell setup Na_3SbS_4|NEZC at 25 °C; fitted impedance spectra of the same cell setup at 25, −40, and 80 °C and an overview of the interface and bulk resistances with changing temperature; XP spectra of Na_3SbS_4 mixed with NEZC (PDF)

■ AUTHOR INFORMATION

Corresponding Author

Jürgen Janek − *Institute for Physical Chemistry and Center for Materials Research (ZfM), Justus Liebig University Giessen, Giessen 35392, Germany;* orcid.org/0000-0002-9221-4756; Email: juergen.janek@phys.chemie.uni-giessen.de, juergen.janek@pc.jlug.de

Authors

Laura E. Goodwin − *Institute for Physical Chemistry and Center for Materials Research (ZfM), Justus Liebig University Giessen, Giessen 35392, Germany*

Maya Ziegler − *Institute for Physical Chemistry and Center for Materials Research (ZfM), Justus Liebig University Giessen, Giessen 35392, Germany*

Paul Till − *Institute for Inorganic and Analytical Chemistry, University of Münster, Münster 48149, Germany*

Nazia Nazer − *Institute of Chemistry, Humboldt University Berlin, Berlin 12489, Germany*

Philipp Adelhelm − *Institute of Chemistry, Humboldt University Berlin, Berlin 12489, Germany;* orcid.org/0000-0003-2439-8802

Wolfgang G. Zeier − *Institute for Inorganic and Analytical Chemistry, University of Münster, Münster 48149, Germany; Institut für Energie-und Klimaforschung (IEK), IEK-12: Helmholtz-Institut Münster, Forschungszentrum Jülich, Münster 48149, Germany;* orcid.org/0000-0001-7749-5089

Felix H. Richter − *Institute for Physical Chemistry and Center for Materials Research (ZfM), Justus Liebig University Giessen, Giessen 35392, Germany;* orcid.org/0000-0002-6587-7757

Complete contact information is available at: https://pubs.acs.org/10.1021/acsami.4c01652

Author Contributions

The experiments presented in this publication were designed and executed by the first author L.E. Goodwin under the supervision of F.H. Richter and J. Janek. M. Ziegler helped in the fabrication of cells for the case study testing the same cell to different lower cutoff potentials. P. Till synthesized the sulfide electrolytes under the supervision of W.G. Zeier. N. Nazer synthesized the cathode active materials under the supervision of P. Adelhelm. Writing, reviewing, and editing was done by L. Goodwin as well as W.G. Zeier, F.H. Richter, P. Adelhelm and J. Janek.

Notes

The authors declare no competing financial interest.

■ ACKNOWLEDGMENTS

The authors acknowledge financial support from the Federal Ministry of Education and Research BMBF within the NASEBER consortium (03XP0187C) and DFG within the POLiS Cluster of Excellence (ID 390874152). We furthermore thank Felix Walther for the valuable scientific input in TOF-SIMS and XPS data analysis.

■ REFERENCES

(1) Vaalma, C.; Buchholz, D.; Weil, M.; Passerini, S. A Cost and Resource Analysis of Sodium-Ion Batteries. *Nat. Rev. Mater.* **2018**, *3* (4), 652.

(2) European Commission Directorate-General for Internal Market, Industry, Entrepreneurship, and SMEs; Grohol, M.; Veeh, C. *Study on the Critical Raw Materials for the EU 2023: Final Report*; Publications Office of the European Union, 2023.

(3) Lacivita, V.; Wang, Y.; Bo, S.-H.; Ceder, G. Ab Initio Investigation of the Stability of Electrolyte/Electrode Interfaces in All-Solid-State Na Batteries. *J. Mater. Chem. A* **2019**, *7* (14), 8144−8155.

(4) Robinson, J. B.; Finegan, D. P.; Heenan, T. M. M.; Smith, K.; Kendrick, E.; Brett, D. J. L.; Shearing, P. R. Microstructural Analysis of the Effects of Thermal Runaway on Li-Ion and Na-Ion Battery Electrodes. *J. Electrochem. En. Conv. Stor.* **2018**, *15* (1), 011010.

(5) Walther, F.; Koerver, R.; Fuchs, T.; Ohno, S.; Sann, J.; Rohnke, M.; Zeier, W. G.; Janek, J. Visualization of the Interfacial Decomposition of Composite Cathodes in Argyrodite-Based All-Solid-State Batteries Using Time-of-Flight Secondary-Ion Mass Spectrometry. *Chem. Mater.* **2019**, *31* (10), 3745−3755.

(6) Koerver, R.; Aygün, I.; Leichtweiß, T.; Dietrich, C.; Zhang, W.; Binder, J. O.; Hartmann, P.; Zeier, W. G.; Janek, J. Capacity Fade in Solid-State Batteries: Interphase Formation and Chemomechanical Processes in Nickel-Rich Layered Oxide Cathodes and Lithium Thiophosphate Solid Electrolytes. *Chem. Mater.* **2017**, *29* (13), 5574−5582.

(7) Kwak, H.; Wang, S.; Park, J.; Liu, Y.; Kim, K. T.; Choi, Y.; Mo, Y.; Jung, Y. S. Emerging Halide Superionic Conductors for All-Solid-State Batteries: Design, Synthesis, and Practical Applications. *ACS Energy Lett.* **2022**, *7* (5), 1776−1805.

(8) Nayak, P. K.; Yang, L.; Pollok, K.; Langenhorst, F.; Wondraczek, L.; Adelhelm, P. Electrochemical Performance and Ageing Mechanisms of Sol-Gel Synthesized $Na_{2/3}[Mn_{3/5}Fe_{2/5}]O_2$ for Sodium-Ion Batteries. *Batter. Supercaps.* **2019**, *2* (1), 104−111.

(9) Zhang, W.; Leichtweiß, T.; Culver, S. P.; Koerver, R.; Das, D.; Weber, D. A.; Zeier, W. G.; Janek, J. The Detrimental Effects of Carbon Additives in $Li_{10}GeP_2S_{12}$-Based Solid-State Batteries. *ACS Appl. Mater. Interfaces* **2017**, *9* (41), 35888−35896.

(10) Randau, S.; Walther, F.; Neumann, A.; Schneider, Y.; Negi, R. S.; Mogwitz, B.; Sann, J.; Becker-Steinberger, K.; Danner, T.; Hein, S.; Latz, A.; Richter, F. H.; Janek, J. On the Additive Microstructure in Composite Cathodes and Alumina-Coated Carbon Microwires for

Improved All-Solid-State Batteries. *Chem. Mater.* **2021**, *33* (4), 1380−1393.
(11) Walther, F.; Randau, S.; Schneider, Y.; Sann, J.; Rohnke, M.; Richter, F. H.; Zeier, W. G.; Janek, J. Influence of Carbon Additives on the Decomposition Pathways in Cathodes of Lithium Thiophosphate-Based All-Solid-State Batteries. *Chem. Mater.* **2020**, *32* (14), 6123−6136.
(12) Usiskin, R.; Maier, J. Interfacial Effects in Lithium and Sodium Batteries. *Adv. Energy Mater.* **2021**, *11* (2), No. 2001455.
(13) Zhang, W.; Richter, F. H.; Culver, S. P.; Leichtweiss, T.; Lozano, J. G.; Dietrich, C.; Bruce, P. G.; Zeier, W. G.; Janek, J. Degradation Mechanisms at the $Li_{10}GeP_2S_{12}$/$LiCoO_2$ Cathode Interface in an All-Solid-State Lithium-Ion Battery. *ACS Appl. Mater. Interfaces* **2018**, *10* (26), 22226−22236.
(14) Qie, Y.; Wang, S.; Fu, S.; Xie, H.; Sun, Q.; Jena, P. Yttrium-Sodium Halides as Promising Solid-State Electrolytes with High Ionic Conductivity and Stability for Na-Ion Batteries. *J. Phys. Chem. Lett.* **2020**, *11* (9), 3376−3383.
(15) Wu, E. A.; Banerjee, S.; Tang, H.; Richardson, P. M.; Doux, J.-M.; Qi, J.; Zhu, Z.; Grenier, A.; Li, Y.; Zhao, E.; et al. A Stable Cathode-Solid Electrolyte Composite for High-Voltage, Long-Cycle-Life Solid-State Sodium-Ion Batteries. *Nat. Commun.* **2021**, *12* (1), 1256.
(16) Schlem, R.; Banik, A.; Eckardt, M.; Zobel, M.; Zeier, W. G. $Na_{3-x}Er_{1-x}Zr_xCl_6$ — A Halide-Based Fast Sodium-Ion Conductor with Vacancy-Driven Ionic Transport. *ACS Appl. Energy Mater.* **2020**, *3* (10), 10164−10173.
(17) Goodwin, L. E.; Till, P.; Bhardwaj, M.; Nazer, N.; Adelhelm, P.; Tietz, F.; Zeier, W. G.; Richter, F. H.; Janek, J. Protective NaSICON Interlayer between a Sodium-Tin Alloy Anode and Sulfide-Based Solid Electrolytes for All-Solid-State Sodium Batteries. *ACS Appl. Mater. Interfaces* **2023**, *15* (43), 50457−50468.
(18) Zhang, W.; Weber, D. A.; Weigand, H.; Arlt, T.; Manke, I.; Schröder, D.; Koerver, R.; Leichtweiss, T.; Hartmann, P.; Zeier, W. G.; Janek, J. Interfacial Processes and Influence of Composite Cathode Microstructure Controlling the Performance of All-Solid-State Lithium Batteries. *ACS Appl. Mater. Interfaces* **2017**, *9* (21), 17835−17845.
(19) Hertle, J.; Walther, F.; Mogwitz, B.; Schröder, S.; Wu, X.; Richter, F. H.; Janek, J. Miniaturization of Reference Electrodes for Solid-State Lithium-Ion Batteries. *J. Electrochem. Soc.* **2023**, *170* (4), 040519.
(20) Minnmann, P.; Quillman, L.; Burkhardt, S.; Richter, F. H.; Janek, J. Editors' Choice—Quantifying the Impact of Charge Transport Bottlenecks in Composite Cathodes of All-Solid-State Batteries. *Prog. Energy* **2021**, *168* (4), 040537.
(21) Stratford, J. M.; Mayo, M.; Allan, P. K.; Pecher, O.; Borkiewicz, O. J.; Wiaderek, K. M.; Chapman, K. W.; Pickard, C. J.; Morris, A. J.; Grey, C. P. Investigating Sodium Storage Mechanisms in Tin Anodes: A Combined Pair Distribution Function Analysis, Density Functional Theory, and Solid-State NMR Approach. *J. Am. Chem. Soc.* **2017**, *139* (21), 7273−7286.
(22) Ellis, L. D.; Hatchard, T. D.; Obrovac, M. N. Reversible Insertion of Sodium in Tin. *J. Electrochem. Soc.* **2012**, *159* (11), A1801−A1805.
(23) Doux, J.-M.; Nguyen, H.; Tan, D. H. S.; Banerjee, A.; Wang, X.; Wu, E. A.; Jo, C.; Yang, H.; Meng, Y. S. Stack Pressure Considerations for Room-Temperature All-Solid-State Lithium Metal Batteries. *Adv. Energy Mater.* **2020**, *10* (1), No. 1903253.
(24) Chastain, J., Ed. *Handbook of X-Ray Photoelectron Spectroscopy:A Reference Book of Standard Spectra for Identification and Interpretation of XPS Data*; [Reprint of the 1992 version]; Physical Electronics, Inc, 1995.
(25) Smetaczek, S.; Pycha, E.; Ring, J.; Siebenhofer, M.; Ganschow, S.; Berendts, S.; Nenning, A.; Kubicek, M.; Rettenwander, D.; Limbeck, A.; Fleig, J. Investigating the Electrochemical Stability of $Li_7La_3Zr_2O_{12}$ Solid Electrolytes Using Field Stress Experiments. *J. Mater. Chem. A* **2021**, *9* (27), 15226−15237.
(26) Park, D.; Kim, K.; Chun, G. H.; Wood, B. C.; Shim, J. H.; Yu, S. Materials Design of Sodium Chloride Solid Electrolytes Na_3MCl_6 for All-Solid-State Sodium-Ion Batteries. *J. Mater. Chem. A* **2021**, *9* (40), 23037−23045.
(27) Rosenbach, C.; Walther, F.; Ruhl, J.; Hartmann, M.; Hendriks, T. A.; Ohno, S.; Janek, J.; Zeier, W. G. Visualizing the Chemical Incompatibility of Halide and Sulfide-Based Electrolytes in Solid-State Batteries. *Adv. Energy Mater.* **2023**, *13* (6), 2203673.
(28) Riegger, L. M.; Schlem, R.; Sann, J.; Zeier, W. G.; Janek, J. Lithium-Metal Anode Instability of the Superionic Halide Solid Electrolytes and the Implications for Solid-State Batteries. *Angew. Chem.* **2021**, *133* (12), 6792−6797.
(29) Sakuda, A.; Hayashi, A.; Tatsumisago, M. Sulfide Solid Electrolyte with Favorable Mechanical Property for All-Solid-State Lithium Battery. *Sci. Rep.* **2013**, *3*, 2261.
(30) Han, Y.; Jung, S. H.; Kwak, H.; Jun, S.; Kwak, H. H.; Lee, J. H.; Hong, S.-T.; Jung, Y. S. Single- or Poly-Crystalline Ni-Rich Layered Cathode, Sulfide or Halide Solid Electrolyte: Which Will be the Winners for All-Solid-State Batteries? *Adv. Energy Mater.* **2021**, *11* (21), 2100126.
(31) Asano, T.; Sakai, A.; Ouchi, S.; Sakaida, M.; Miyazaki, A.; Hasegawa, S. Solid Halide Electrolytes with High Lithium-Ion Conductivity for Application in 4 V Class Bulk-Type All-Solid-State Batteries. *Advanced materials (Deerfield Beach, Fla.)* **2018**, *30* (44), No. e1803075.
(32) Zakarian, D.; Khachatrian, A.; Firstov, S. Universal Temperature Dependence of Young's Modulus. *Met. Powder Rep.* **2019**, *74* (4), 204−206.

https://doi.org/10.1021/acsami.4c01652
ACS Appl. Mater. Interfaces XXXX, XXX, XXX−XXX

4. Conclusion and Outlook

The study of sodium all-solid-state batteries with sodium tin alloy as the anode and transition metal oxides as the cathode active material has provided valuable insights into the intricate interplay of various components within the battery system. Employing advanced analytical techniques such as X-ray photoelectron spectroscopy, time-of-flight secondary ion mass spectrometry and scanning electron microscopy, we aimed to elucidate the nuances affecting the overall cycling performance and identify weak points in the system.

One of the key advantages of all-solid-state batteries lies in their potential to employ different electrolytes not only as catholyte but also as a separator. This flexibility allows for customization of the battery architecture, presenting an opportunity to enhance performance and address specific challenges. Throughout our investigation we employed two distinct electrolytes as catholyte (Na_3SbS_4 and $Na_{2.4}Er_{0.4}Zr_{0.6}Cl_6$) and two as separator ($Na_3SbS_4$ and $Na_{2.9}Sb_{0.9}W_{0.1}S_4$), while also introducing NaSICON ($Na_{3.4}Zr_2Si_{2.4}P_{0.6}O_{12}$) as a protective layer.

Our findings revealed a marked differentiation in the performance of sulfide and halide catholytes. The sulfide catholyte Na_3SbS_4 exhibited severe degradation upon contact and cycling with transition metal oxide cathode active materials analogous to cells with lithium sulfide solid electrolytes. Conversely, the halide catholyte $Na_{2.4}Er_{0.4}Zr_{0.6}Cl_6$ demonstrated higher stability when in contact with transition metal oxide cathode active materials, with only minor degradation products detected.

The investigation into separator materials Na_3SbS_4 and $Na_{2.9}Sb_{0.9}W_{0.1}S_4$ revealed reactions with the sodium-tin alloy anode over time highlighting a critical issue that could compromise the long-term stability of the battery. The introduction of NaSICON as a protective layer proved to be effective in stabilizing the separator materials, emphasizing the importance of thoughtful design in achieving robust all-solid-state batteries.

Battery cycling experiments underscored the significance of cut-off potentials, revealing the delicate balance required for optimal performance. Our work, while providing valuable insights into the current state of sodium all-solid-stat batteries, also illuminated the challenges associated with achieving ultimate sodium solid electrolytes possessing high ionic conductivity and redox stability, especially when coupled with high voltage cathodes.

Looking ahead it is evident that there is a demand for stable composites, not just individual components with enhanced properties. The emphasis should be on developing the synergy among these components, a crucial factor that must be carefully considered for the success of a sodium all-solid-state battery. Currently, the “NaSICON” materials are still too rigid and thick. Excessive thickness results in both volumetric and gravimetric energy density loss, as NaSICON serves “only” as a separator material or

protective anode layer without actively participating in the cell reaction. Therefore, for industrial applications of all-solid-state cells, NaSICON materials are not yet suitable. A potential solution could involve the usage of thinner sheets, which, however, make the processability even more challenging or to increase the binder content in electrodes to incorporate NaSICON materials. Despite their advantageous high ionic conductivity, sulfide electrolytes react heavily with the sodium anode materials and high voltage cathode materials tested in this study. The use of a NaSICON sheet as a separator or anode protection opens up the possibility of using sodium metal as an anode material, thereby increasing the energy density. While sulfide electrolytes possess the required softness to make excellent catholytes, the unavoidable need to coat especially the cathode active materials arises. In comparing halide and sulfide electrolytes, a significant advantage of sulfides lies in their cost-effectiveness and abundance of elements compared to the elements currently used in halide materials. A substantial effort is required to enhance the ionic conductivity of halides to make them competitive with sulfides in all-solid-state batteries. Additionally, a more thorough investigation into the stability of halides is necessary since the exact nature of their reaction at the cathode is not entirely certain from the conducted experiments. It is crucial to determine whether a stable cathode–electrolyte interface or a mixed conducting interface at the cathode is formed, as the latter could lead to long-term capacity fading. In terms of engineering aspects of sodium all-solid-state cells, a deeper understanding of the importance of particle sizes, especially in cathode composites, is necessary. Furthermore, studies on the necessary pressures to compensate for volume changes, as well as investigations into the morphologies of sodium alloys a sodium metal during stripping and plating, are essential for future developments.

5. Appendix

5.1. Supporting Information Publication I

Supporting information

Protective NaSICON Interlayer Between a Sodium-Tin Alloy Anode and Sulfide-based Solid Electrolytes for All-Solid-State Sodium Batteries

Laura E. Goodwin[a,b], *Paul Till*[c], *Monika Bhardwaj*[d], *Nazia Nazer*[e], *Philipp Adelhelm*[e], *Frank Tietz*[d], *Wolfgang G. Zeier*[c,f], *Felix H. Richter*[a,b], *and Jürgen Janek*[a,b,*]

[a] Institute for Physical Chemistry, Justus Liebig University Giessen, 35392 Giessen, Germany.
*E-Mail: juergen.janek@phys.chemie.uni-giessen.de

[b] Center for Materials Research (ZfM), Justus Liebig University Giessen, 35392 Giessen, Germany.

[c] Institute for Inorganic and Analytical Chemistry, University of Münster, 48149 Münster, Germany.

[d] Forschungszentrum Jülich GmbH, Institute of Energy and Climate Research, Materials Synthesis and Processing (IEK-1), 52425 Jülich, Germany.

[e] Institute of Chemistry, Humboldt University Berlin, 12489 Berlin, Germany.

[f] Institut für Energie- und Klimaforschung (IEK), IEK-12: Helmholtz-Institut Münster, Forschungszentrum Jülich, 48149 Münster, Germany.

5. Appendix

Index

Material Synthesis

$Na_3Sn/Na_{15}Sn_4$. Na-Sn was prepared in argon atmosphere in batches of 2 g by ball milling. Tin powder (100 mesh, 99.999% from Fisher Scientific GmbH) was alloyed with elemental Na (BASF SE) in a stoichiometric ratio for $Na_{15}Sn_4$ with a 1.05 wt.% excess of sodium, due to the loss at the cup wall and milling media. The media-to-sample weight ratio was 40:1, the media being 5 mm ZrO_2 balls in a 45 mL ball milling cup. The synthesis was carried out for 20 h with intervals of 10 min of milling at 510 rpm and 10 min of resting time. The powder was subsequently mortared for 20 min by hand.

$Na_{2.4}Er_{0.4}Zr_{0.6}Cl_6$. $Na_{2.4}Er_{0.4}Zr_{0.6}Cl_6$ (NEZC) was prepared in argon atmosphere as described by Schlem et al.[1] resulting in a catholyte with an ionic conductivity of 0.04 $mS \cdot cm^{-1}$. NaCl (Merck, 99.5% pre-dried at 200 °C for 48 h under dynamic vacuum), $ErCl_3$ (Sigma Aldrich, 99%) and $ZrCl_4$ (Alfa Aesar, 99.5%) were mixed with an excess of $ErCl_3$ of 10 wt.% and reacted using the ball milling method. In a 30:1 mass ratio of milling media (5 mm ZrO_2 balls) to precursor powder, the reaction was conducted in 99 milling cycles with 15 min of running time at 500 rpm and 5 min rest.

$Na_{0.66}Fe_{0.4}Mn_{0.5}Mg_{0.1}O_2$. The layered oxide $Na_{0.66}Fe_{0.4}Mn_{0.5}Mg_{0.1}O_2$ (NFMM) was synthesized by carbonate co-precipitation. The reaction vessel was heated to 55 °C in a water bath. Stoichiometric amounts of $FeSO_4 \cdot 7H_2O$ (Merck), $MnSO_4 \cdot H_2O$ (Alfa Aesar), $MgSO_4$ (Sigma Aldrich) were dissolved in water to obtain a 2 M aqueous solution. This solution was added dropwise using a dropping funnel to the reactor vessel. 2 M Na_2CO_3 (Alfa Aesar) – 0.2 M NH_4OH (Sigma Aldrich) base solution was also prepared and added dropwise to the reaction vessel, so that the pH of the reaction mixture, monitored with a SevenCompact pH meter S220 (Mettler Toledo), was always maintained between 7.5 and 8. Afterwards, the precipitated (Fe, Mn, Mg) carbonate was allowed to mature with continuous stirring at room temperature and then washed with water using a centrifuge (Rotina 380, Hettich) to remove the sulfate anions. The precipitate was then dried at 60 °C in air atmosphere, before drying was continued overnight under vacuum at 120 °C. Then, the as-obtained metal carbonate precursor was mixed with Na_2CO_3 in the required stoichiometry, ground and heated to 500 °C for 6 h (300 °C/h heating rate, air atmosphere, oven: Nabertherm). Subsequently, the material was re-ground and heated to 900 °C, for 12 h (300 °C/h). The calcination product was allowed to cool to room temperature (60 °C/h) prior to being transferred into an argon-filled glovebox (Braun, $p(O_2)/p < 0.1$ ppm, $p(H_2O)/p < 0.1$ ppm).

Na_3SbS_4 and $Na_{2.9}Sb_{0.9}W_{0.1}S_4$. The sulfide-type separator materials Na_3SbS_4 and $Na_{2.9}Sb_{0.9}W_{0.1}S_4$ were synthesized by solid-state reaction in inert atmosphere using a sealed ampoule. Before use, the ampoules were dried under dynamic vacuum at 800 °C for 2 h to remove all traces of water. All syntheses were carried out in argon-filled gloveboxes. The precursors Na_2S (Sigma Aldrich), S (Acros Organics, 99.999%), WS_2 (chemPur, 99.98%) and Sb_2S_3 were mixed in stoichiometric ratios in an agate mortar for 20 min. The mixture was then pressed into a pellet, loaded into an ampoule and sealed under vacuum. The sample was heated in a tube furnace up to 550 °C with a heating ramp of 30 °C/h, dwelled for 20 h and was left in the furnace afterwards to cool down naturally. The ampoule was then transferred to a glovebox and the obtained pellet was ground to a powder for further use.

$Na_{3.4}Zr_2Si_{2.4}P_{0.6}O_{12}$ (NZSPO) **– (A) Slurry preparation.** An alcohol-based suspension was prepared using NZSPO ceramic powder. The synthesis of the NZSPO powder has been reported elsewhere[2,3]. The solvent of the suspension containing 25 vol% of ceramic powder was based on an azeotropic mixture of ethanol (67 vol%) and methyl ethyl ketone (33 vol%); organic additives such as 5 wt.% polyvinyl butyral (PVB-98) as a binder and 3 wt.% of Solusolve® 2075 (Solutia Inc.) and 2 wt.% of PEG400® (Merck) as plasticizers were added to stabilize the suspension. To obtain a homogeneous dispersion, the slurry was mixed in a planetary mixer at 1500 rpm for 8 min and continuously ball milled for 12 h. To eliminate bubbles, the slurry was degassed by stirring in a vacuum chamber for 2 h. – **(B) Tape casting and sintering process.** The slurry was tape-cast on a polymeric foil with a slit height of 600 µm at the doctor blade to obtain densified layer of about 100-200 µm (see Figure S31) depending on the velocity of the transported foil. During sintering process, the samples were sandwiched between two NZSPO pellets to ensure flat surfaces which is extremely important for cell assembly and electrochemical tests. Samples with diameters of 8 mm were punched out from the dried green tape and slowly heated up to 600 °C for 2 h to remove all organic components. Subsequently, final sintering was carried out at 1265 °C for 5 h.

Material characterization

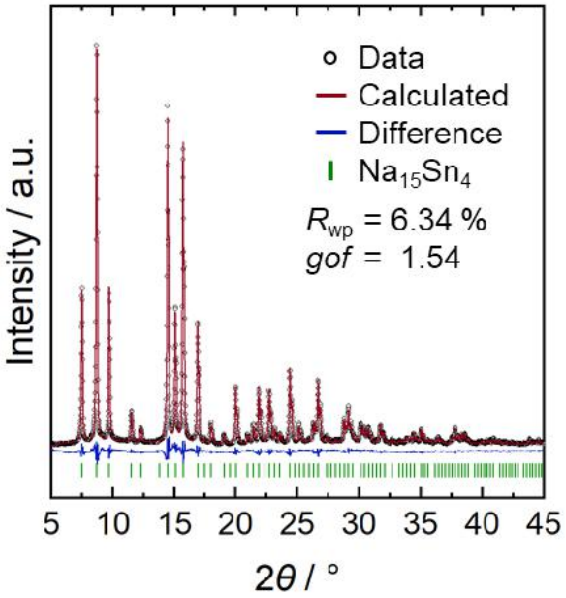

Figure S1: Rietveld-refinement against X-ray diffraction data of the Na-Sn anode material. Obtained structural data are given in Table S2.

Table S 1: Structural data from the refinement of the Na-Sn anode material.

$Na_{15}Sn_4$

Lattice Parameter $a = b = c = 13.2208(6)$

$R_{wp} = 6.34$ %, $R_{exp} = 4.11$, Goodness of fit: 1.54

Space group: $I\bar{4}3d$ Impurity phase: -

Atom	**Wyckoff position**	**Atomic coordinates**			***Occ.***	***B*iso / Å²**
		x	***y***	***z***		
Na1	12*a*	0.375	0	0.25	1	3.9(6)
Na2	48*e*	0.6243(9)	0.6506(9)	0.4596(9)	1	3.2(2)
Sn	16*c*	0.7084(2)	0.7084(2)	0.7084(2)	1	2.38(6)

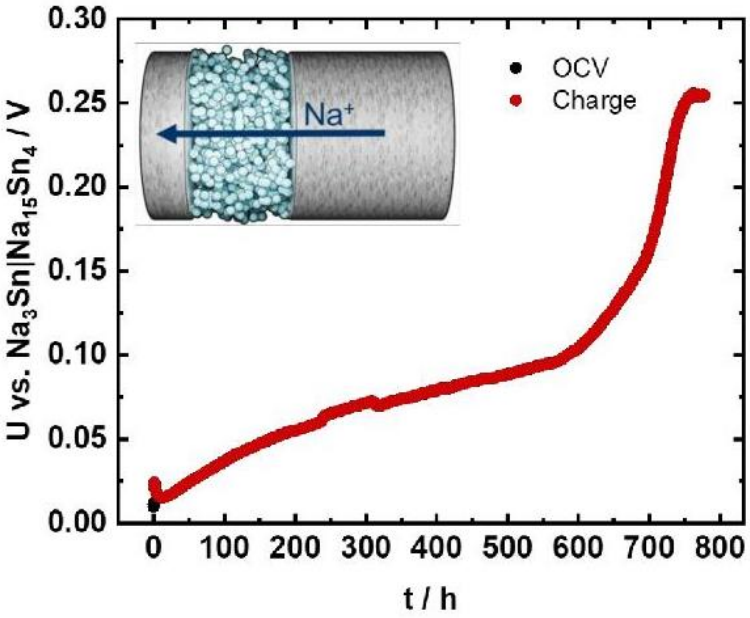

Figure S2: Stability test of the anode potential of a Na-Sn(20 mg)|Na_3SbS_4(50 mg)|Na-Sn(100 mg) cell during sodiation of the 20 mg $Na_3Sn/Na_{15}Sn_4$ (Na-Sn) anode for 778 h. Equivalent to the 0.1 C used for full cell cycling, a stripping current of 24 $\mu A \cdot cm^{-2}$ is applied. The expected potential drop to −0.2 V during changing from the two-phase mixture $Na_3Sn/Na_{15}Sn_4$ to $Na/Na_{15}Sn_4$ is not reached, suggesting the immediate reaction of Na^0 with the solid electrolyte. The strong increase after ~600 h to 0.25 V suggests a phase transition from $Na_3Sn/Na_{15}Sn_4$ to Na_9Sn_4/Na_3Sn at the stripped electrode. Using the capacity at the plateau after 760 h (14.41 mAh) a ratio of 41% $Na_{15}Sn_4$ and 59% Na_3Sn can be calculated. Even though the XRD does not indicate such a high fraction of Na_3Sn in the Na-Sn alloy, this experiments proves that the two-phase region of $Na_3Sn/Na_{15}Sn_4$ (Na-Sn) used as anode has a stable potential upon charging (100 h) when it is applied in a full cell (50 mg).

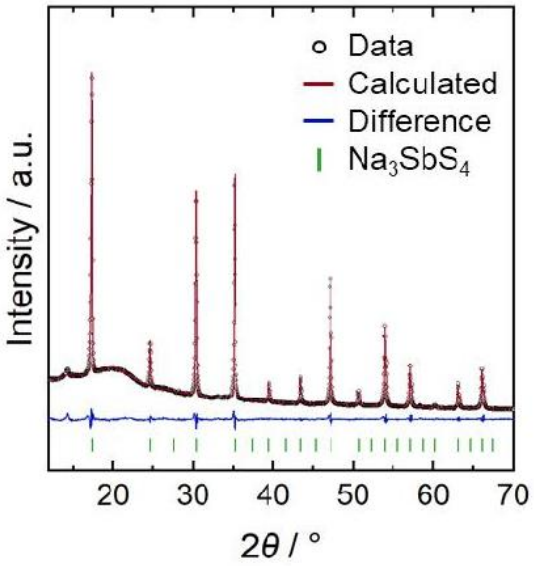

Figure S3: Pawley-fit against X-ray diffraction data of the Na_3SbS_4 SE. The increased background signal intensity at 20° can be attributed to Kapton foil used to cover the air-sensitive samples. Obtained lattice parameters are shown in Table S2.

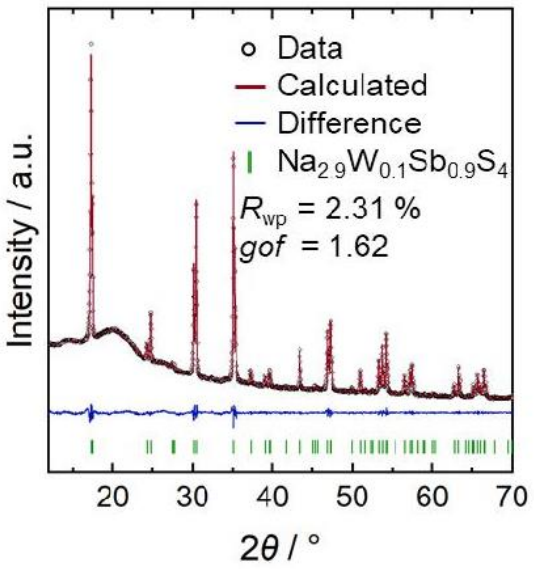

Figure S4: Pawley-fit against X-ray diffraction data of the $Na_{2.9}Sb_{0.9}W_{0.1}S_4$ SE. The increased background signal intensity at 20° can be attributed to Kapton foil used to cover the air-sensitive samples. Obtained lattice parameters are shown in Table S2.

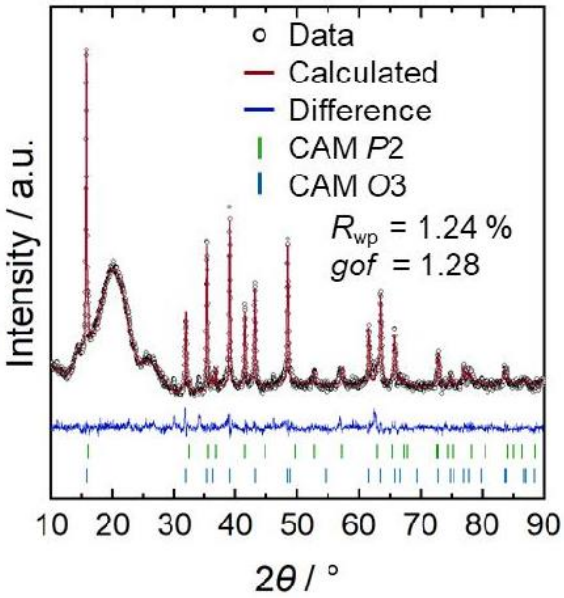

Figure S5: Pawley-fit against X-ray diffraction data of the $Na_{0.66}Fe_{0.4}Mn_{0.5}Mg_{0.1}O_2$ cathode active material. The increased background signal intensity at 20° can be attributed to Kapton foil used to cover the air-sensitive samples. Obtained lattice parameters of the *P*2 and *O*3 polymorphs are shown in Table S2.

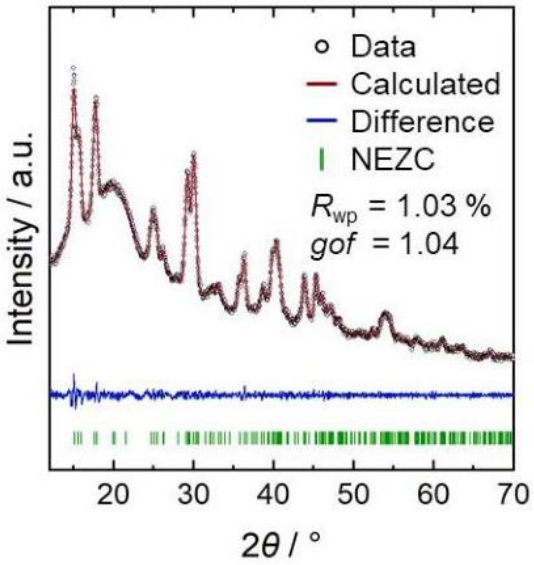

Figure S6: Pawley-fit against X-ray diffraction data of the $Na_{2.4}Er_{0.4}Zr_{0.6}Cl_6$ SE. The increased background signal intensity at 20° can be attributed to Kapton foil used to cover the air-sensitive samples. Obtained lattice parameters are shown in Table S2.

Table S2: Obtained lattice parameters and space group for Pawley-fits against diffraction data of the cathode active material $Na_{0.66}Fe_{0.4}Mn_{0.5}Mg_{0.1}O_2$ and the solid electrolytes Na_3SbS_4, and $Na_{2.4}Er_{0.4}Zr_{0.6}Cl_6$.

	Lattice Parameter	**Space Group**
Na_3SbS_4	a = 7.1633(3) Å c = 7.2951(3) Å	$P\bar{4}2_1c$
$Na_{2.9}W_{0.1}Sb_{0.9}S_4$	a = 7.2028(3) Å	$I\bar{4}3m$
$Na_{2.4}Er_{0.4}Zr_{0.6}Cl_6$	a = 6.782(9) Å b = 7.19(2) Å c = 10.036(9) Å β = 91.22(9)	$P2_1/n$
CAM *P*2 $Na_{0.66}Fe_{0.4}Mn_{0.5}Mg_{0.1}O_2$	a = 2.9280(2) Å c = 11.204(3) Å	$P63/mmc$
CAM *O*3 $Na_{0.66}Fe_{0.4}Mn_{0.5}Mg_{0.1}O_2$	a = 2.9497(3) Å c = 16.551(9) Å	$R\bar{3}m$

Supporting measurements

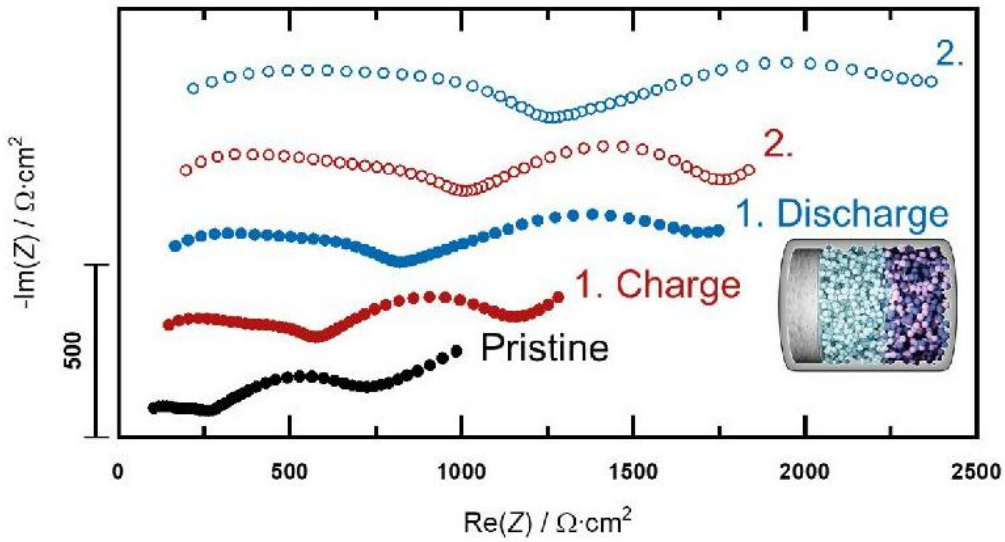

Figure S7: Impedance spectra of the cell Na-Sn|Na_3SbS_4|NEZC:NFMM:C65, as shown in the scheme, in the pristine state (black), after the first charge (red), the first discharge (blue), the second charge step (open red) and the second discharge step (open blue). For better visibility, the impedance spectra are stacked by 200 Ω·cm² on the y-axis. A scale bar of 500 Ω·cm² is added.

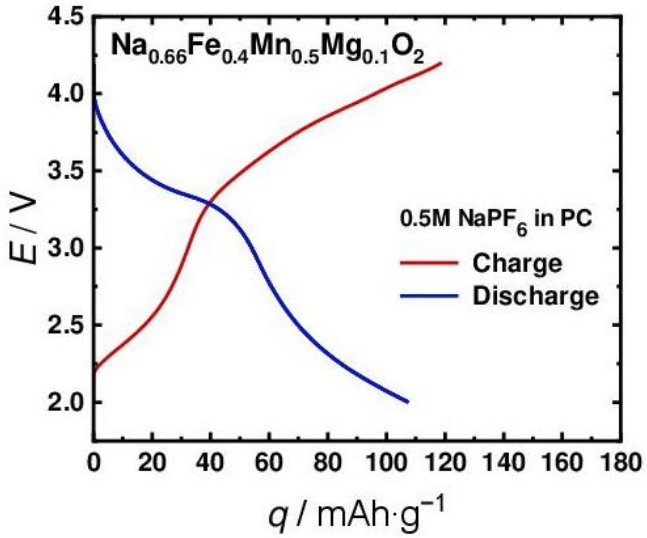

Figure S8: NFMM cycled in a coin cell setup with liquid electrolyte and sodium as anode material at 0.1C with cut-off voltages of 4.25 V and 2 V. The liquid electrolyte was 0.5M $NaPF_6$ (Alfa Aessar) in polycarbonate (PC) purchased from Sigma Aldrich. The glass fibre separator manufacturer was Whatman®.

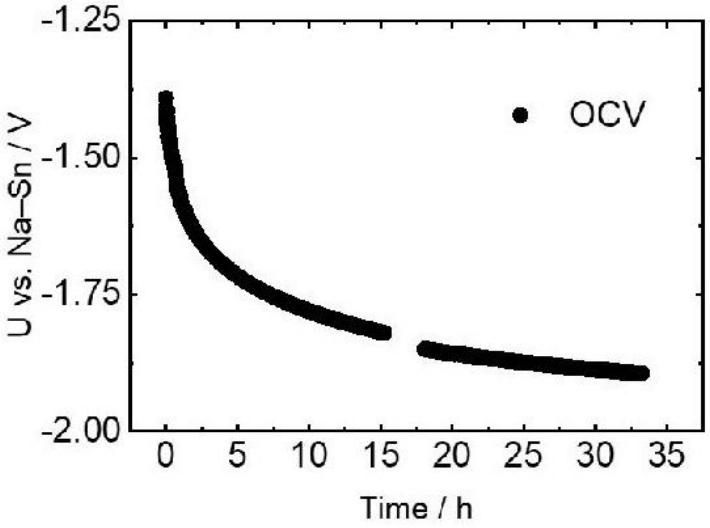

Figure S9: Voltage profile of the pseudo Sn reference electrode measured in a Na-Sn|Na_3SbS_4|RE(Sn)|Na_3SbS_4|Na-Sn symmetric cell reaching a stable potential for the impedance measurements.

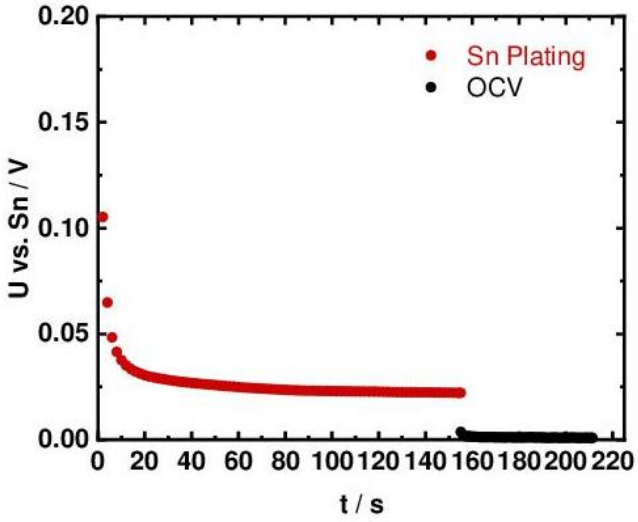

Figure S10: Voltage profile during electrochemical deposition of Sn on the reference gold wire (red) and a subsequent OCV step (black).

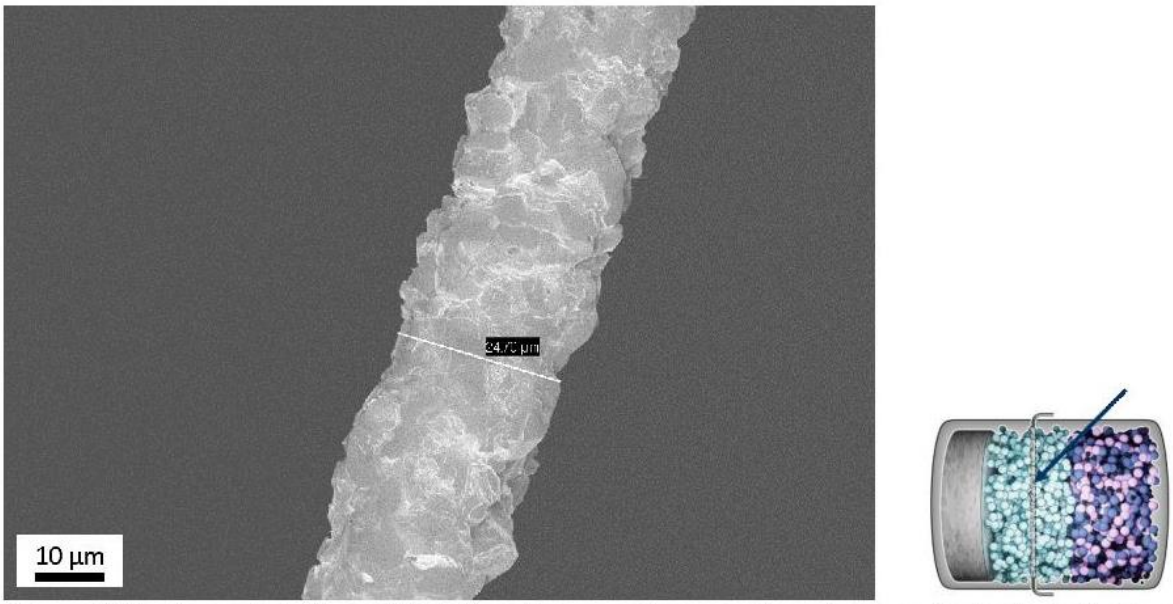

Figure S11: Sn-coated 10 µm thick Au wire as used as pseudo reference electrode in the three-electrode cell.

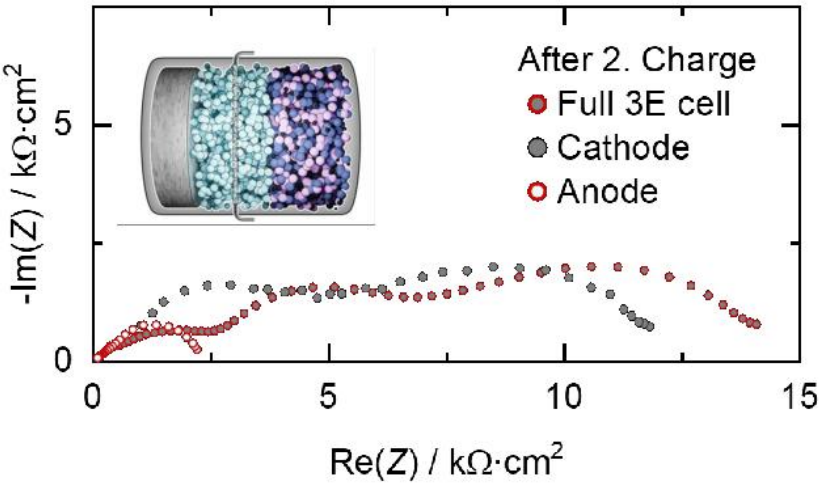

Figure S12: Impedance spectra measured after the second charge of the three-electrode cell. The sum of the contributions of the anode (red circles) and of the cathode (grey dots) equal the full three-electrode cell (grey dot framed red) impedance.

Na_3SbS_4:

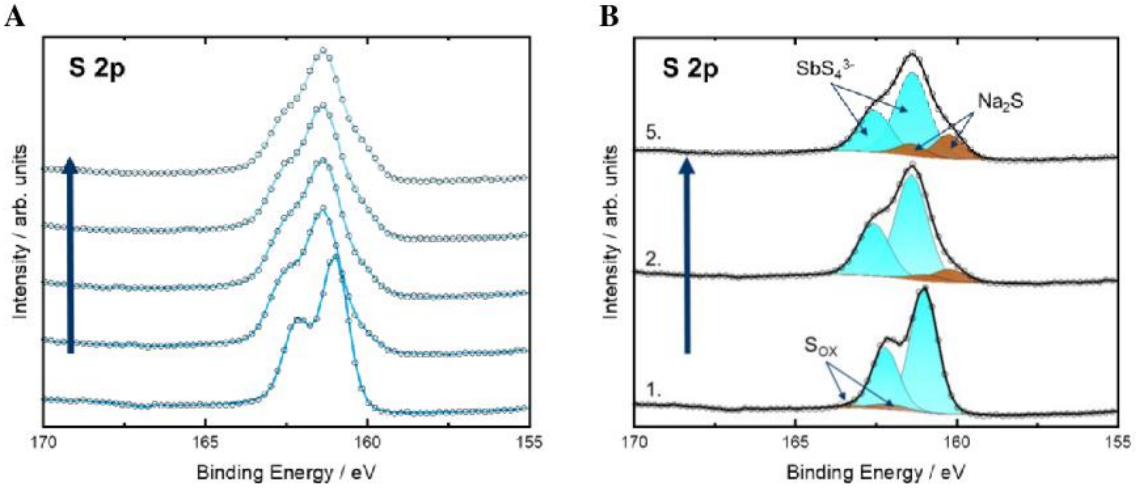

Figure S13: XP spectra of Na_3SbS_4 with (A) the S 2p signal evolving during sputtering, and (B) the fitted S 2p signals of the first (1.), second (2.) and last (5.) spectrum.

XPS of Na_3SbS_4 revealed a sputter damage occurring with increasing sputter steps forming Na_2S. An initial minor signal of oxidized species can be detected in the pristine SE.

Na-Sn:

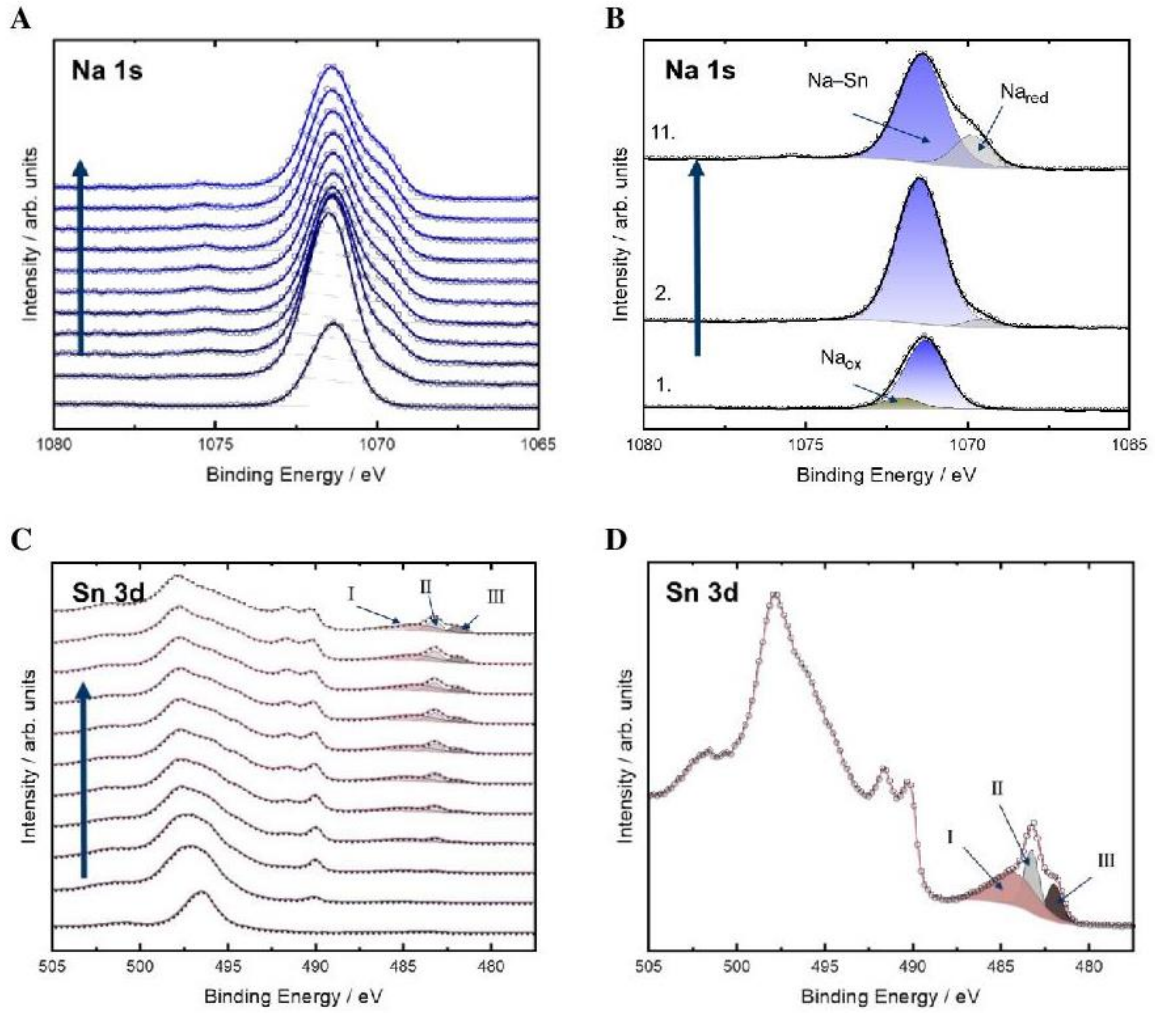

Figure S14: XP spectra of Na-Sn with (A) the Na 1s signal evolution during sputtering and (B) the first, second and last (11.) spectrum of Na 1s after peak fitting. The Sn 3d XP spectra (C) evolution during sputtering of Na-Sn with fitted data (I-III) for the Sn $3d_{5/2}$ peak. (D) The last spectrum after sputtering of the Sn 3d peak with the fitted Sn $3d_{5/2}$ peaks.

XPS of Na-Sn was measured as reference and to compare it with the spectra of the mixture of Na_3SbS_4 and Na-Sn. Since the Sn $3d_{3/2}$ peak overlaps strongly with the Na KLL Auger lines, only the Sn $3d_{5/2}$ peaks were fitted. A quantification to confirm the stoichiometry of the Na-Sn alloy was not possible due to the strong background caused by the Na KLL Auger lines. Unexpectedly the surface spectrum did not show any tin signal. The study on the Na signal showed a second peak indicating a sodium oxide species on the surface. A reduced sodium species is detected with increasing sputtering time. This could indicate the existence of either sodium metal as part of a two-phase alloy or as unreacted starting material from the synthesis of the Na-Sn alloy. Furthermore, it could be a different chemical environment of sodium in the alloy. The three different Sn $3d_{5/2}$ peaks increasing during sputtering indicate different oxidation states of the tin, which is expected in a two-phase alloy.

Mortared Na_3SbS_4 with Na-Sn:

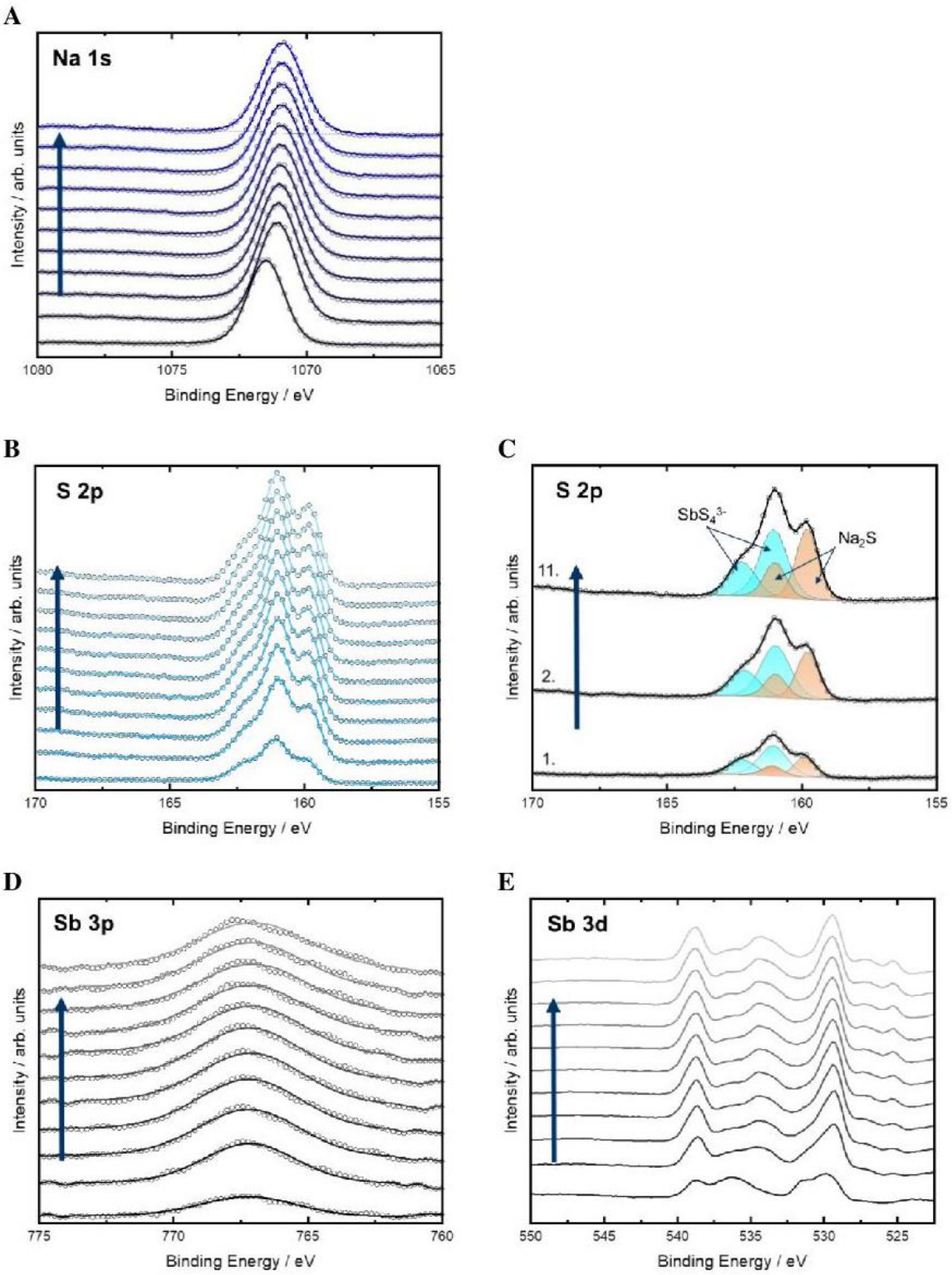

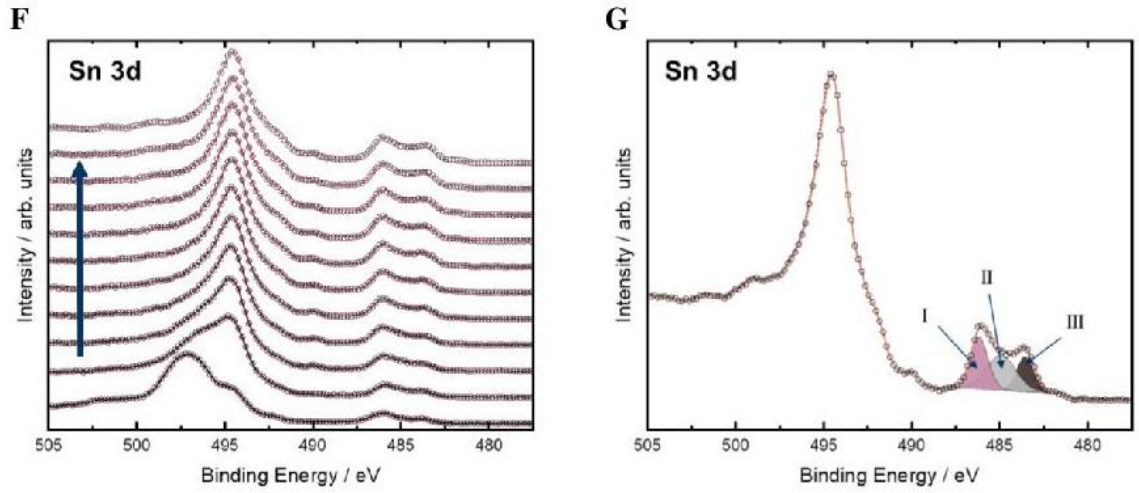

Figure S15: XP spectra after mixing Na_3SbS_4 and Na-Sn of (A) the Na 1s signal and (B) the S 2p signal evolving during sputtering, the first (1.), second (2.) and last (11.) spectrum (C) of the fitted S 2p signal. The Sb 3p (D) and the Sb 3d (E) (overlapping with the oxygen signal) and the Sn 3d (F) (including the 3 d5/2 signal, with overlapping $3d_{3/2}$ signals and Na KLL Auger lines) each evolving during sputtering. (G) Last (11^{th}) spectrum of the Sn 3d peak with fitted Sn $3d_{5/2}$ peaks.

XPS of the mixture of Na_3SbS_4 with Na-Sn shows the claimed chemical decomposition. The sodium signal showing only one Na^+ peak is attributed to both materials and does not change during sputtering. Na_3SbS_4 experiences sputter damage as already shown in the sulfur signal for the pristine electrolyte. The sulfur signal for the mixed materials, however, shows a strong second doublet peak at lower binding energies already in the surface spectrum prior to sputtering. This indicates the formation of Na_2S when Na_3SbS_4 is in contact with Na-Sn. The Sb 3p and 3d signals show no clear signs of change. Especially the Sb 3d peak, which overlaps with the oxygen signal, cannot be properly deconvoluted. An oxygen-rich first surface layer can be assumed. The interpretation of the tin signal faces the same issues as for the pristine Na-Sn due to the overlapping Na KLL lines. The area ratio between the three detected Sn $3d_{5/2}$ peaks, however, differs from the pristine Na-Sn indicating that a reaction between the Na_3SbS_4 and the Na-Sn alloy took place, forming differently oxidized/reduced Sn ratios.

NZSPO:

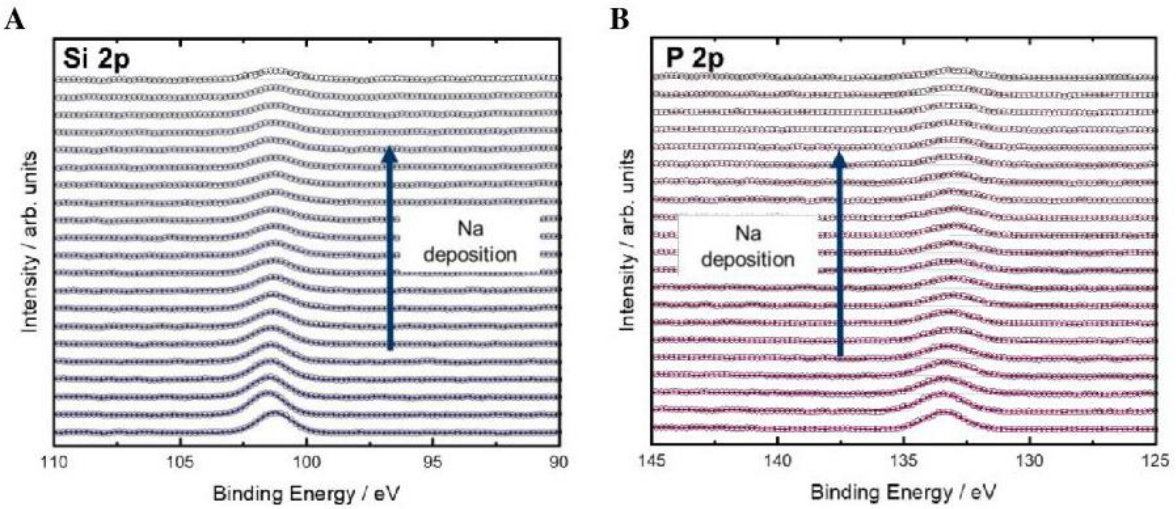

Figure S16: XP spectra of (A) the Si 2p and (B) the P 2p signals evolving during sodium deposition on the NZSPO interlayer material.

Impedance spectra and resistance contributions for symmetric cells

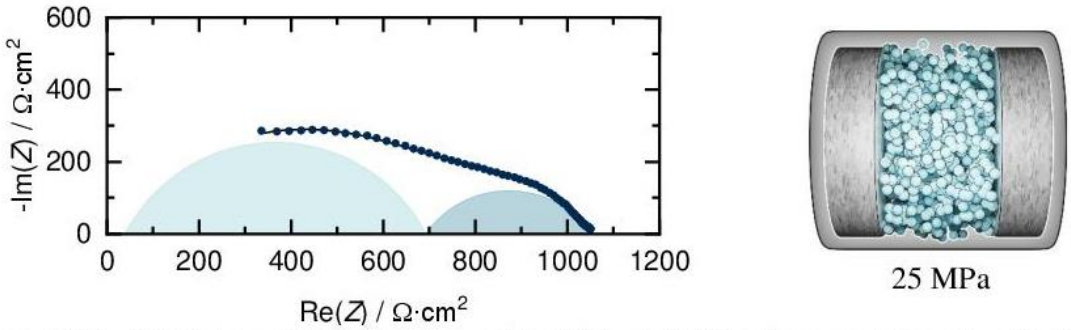

Figure S17: Fitted impedance spectrum after 55 h at OCV of symmetric cell with the SE Na_3SbS_4 and the Na-Sn anode on both sides at a constant pressure of 25 MPa showing the two CPE contributions.

Table S3: List of equivalent circuit parameters for the resistance contributions of the symmetric cell Na-Sn|Na_3SbS_4|Na-Sn with a constant pressure of 25 MPa. The value for R_{SE} was constrained to 39 Ω·cm² since it was evaluated to be 39 Ω·cm² from the impedance measurement for the same cell at higher pressure as can be seen in Figure S18 with the corresponding parameters in Table S4.

No	R_{SE} Ω·cm²	$R_{Na\text{-}Sn/SEI}$ Ω·cm²	$CPE_{Na\text{-}Sn/SEI}$ /10⁻⁹ F	$\alpha_{Na\text{-}Sn/SEI}$	$R_{SEI/SE}$ Ω·cm²	$CPE_{SEI/SE}$ /10⁻⁶ F	$\alpha_{SEI/SE}$
1	39	286	52	0.63	31	292	0.41
2	39	348	7.27	0.74	121	4.54	0.55
3	39	410	9.57	0.72	149	2.58	0.58
4	39	465	12.1	0.71	182	1.84	0.60
5	39	505	13.0	0.70	224	1.47	0.60
6	39	536	13.7	0.70	262	1.29	0.60
7	39	564	13.1	0.70	287	1.19	0.60
8	39	590	13.0	0.70	316	1.09	0.60
9	39	629	13.4	0.69	332	0.97	0.61
10	39	653	12.6	0.70	361	0.92	0.61

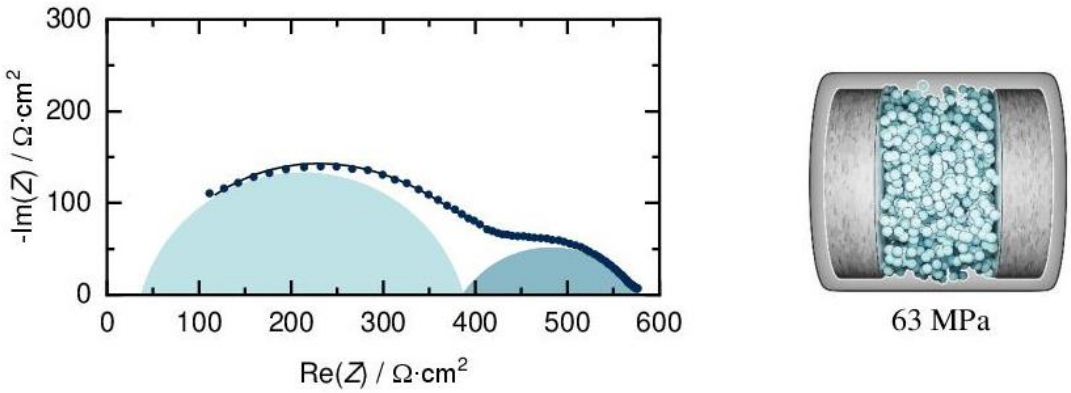

Figure S18: Fitted impedance spectrum after 55 h at OCV of symmetric cell with the SE Na_3SbS_4 and the Na-Sn anode on both sides with a constant pressure of 63 MPa showing the two CPE contributions.

Table S4: List of equivalent circuit parameters for the resistance contributions of the symmetric cell Na-Sn|Na_3SbS_4|Na-Sn with a constant pressure of 63 MPa.

No	R_{SE} $\Omega \cdot cm^2$	$R_{Na\text{-}Sn/SEI}$ $\Omega \cdot cm^2$	$CPE_{Na\text{-}Sn/SEI}$ $/10^{-9}$ F	$\alpha_{Na\text{-}Sn/SEI}$	$R_{SEI/SE}$ $\Omega \cdot cm^2$	$CPE_{SEI/SE}$ $/10^{-6}$ F	$\alpha_{SEI/SE}$
1	52	81	1.67	0.91	56	8.85	0.52
2	51	145	2.56	0.86	86	6.21	0.56
3	43	184	2.45	085	105	4.44	0.58
4	41	218	2.70	0.84	118	3.48	0.60
5	41	241	2.56	0.84	133	3.08	0.60
6	40	267	2.58	0.84	146	2.67	0.61
7	39	292	2.57	0.83	160	2.43	0.61
8	39	313	2.50	0.83	173	2.25	0.61
9	39	325	2.35	0.83	182	2.08	0.62
10	37	349	2.45	0.83	191	1.91	0.62

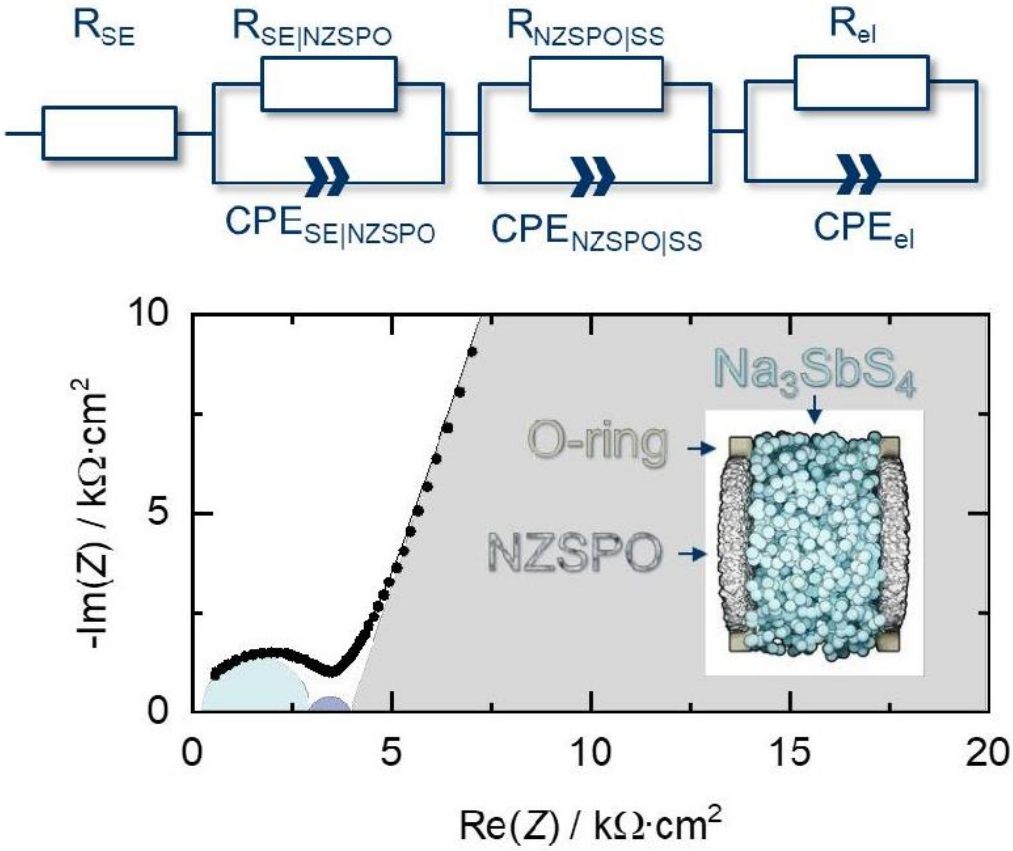

Figure S19: Symmetric cell NZSPO|Na_3SbS_4|NZSPO showing the interfacial resistance between sulfide electrolyte and oxide electrolyte constricted at a constant pressure of 25 MPa. The contributions are from the solid electrolyte resistance R_{SE}, the SE|NZSPO resistance (light blue), the resistance from NZSPO to the stainless-steel rods (SS) (purple) as current collectors and the electronic resistance (grey) due to the ion blocking electrodes.

Table S5: List of equivalent circuit parameters for the resistance contributions of the symmetric cell NZSPO|Na_3SbS_4|NZSPO.

R_{SE} $\Omega \cdot cm^2$	$R_{SE/NZSPO}$ $\Omega \cdot cm^2$	$CPE_{SE/NZSPO}$ $/10^{-11}$ F	$\alpha_{SE/NZSPO}$	$R_{NZSPO/SS}$ $\Omega \cdot cm^2$	$CPE_{NZSPO/SS}$ $/10^{-8}$ F	$\alpha_{NZSPO/SS}$	R_{el} $\Omega \cdot 10^9 \cdot cm^2$	CPE_{el} $/10^{-8}$ F	α_{el}
234	3027	3.2	0.97	1266	7.0	0.65	1.1	1.56	0.82

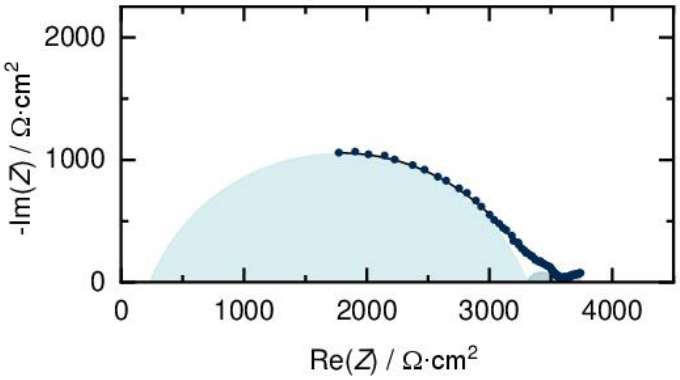

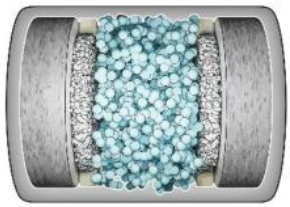

Figure S20: Fitted impedance spectrum after 55 h at OCV of symmetric cell with the SE Na_3SbS_4, two NZSPO disks and the Na-Sn anode on both sides at a constant pressure of 25 MPa showing two *CPE* contributions and a diffusion tail which was fitted with a conductor.

Table S6: List of equivalent circuit parameters for the resistance contributions of the symmetric cell Na-Sn|NZSPO|Na_3SbS_4|NZSPO|Na-Sn. With R_{SE} fixed to 235 $\Omega \cdot cm^2$ derived from the measurement without the Na-Sn anode (Figure S19, Table S5). The $R_{SE/NZSPO}$ for spectra 1 and 2 were fixed as well.

No	R_{SE} $\Omega \cdot cm^2$	$R_{SE/NZSPO}$ $\Omega \cdot cm^2$	$CPE_{SE/NZSPO}$ $/10^{-9}$ F	$\alpha_{SE/NZSPO}$	$R_{NZSPO/Na-Sn}$ $\Omega \cdot cm^2$	$CPE_{NZSPO/Na-Sn}$ $/10^{-7}$ F	$\alpha_{NZSPO/Na-Sn}$	CPE_{Diff} $/10^{-3}$ F	α_{Diff}
1	235	3297	1.09	0.76	422	1.14	0.69	3.80	0.33
2	235	3297	1.11	0.76	245	2.24	0.73	3.45	0.33
3	235	3257	1.25	0.76	164	1.28	0.86	3.23	0.27
4	235	3206	1.22	0.76	177	1.97	0.83	2.90	0.25
5	235	3175	1.21	0.76	182	1.72	0.85	2.62	0.24
6	235	3127	1.24	0.76	194	3.16	0.80	2.45	0.25
7	235	3126	1.19	0.76	209	3.40	0.80	2.36	0.25
8	235	3102	1.12	0.76	224	3.80	0.79	2.29	0.25
9	235	3087	1.09	0.77	228	3.47	0.79	2.27	0.25
10	235	3073	1.14	0.76	229	3.87	0.78	2.23	0.24

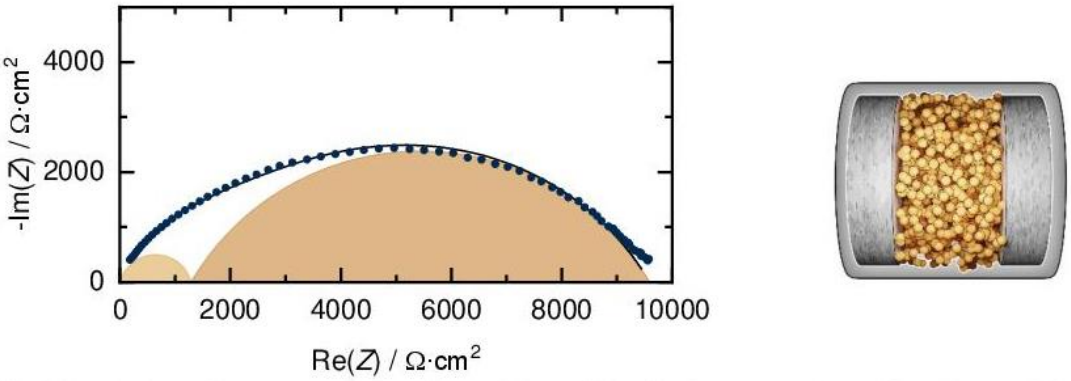

Figure S21: Fitted impedance spectrum after 55 h at OCV of symmetric cell with the SE $Na_{2.9}Sb_{0.9}W_{0.1}S_4$ and the Na-Sn anode on both sides at a constant pressure of 25 MPa showing the two *CPE* contributions.

Table S7: List of equivalent circuit parameters for the resistance contributions of the symmetric cell Na-Sn|$Na_{2.9}Sb_{0.9}W_{0.1}S_4$|Na-Sn.

No	*R* Na-Sn/SEI Ω·cm²	*CPE* Na-Sn/SEI /10⁻⁹ *F*	*α* Na-Sn/SEI	*R* SEI/SE-W Ω·cm²	*CPE* SEI/SE-W /10⁻⁸ *F*	*α* SEI/SE-W
1	50	3.43	1.00	1365	8.18	0.68
2	195	0.98	1.00	3545	4.80	0.67
3	439	3.21	0.89	4556	3.71	0.69
4	602	3.35	0.87	5285	4.09	0.68
5	769	3.54	0.86	5877	4,40	0.68
6	896	3.56	0.85	6433	4.48	0.67
7	1014	3.56	0.85	6938	4.50	0.67
8	1108	3.41	0.84	7415	4.45	0.67
9	1227	3.48	0.84	7836	4.44	0.67
10	1288	3.35	0.84	8306	4.40	0.66

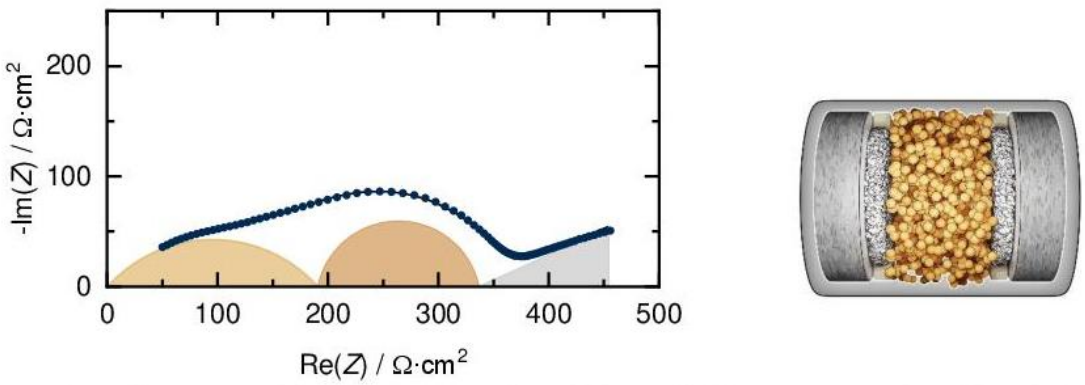

Figure S22: Fitted impedance spectrum after 55 h at OCV of symmetric cell with the SE $Na_{2.9}Sb_{0.9}W_{0.1}S_4$, two NZSPO disks and the Na-Sn anode on both sides at a constant pressure

of 25 MPa showing two CPE contributions and a diffusion tail which was fitted with a conductor.

Table S8: List of equivalent circuit parameters for the resistance contributions of the symmetric cell Na-Sn|NZSPO|$Na_{2.9}Sb_{0.9}W_{0.1}S_4$|NZSPO|Na-Sn.

No	*R* SE-W/NZSPO $\Omega \cdot cm^2$	*CPE* SE-W/NZSPO $/10^{-6}$ *F*	*α* SE-W/NZSPO	*R* NZSPO/Na-Sn $\Omega \cdot cm^2$	*CPE* NZSPO/Na-Sn $/10^{-7}$ *F*	*α* NZSPO/Na-Sn	*CPE* Diff $/10^{-7}$ *F*	*α* Diff
1	178	0.53	0.59	129	1.42	0.84	3.17	0.25
2	179	0.65	0.58	138	1.53	0.85	2.14	0.33
3	184	0.84	0.56	150	2.14	0.84	1.64	0.37
4	186	0.99	0.55	155	2.49	0.83	1.46	0.38
5	188	1.13	0.54	157	2.73	0.83	1.33	0.39
6	191	1.30	0.54	154	2.78	0.84	1.31	0.39
7	193	1.43	0.53	155	2.85	0.84	1.27	0.39
8	196	1.54	0.53	154	2.77	0.84	1.30	0.38
9	199	1.64	0.52	155	2.77	0.85	1.28	0.38

Testing of NZSPO interlayer

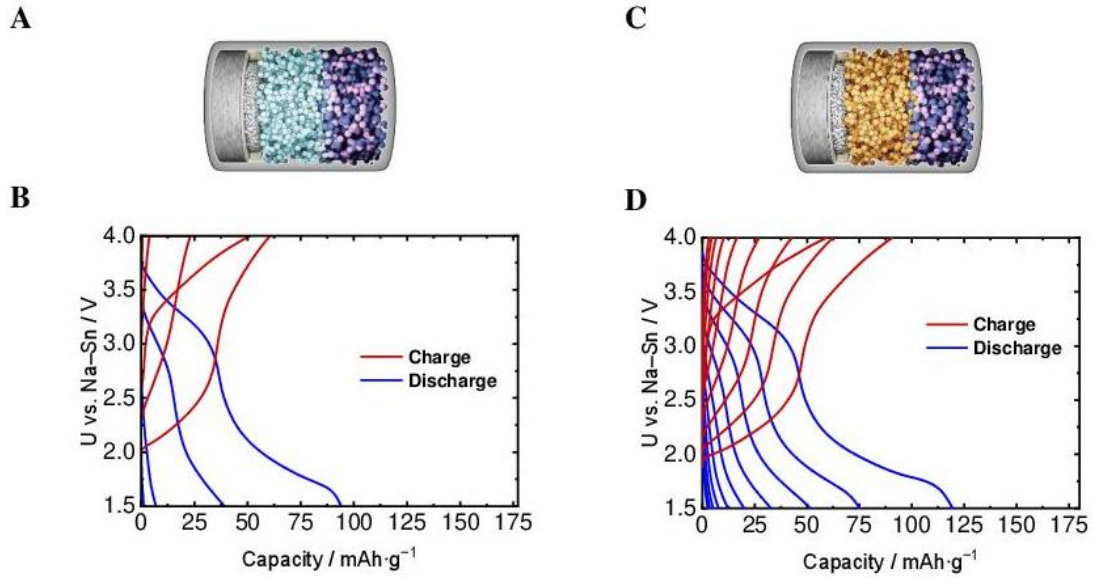

Figure S23: (A) Scheme of the Na-Sn|NZSPO|Na_3SbS_4|NEZC:NFMM:C65 cell with (B) corresponding charge and discharge curves and (C) scheme of the Na-Sn|NZSPO|$Na_{2.9}Sb_{0.9}W_{0.1}S_4$|NEZC:NFMM:C65 cell with (D) corresponding charge and discharge curves each cycled with a current of 24 $\mu A \cdot cm^{-2}$.

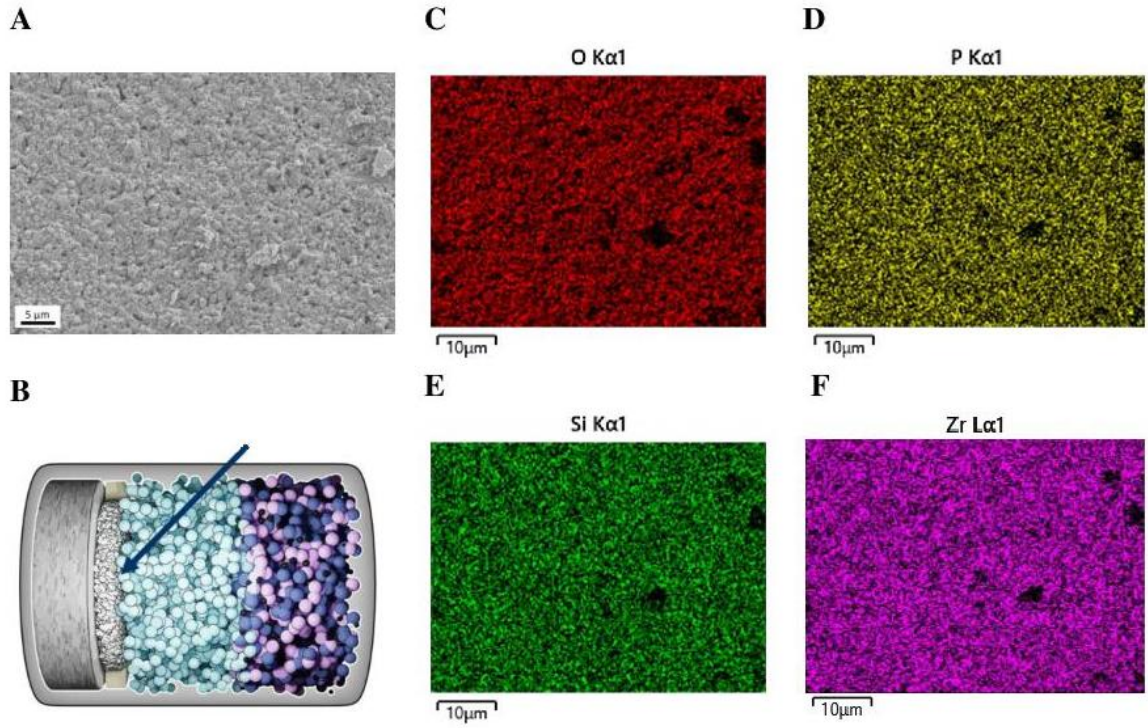

Figure S24: SEM image (A) and EDX element mappings (C-F) of a NZSPO disk taken from a full cell after stripping/plating. The NZSPO disk was in contact with Na_3SbS_4 as shown in the schematic (B). EDX mappings recorded at 8 kV and 2000 pA for the elements oxygen (C), phosphorus (D), silicon (E) and zirconium (F).

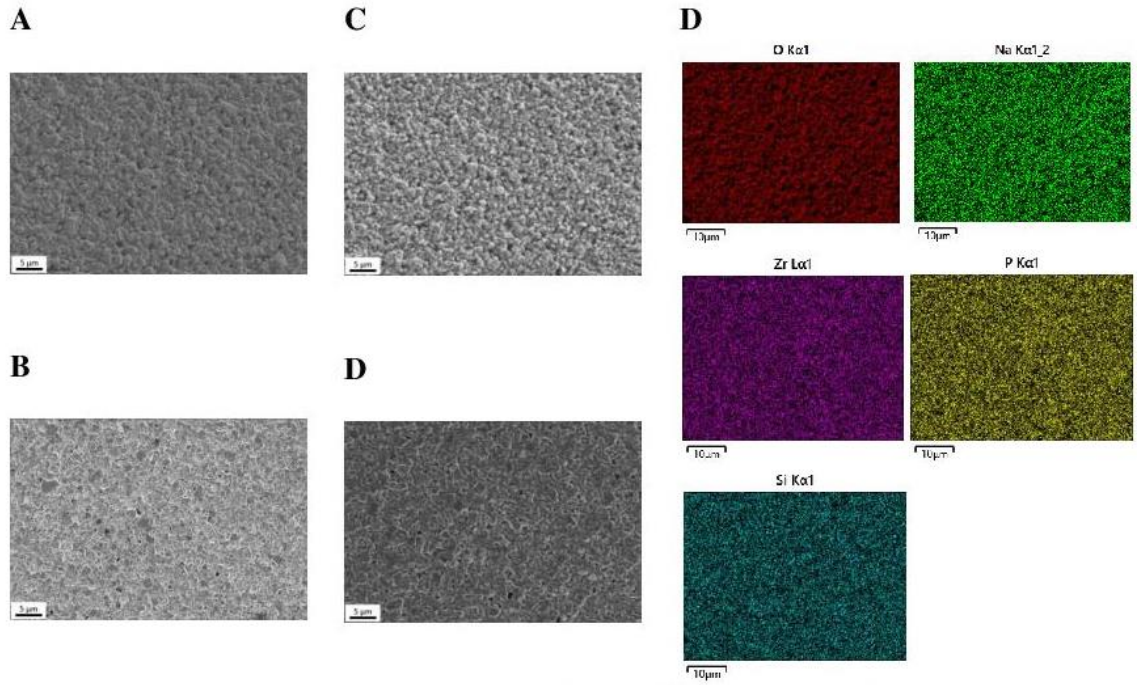

Figure S25: SEM images (A-D) of NZSPO disk at different acceleration voltages/currents and with different detectors. 3 kV and 100 pA (A,B) and 8 kV and 2000 pA (C,D). Images taken with SE2 detector (A,C) and InLens detector (B,D). EDX element mappig (D) of a NZSPO disk at 8 kV and 2000 pA for the elements oxygen, sodium, zirconium, phosphorus and silicon.

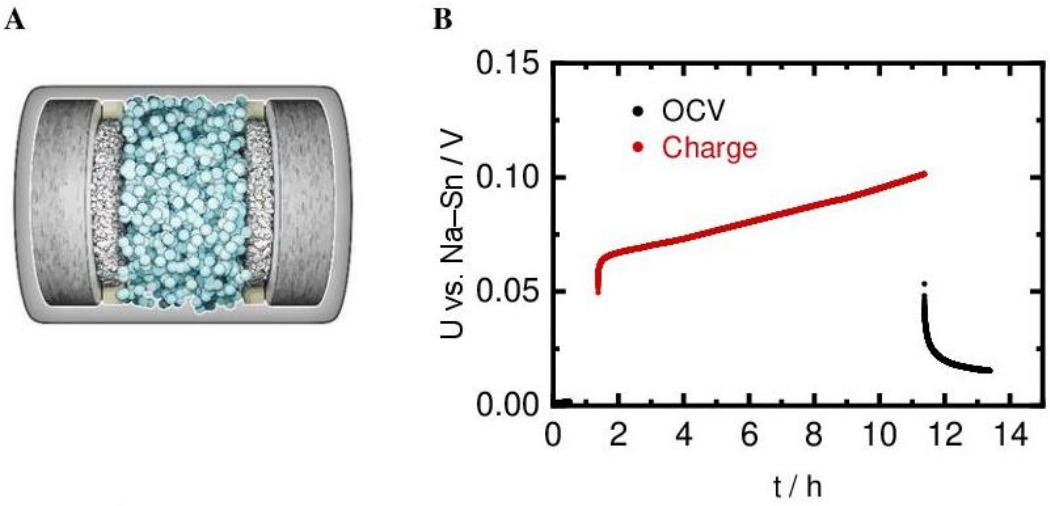

Figure S26: Symmetric cell (A) with Na_3SbS_4 as separator SE, two NZSPO interlayers, and the Na-Sn electrodes during application of a unidirectional current of 24 $\mu A \cdot cm^{-2}$ and the resulting voltage response (B).

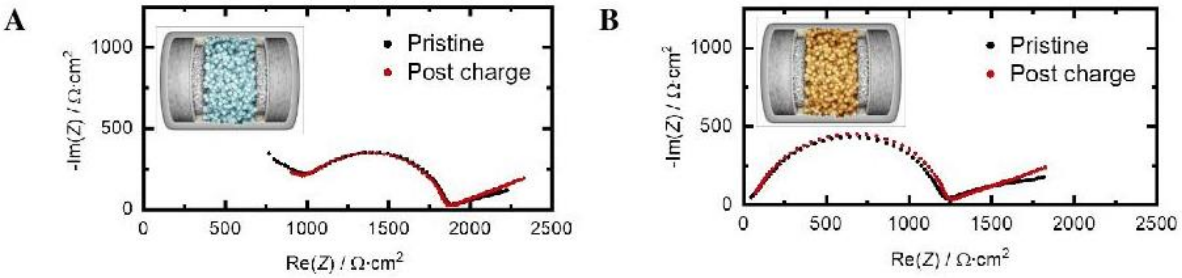

Figure S27: Impedance spectra of symmetric cells with (A) Na_3SbS_4 (blue) and (B) $Na_{2.9}Sb_{0.9}W_{0.1}S_4$ (yellow) as separator, NZSPO (white) as anode protective layer and Na-Sn as anode before (black) and after current flow (red). Please note, that the nominal resistance values differ between the cells. This is due to stack pressure differences caused by the O-ring contributions.

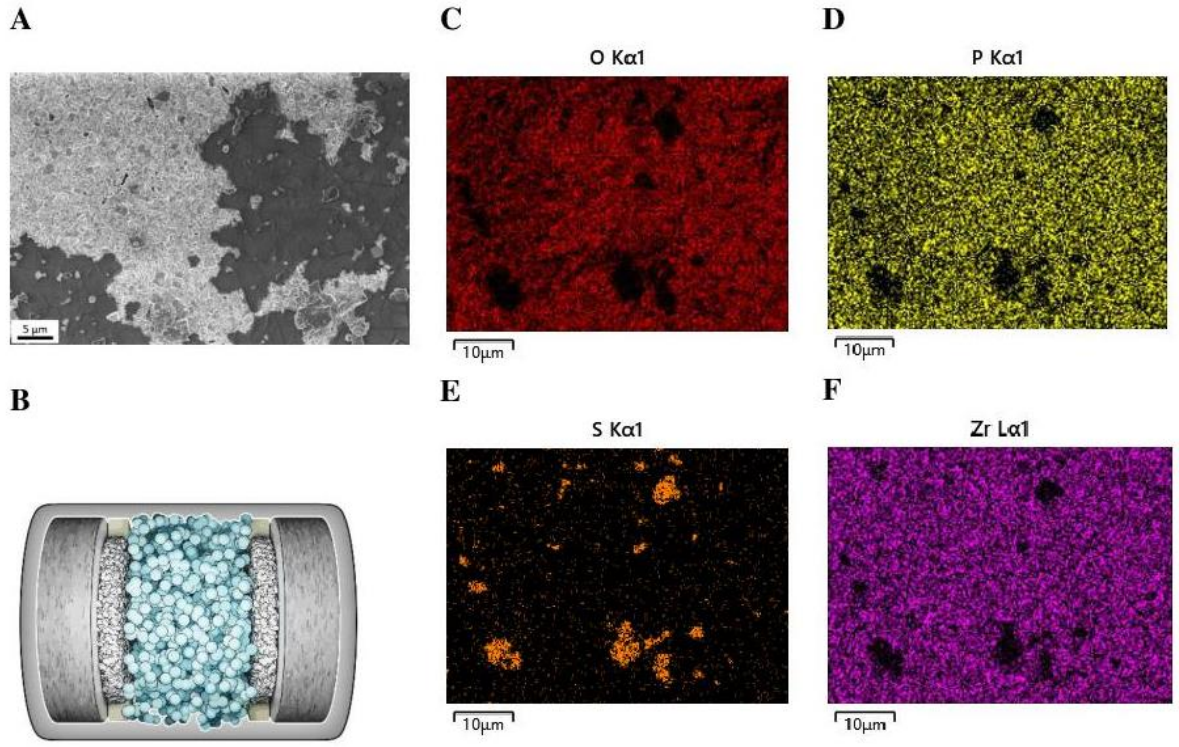

Figure S28: SEM image (A) and EDX element mappings (C-F) of a NZSPO disk taken from a symmetric cell after unidirectional current flow. The NZSPO disk was in contact with Na_3SbS_4 as shown in the schematic (B). EDX mappings recorded at 8 kV and 2000 pA for the elements oxygen (C), phosphorus (D), sulfur (E) and zirconium (F).

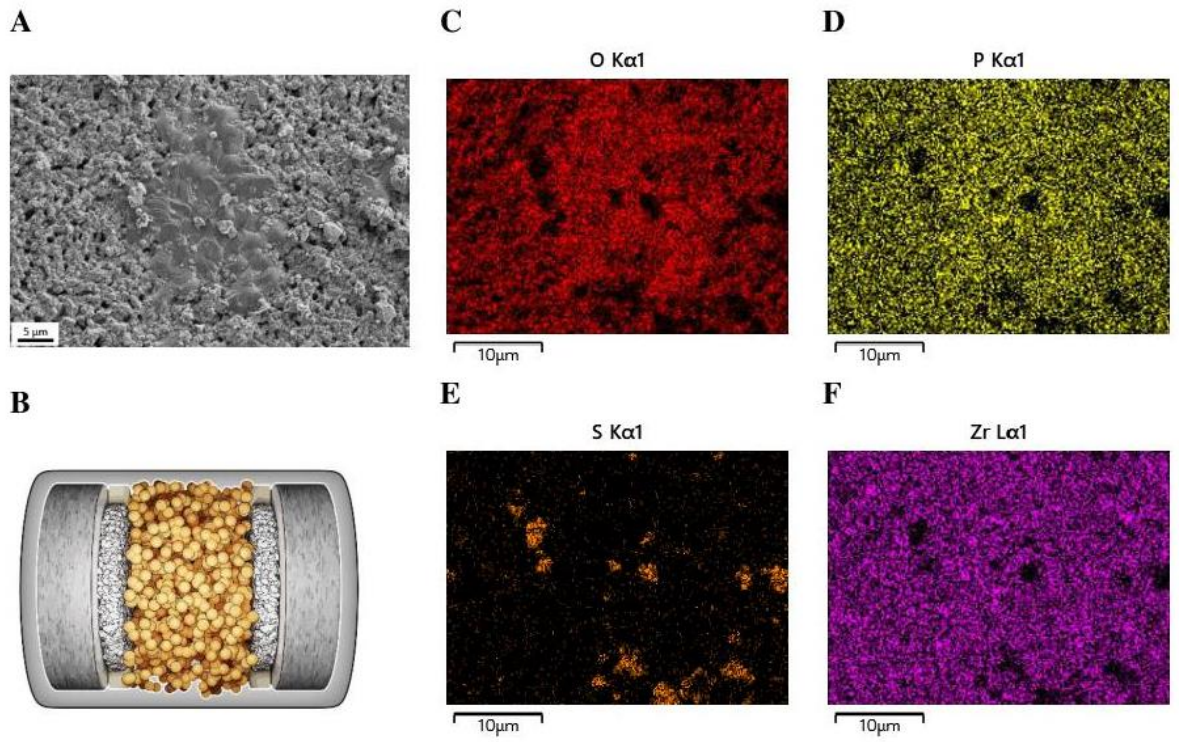

Figure S29: SEM image (A) and EDX element mappings (C-F) of a NZSPO disk taken from a symmetric cell after unidirectional current flow. The NZSPO disk was in contact with $Na_{2.9}Sb_{0.9}W_{0.1}S_4$ as shown in the schematic (B). EDX mappings recorded at 8 kV and 2000 pA for the elements oxygen (C), phosphorus (D), sulfur (E) and zirconium (F).

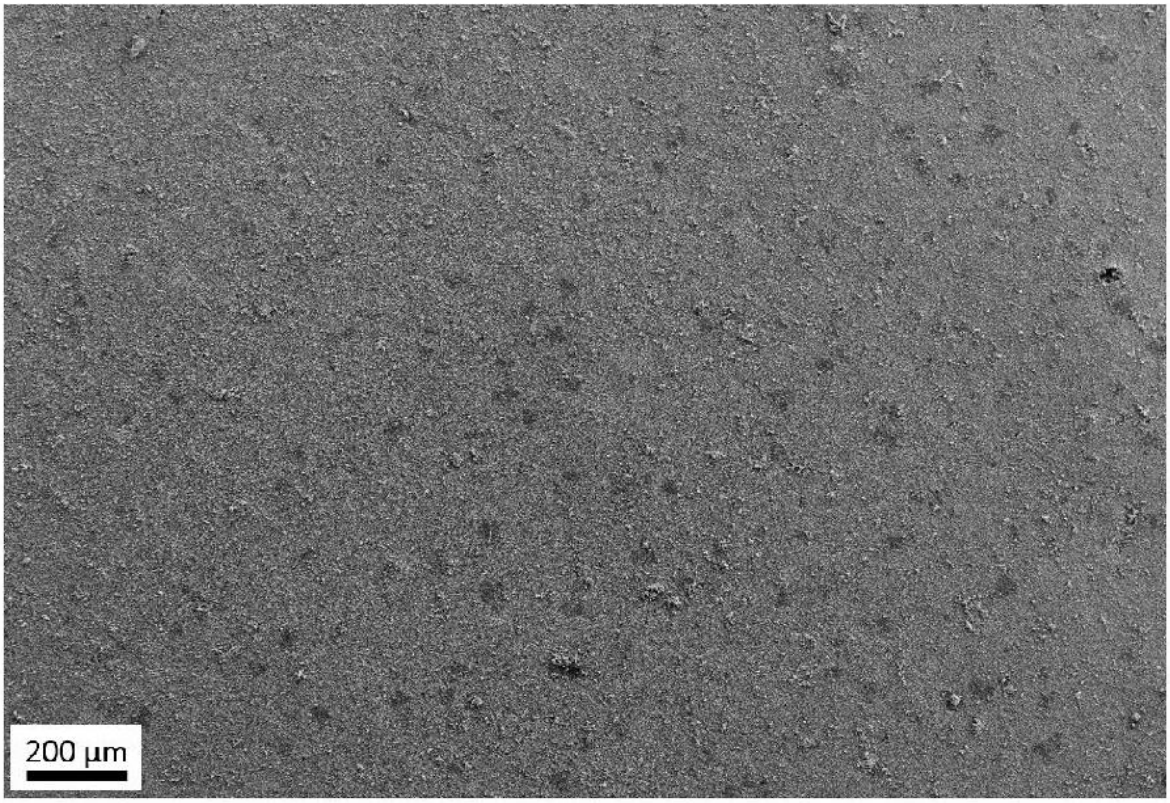

Figure S30: SEM image of a NZSPO taken from a symmetric cell after unidirectional current flow. The NZSPO was in contact with $Na_{2.9}Sb_{0.9}W_{0.1}S_4$. A SE2 detector with an 8 kV acceleration voltage and 2 nA emission current was used.

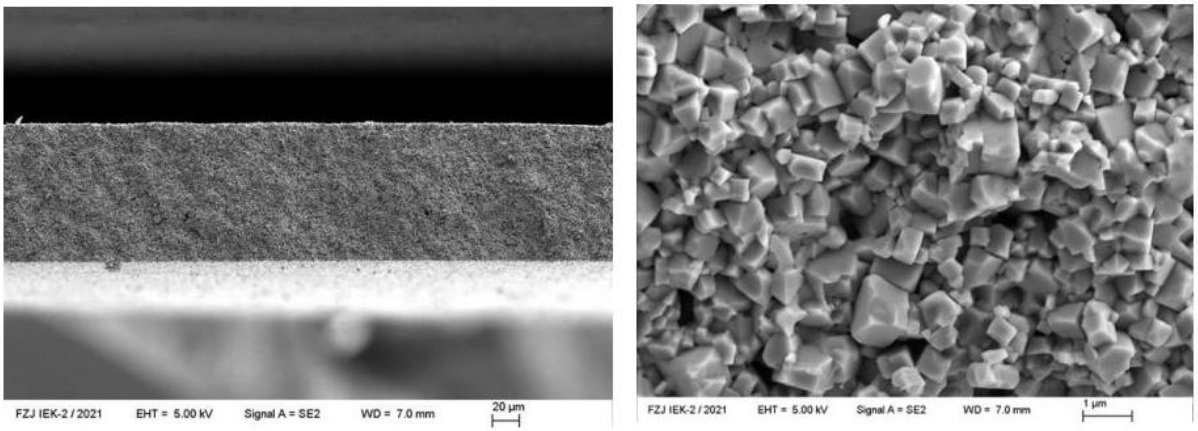

Figure S31: SEM micrographs of a fracture surface of a 95 % dense and 90 µm thick NZSPO disk analyzed using a Zeiss SUPRA 50 VP.

References

(1) Schlem, R.; Banik, A.; Eckardt, M.; Zobel, M.; Zeier, W. G. $Na_{3-x}Er_{1-x}Zr_xCl_6$ — A Halide-Based Fast Sodium-Ion Conductor with Vacancy-Driven Ionic Transport. *ACS Appl. Energy Mater.* **2020**, *3* (10), 10164–10173.

(2) Ma, Q.; Guin, M.; Naqash, S.; Tsai, C.-L.; Tietz, F.; Guillon, O. Scandium-Substituted $Na_3Zr_2(SiO_4)_2(PO_4)$ Prepared by a Solution-Assisted Solid-State Reaction Method as Sodium-Ion Conductors. *Chem. Mater.* **2016**, *28* (13), 4821–4828.

(3) Naqash, S.; Ma, Q.; Tietz, F.; Guillon, O. $Na_3Zr_2(SiO_4)_2(PO_4)$ Prepared by a Solution-Assisted Solid State Reaction. *Solid State Ionics* **2017**, *302*, 83–91.

(4) Till, P.; Agne, M. T.; Kraft, M. A.; Courty, M.; Famprikis, T.; Ghidiu, M.; Krauskopf, T.; Masquelier, C.; Zeier, W. G. Two-Dimensional Substitution Series $Na_3P_{1-x}Sb_xS_{4-y}Se_y$: Beyond Static Description of Structural Bottlenecks for Na + Transport. *Chem. Mater.* **2022**, *34* (5), 2410–2421.

(5) Fuchs, T.; Culver, S. P.; Till, P.; Zeier, W. G. Defect-Mediated Conductivity Enhancements in $Na_{3-x}Pn_{1-x}W_xS_4$ (Pn = P, Sb) Using Aliovalent Substitutions. *ACS Energy Lett.* **2020**, *5* (1), 146–151.

5.2. Supporting Information Publication II

Supporting Information

Halide and Sulfide Electrolytes in Cathode Composites for Sodium All-Solid-State Batteries and their Stability

Laura E. Goodwin[a,b], Maya Ziegler[a,b], Paul Till[c], Nazia Nazer[d], Philipp Adelhelm[d], Wolfgang G. Zeier[c,e], Felix H. Richter[a,b], Jürgen Janek[a,b,]*

[a] Institute for Physical Chemistry, Justus Liebig University Giessen, 35392 Giessen, Germany.

[b] Center for Materials Research (ZfM), Justus Liebig University Giessen, 35392 Giessen, Germany.

[c] Institute for Inorganic and Analytical Chemistry, University of Münster, 48149 Münster, Germany.

[d] Institute of Chemistry, Humboldt University Berlin, 12489 Berlin, Germany.

[e] Institut für Energie-und Klimaforschung (IEK), IEK-12: Helmholtz-Institut Münster, Forschungszentrum Jülich, 48149 Münster, Germany

Corresponding author: juergen.janek@pc.jlug.de

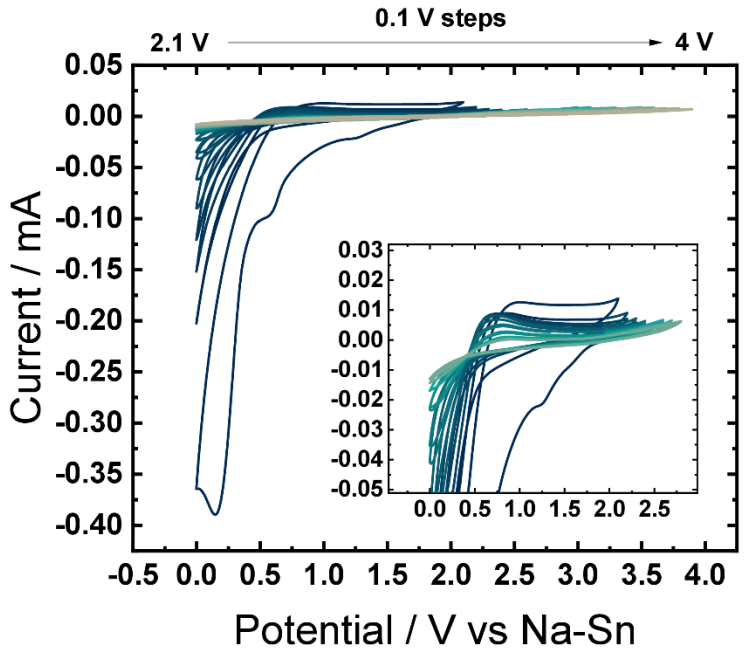

Figure S 1: Stability window test of Na_3SbS_4 using the cell setup Na–Sn|Na_3SbS_4|CAM:Na_3SbS_4:C65. Lower cutoff potential is 0 V vs Na–Sn and the upper cut-off potential was 4 V in increased steps of 0.1 V. Scan speed was 0.1 $mV \cdot s^{-1}$.

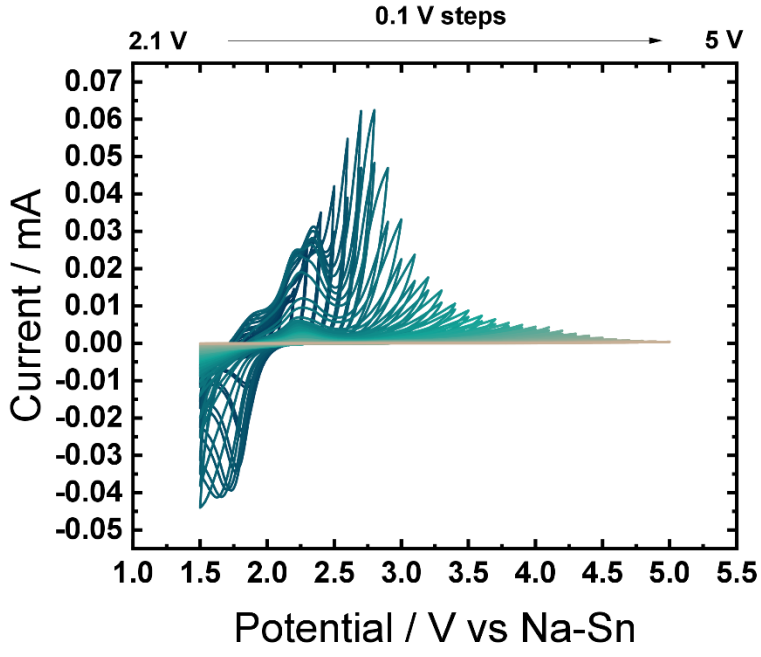

Figure S 2: Stability window test of Na_3SbS_4 using the cell setup Na–Sn|Na_3SbS_4|CAM:Na_3SbS_4:C65. Lower cutoff potential is 1.5 V vs Na–Sn and the upper cutoff potential was 5 V in increased steps of 0.1 V. Scan speed was 0.1 $mV \cdot s^{-1}$.

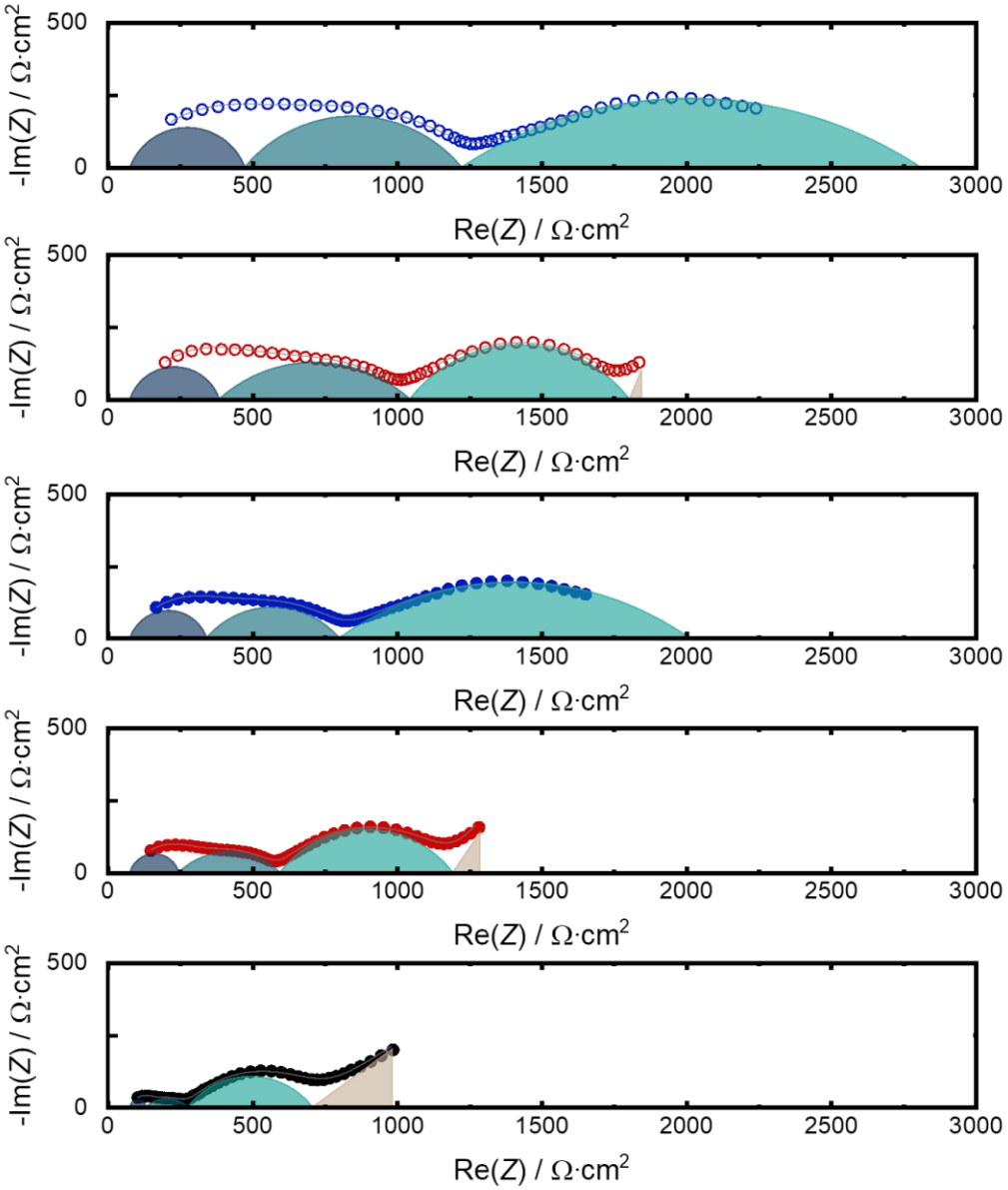

Figure S 3: Fitted impedance spectra with corresponding resistance contributions of a cell type Na–Sn|Na_3SbS_4|NFMM:NEZC:C65 cycled at a C-Rate of 0.01C. The impedance spectra bottom to top show the pristine state (black), the impedance after the first charge (red), the first discharge (blue), the second charge step (open red) and the second discharge step (open blue). Impedances of the pristine cell and those after charge are fitted with a resistor for the bulk impedance which stays constant, three (R)(CPE) elements for the charge transfer resistance and interfacial processes of the anode and cathode and an additional CPE (beige) for diffusion. The impedance spectra after discharge do not show the diffusion tail and are therefore only fitted with the resistor for the bulk impedance and three (R)(CPE) elements.

5. Appendix

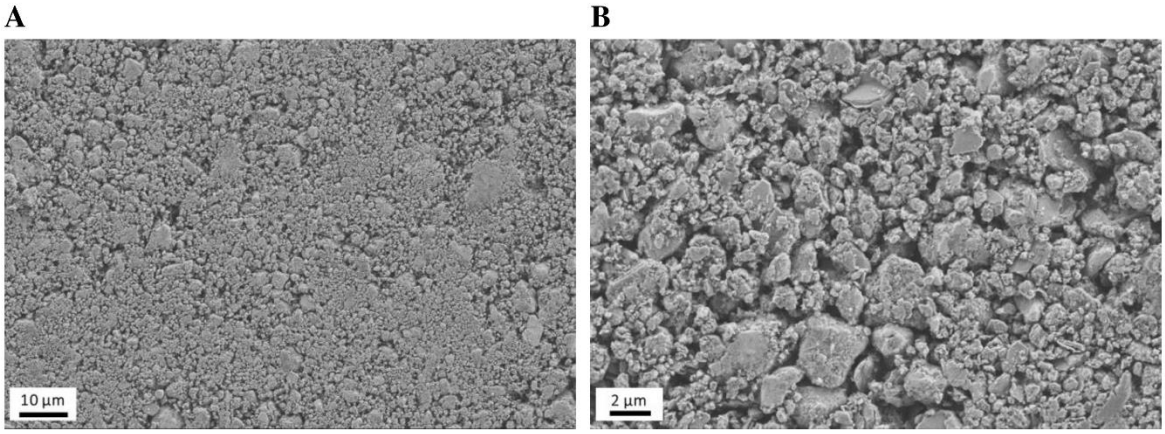

Figure S 4: SEM images of the NFMM:NEZC:C65 composite in (A) ×1000 magnification (scale 10 µm) and (B) ×4000 magnification (scale 2 µm).

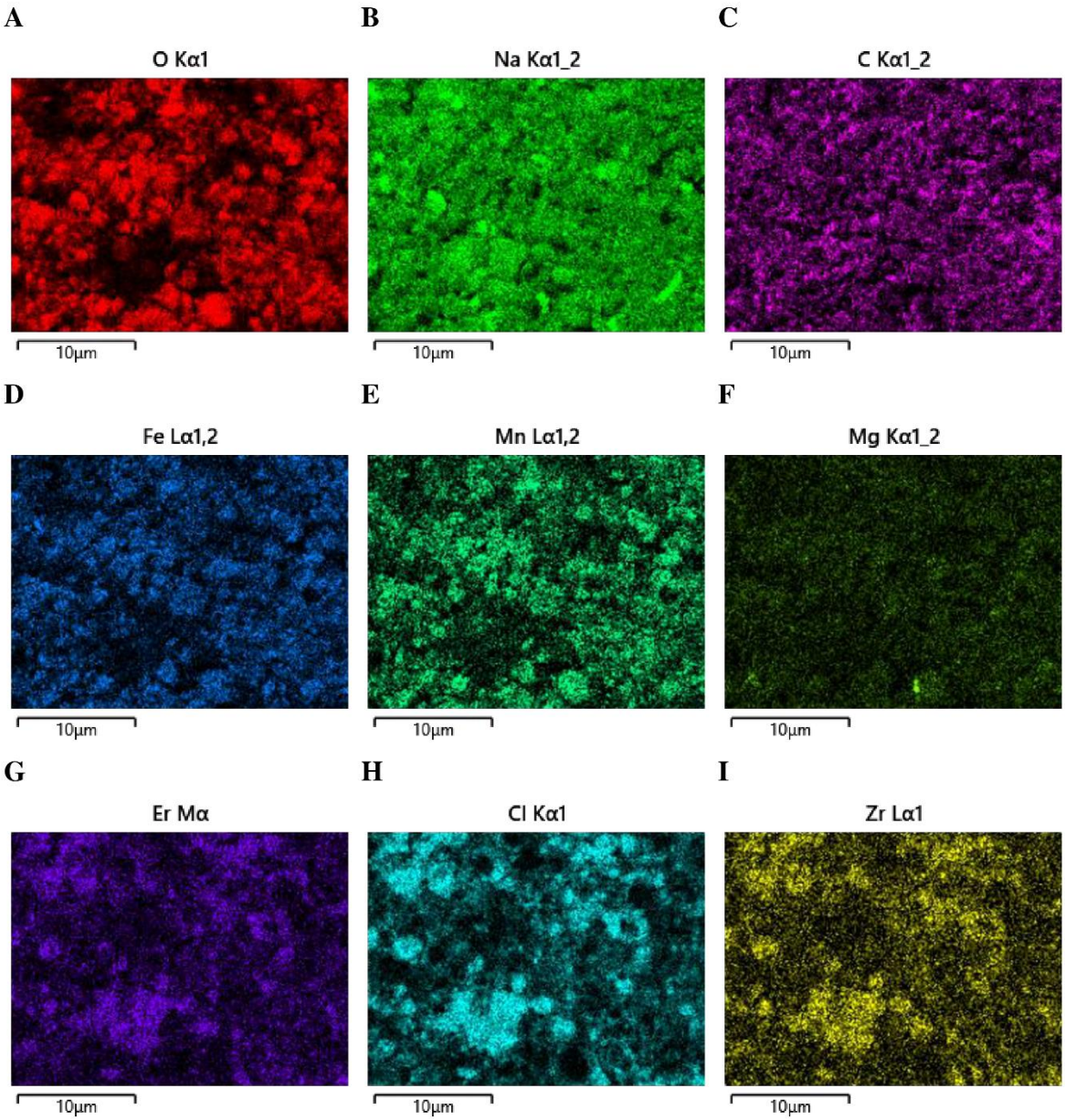

Figure S 5: EDX images of the NFMM:NEZC:C65 composite shown **Figure S 4**. (B) The Na $K_{\alpha1,2}$ line is specific for both CAM and solid electrolyte. The Fe $L_{\alpha1,2}$ (D), Mn $L_{\alpha1,2}$ (E), Mg $K_{\alpha1,2}$ (F) and O $K_{\alpha1}$ (A) are specific for the CAM, Er M_{α} (G), Cl $K_{\alpha1}$ (H) and Zr $L_{\alpha1}$ (I) for the solid electrolyte. The C $K_{\alpha1,2}$ signal (C) shows the carbon additive (C65) distribution in the composite.

For the CAM $Na_{0.66}Fe_{0.4}Mn_{0.5}Mg_{0.1}O_2$ (NFMM) the energies for the elements oxygen (O $K_{\alpha1}$), iron (Fe $L_{\alpha1,2}$), manganese (Mn $L_{\alpha1,2}$) and magnesium (Mg $K_{\alpha1,2}$) are characteristic. For the catholyte $Na_{2.4}Er_{0.4}Zr_{0.6}Cl_6$, (NEZC) the energies of the elements erbium (Er M_{α}), chloride (Cl $K_{\alpha1}$) and zirconium (Zr $L_{\alpha1}$) are specific. The binding energy peak of sodium (Na $K_{\alpha1,2}$) corresponds to both materials and C $K_{\alpha1,2}$ corresponds to the C65 carbon additive.

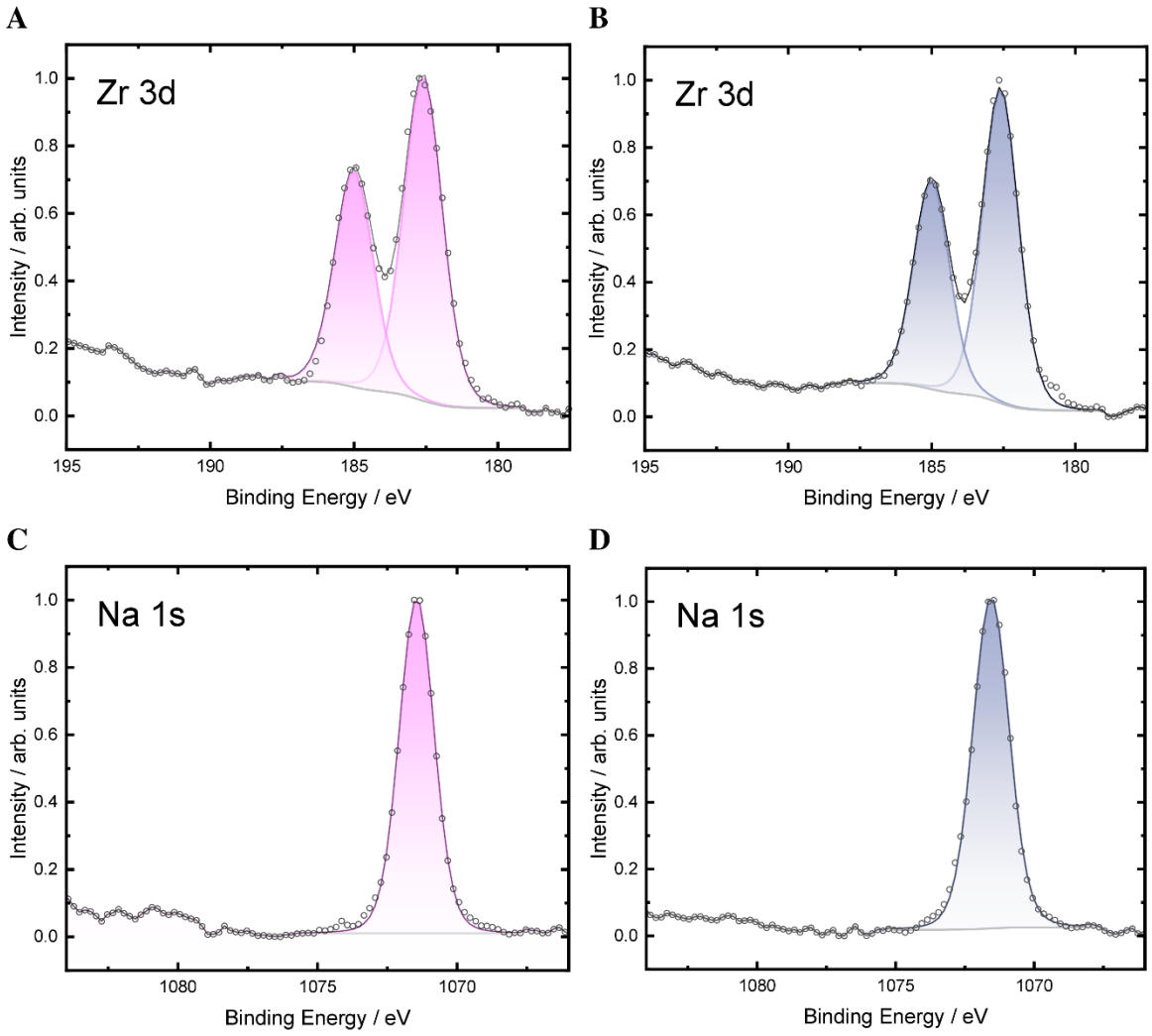

Figure S 6: (A) Zr 3d XP spectra of NEZC and (B) the composite NFMM:NEZC:C65 and (C) the Na 1s XP spectra fitted to the Zr 3d signal of NEZC and (D) the composite NFMM:NEZC:C65.

Table S1: List of equivalent circuit parameters for the resistance contributions of the cell Na_3SbS_4|NEZC measured over 48 h at 25°C.

No	*R* SE $\Omega \cdot cm^2$	*CPE* SE $/10^{-10}$ *F*	*α* SE	*R* NEZC/Na_3SbS_4 $\Omega \cdot cm^2$	*CPE* NEZC/Na_3SbS_4 $/10^{-6}$ *F*	*α* NEZC/Na_3SbS_4	*CPE* Diff $/10^{-6}$ *F*	*α* Diff
1	3404	5.54	0.82	506	0.41	0.82	1.56	0.78
2	3417	5.47	0.82	507	0.39	0.83	1.54	0.78
3	3424	5.56	0.82	509	0.38	0.84	1.52	0.78
4	3424	5.55	0.82	513	0.38	0.84	1.51	0.78
5	3434	5.67	0.82	518	0.40	0.84	1.50	0.78
6	3439	5.58	0.82	525	0.42	0.83	1.49	0.78
7	3445	5.58	0.82	530	0.42	0.83	1.48	0.78
8	3456	5.59	0.82	536	0.43	0.83	1.47	0.78
9	3453	5.59	0.82	540	0.44	0.83	1.46	0.78
10	3439	5.61	0.82	537	0.45	0.83	1.46	0.78
11	3433	5.54	0.82	547	0.45	0.83	1.45	0.78
12	3438	5.66	0.82	549	0.47	0.82	1.45	0.78
13	3440	5.53	0.82	556	0.47	0.82	1.44	0.78
14	3446	5.62	0.82	553	0.45	0.83	1.44	0.78
15	3446	5.63	0.82	566	0.51	0.82	1.43	0.78
16	3447	5.57	0.82	564	0.50	0.82	1.43	0.77
17	3450	5.62	0.82	571	0.51	0.82	1.42	0.77
18	3453	5.63	0.82	575	0.54	0.81	1.42	0.77
19	3457	5.54	0.82	579	0.56	0.81	1.41	0.77
20	3463	5.64	0.82	581	0.55	0.81	1.41	0.77
21	3460	5.61	0.82	589	0.57	0.81	1.40	0.77
22	3466	5.62	0.82	596	0.59	0.80	1.40	0.77
23	3469	5.60	0.82	597	0.59	0.81	1.40	0.77
24	3471	5.69	0.82	601	0.60	0.80	1.39	0.77
25	3479	5.71	0.82	602	0.60	0.81	1.39	0.77
26	3478	5.65	0.82	609	0.61	0.80	1.38	0.77
27	3480	5.59	0.82	612	0.64	0.80	1.38	0.77
28	3480	5.64	0.82	623	0.68	0.79	1.37	0.78
29	3484	5.61	0.82	623	0.68	0.79	1.37	0.77
30	3488	5.69	0.82	628	0.71	0.79	1.37	0.77
31	3487	5.65	0.82	631	0.71	0.79	1.36	0.77
32	3488	5.65	0.82	635	0.72	0.79	1.36	0.78
33	3495	5.68	0.82	641	0.73	0.79	1.35	0.78
34	3493	5.69	0.82	648	0.78	0.78	1.35	0.78
35	3500	5.81	0.82	646	0.75	0.79	1.35	0.78
36	3500	5.69	0.82	652	0.78	0.78	1.34	0.78
37	3500	5.62	0.82	658	0.78	0.78	1.34	0.78
38	3504	5.65	0.82	662	0.82	0.78	1.34	0.78
39	3507	5.70	0.82	666	0.83	0.78	1.33	0.78

40	3509	5.62	0.82	674	0.86	0.77	1.33	0.78
41	3519	5.67	0.82	680	0.89	0.77	1.32	0.78
42	3517	5.69	0.82	680	0.88	0.77	1.32	0.78
43	3515	5.57	0.82	689	0.93	0.77	1.32	0.78
44	3518	5.74	0.82	692	0.92	0.77	1.32	0.78
45	3519	5.73	0.82	697	0.96	0.76	1.31	0.78
46	3520	5.68	0.82	705	1.02	0.76	1.31	0.78
47	3521	5.65	0.82	703	0.98	0.76	1.31	0.78
48	3529	5.79	0.82	705	1.01	0.76	1.31	0.78
49	3524	5.65	0.82	722	1.09	0.75	1.30	0.78
50	3529	5.63	0.82	717	1.04	0.76	1.30	0.78
51	3533	5.78	0.82	721	1.05	0.76	1.30	0.78
52	3531	5.69	0.82	733	1.13	0.75	1.29	0.78
53	3537	5.73	0.82	732	1.12	0.75	1.29	0.78
54	3539	5.64	0.82	741	1.18	0.74	1.29	0.78
55	3541	5.65	0.82	750	1.19	0.74	1.29	0.78
56	3546	5.64	0.82	758	1.24	0.74	1.28	0.78
57	3550	5.71	0.82	755	1.19	0.74	1.28	0.78
58	3553	5.81	0.82	757	1.22	0.74	1.28	0.78
59	3551	5.73	0.82	772	1.28	0.74	1.28	0.78
60	3554	5.61	0.82	777	1.30	0.73	1.27	0.78
61	3554	5.69	0.82	781	1.32	0.73	1.27	0.78
62	3559	5.77	0.82	785	1.34	0.73	1.27	0.78
63	3559	5.73	0.82	789	1.35	0.73	1.27	0.78
64	3566	5.82	0.82	796	1.41	0.73	1.26	0.78
65	3562	5.67	0.82	806	1.46	0.72	1.26	0.78
66	3565	5.67	0.82	808	1.44	0.72	1.26	0.78
67	3569	5.70	0.82	816	1.49	0.72	1.26	0.78
68	3567	5.65	0.82	830	1.57	0.71	1.25	0.78
69	3574	5.81	0.82	829	1.54	0.72	1.25	0.78
70	3575	5.77	0.82	832	1.54	0.72	1.25	0.78
71	3575	5.71	0.82	844	1.65	0.71	1.25	0.78
72	3580	5.67	0.82	838	1.56	0.72	1.25	0.78
73	3579	5.65	0.82	861	1.74	0.70	1.25	0.78
74	3589	5.81	0.82	852	1.67	0.71	1.25	0.78
75	3591	5.75	0.82	864	1.69	0.71	1.24	0.78
76	3592	5.78	0.82	868	1.70	0.71	1.24	0.78
77	3603	5.80	0.82	861	1.63	0.72	1.24	0.78
78	3599	5.75	0.82	880	1.75	0.71	1.24	0.78
79	3602	5.75	0.82	888	1.78	0.71	1.24	0.78
80	3603	5.77	0.82	900	1.88	0.70	1.23	0.78
81	3606	5.85	0.82	893	1.79	0.71	1.24	0.78
82	3605	5.74	0.82	915	1.97	0.69	1.23	0.78
83	3608	5.76	0.82	914	1.93	0.70	1.23	0.78

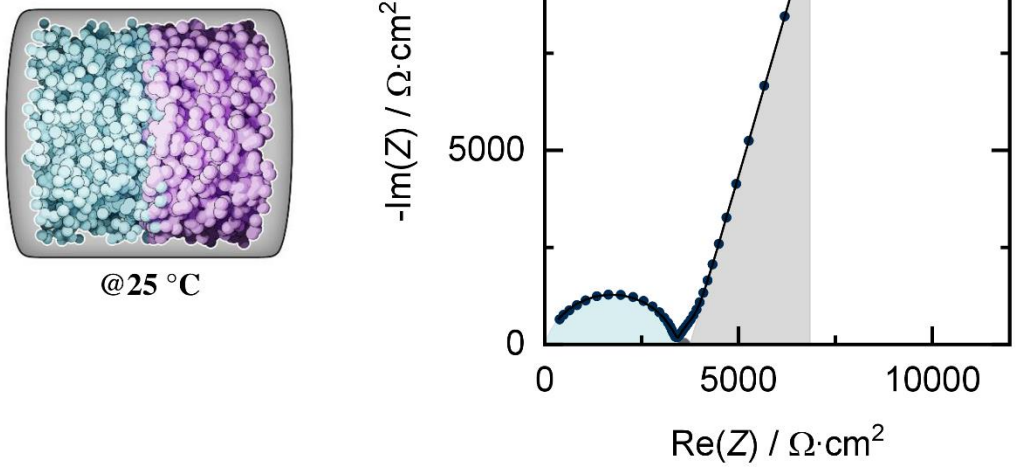

Figure S 7: Fitted impedance spectrum of a measurement at 25 °C of a cell with NEZC and Na_3SbS_4. The spectrum is fitted with two (R)(CPE) elements for the bulk and the interface resistance, as well as a CPE element for the contribution of the electronic resistance due to the ionically blocking electrodes which are stainless steel.

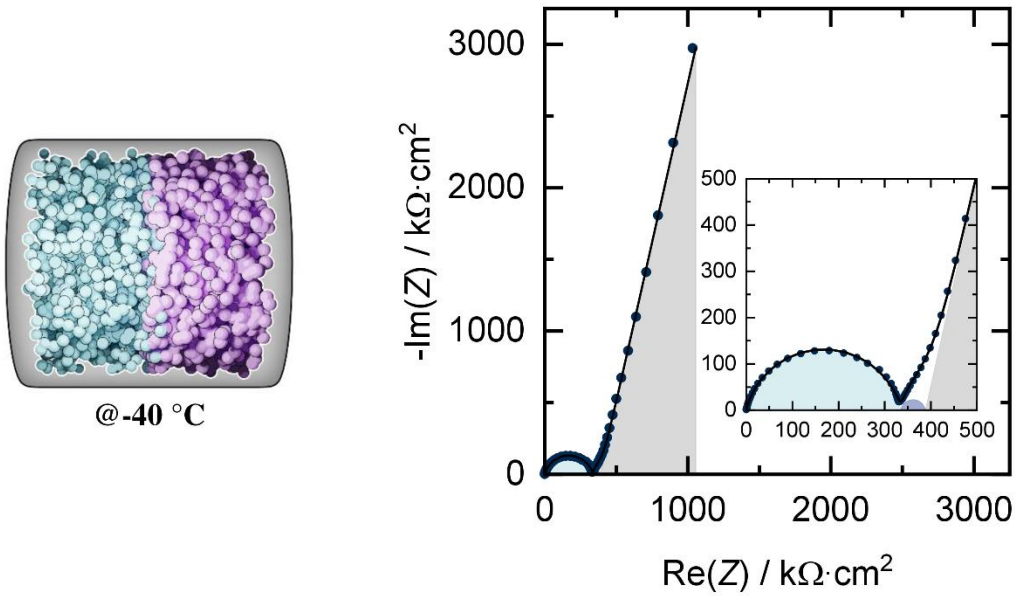

Figure S 8: Fitted impedance spectrum of a measurement at −40 °C of a cell with NEZC and Na_3SbS_4. The spectrum is fitted with two (R)(CPE) elements for the bulk and the interface resistance, as well as a CPE element for the contribution of the electronic resistance due to the ionically blocking electrodes which are stainless steel.

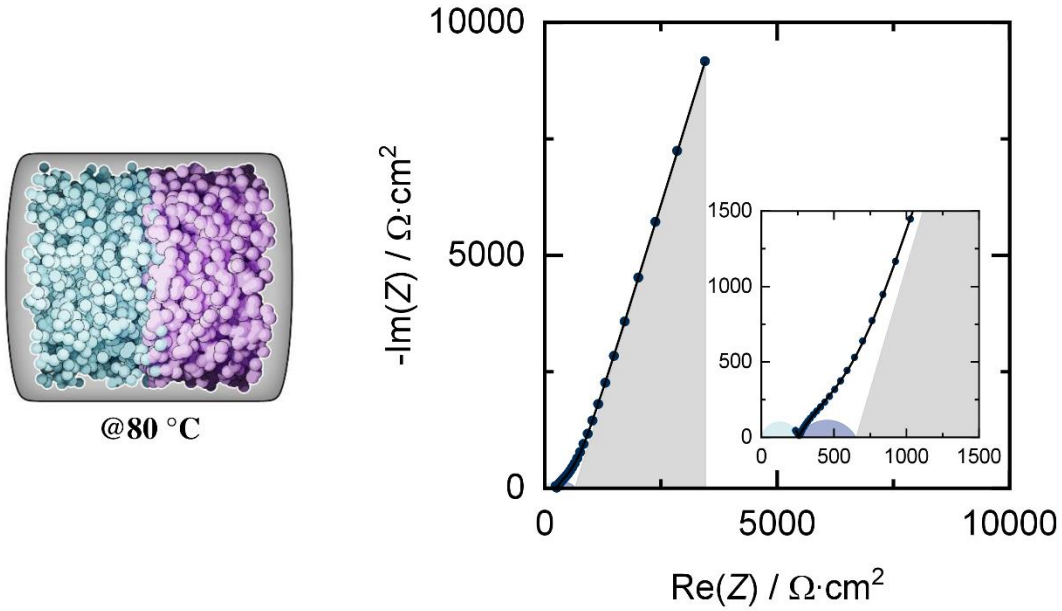

Figure S 9: Fitted impedance spectrum of a measurement at 80 °C of a cell with NEZC and Na_3SbS_4. The spectrum is fitted with two (R)(CPE) elements for the bulk and the interface resistance, as well as a CPE element for the contribution of the electronic resistance due to the ionically blocking electrodes which are stainless steel.

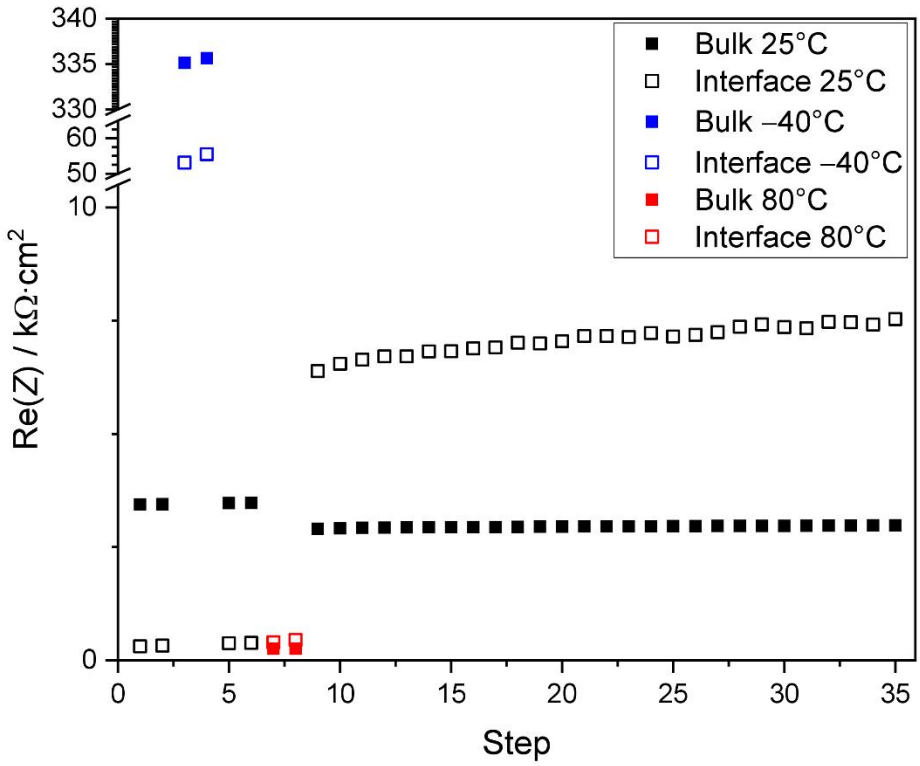

Figure S 10: Overview of the interface and bulk resistances with changing temperatures of a NEZC|Na_3SbS_4 cell. Each step is a 30 min OCV step in between impedance measurements.

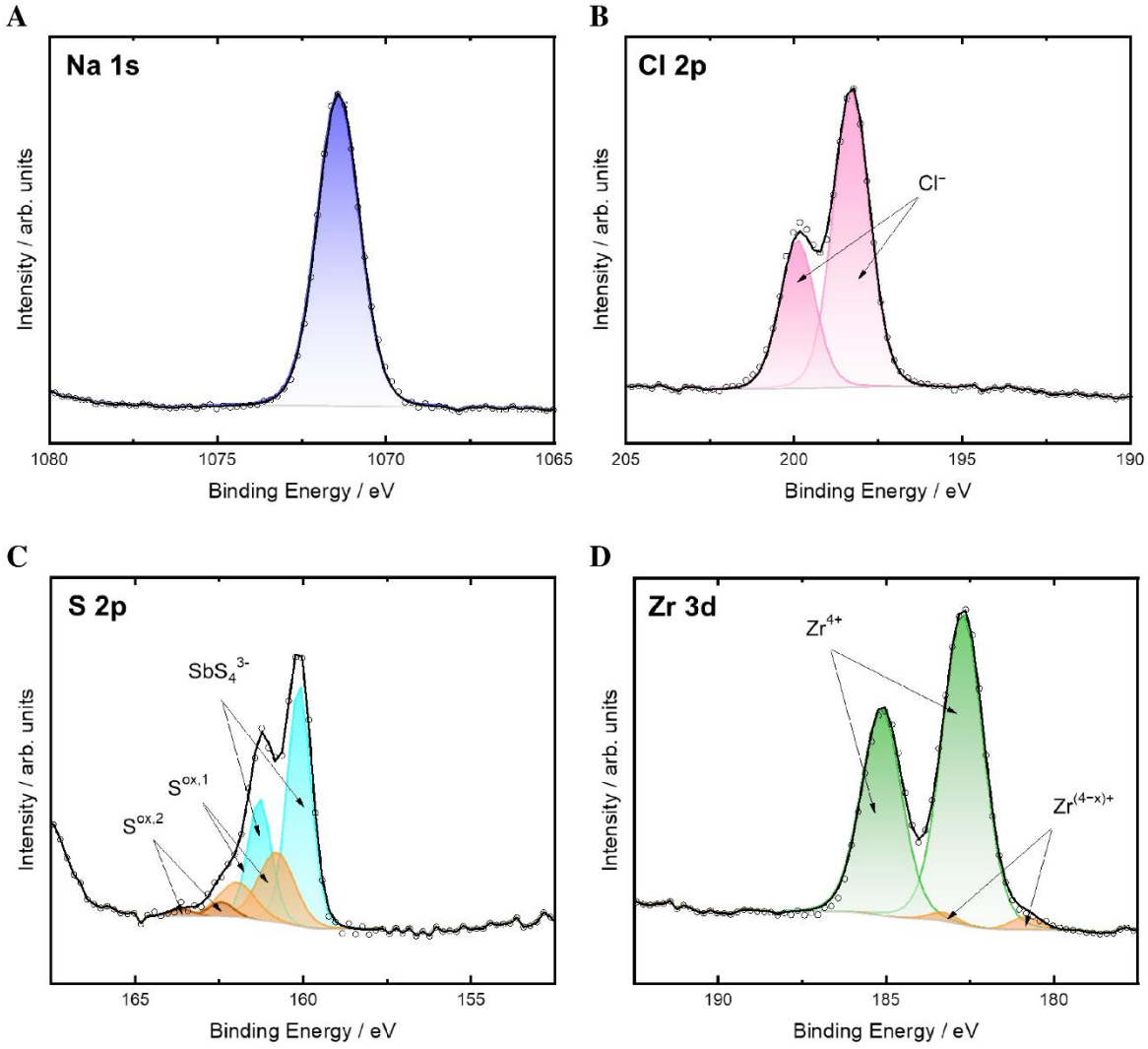

Figure S 11: XP spectra of Na_3SbS_4 mixed with NEZC represented by the Na 1s (A), Cl 2p (B), S 2p (C) and Zr 3d (D) signal. The S 2p signal shows two oxidized species ($S^{ox,1}$ and $S^{ox,2}$), apart from the expected SbS_4^{3-} doublet, the Zr 3d signal shows a minor reduced species ($Zr^{(4-x)+}$), apart from the expected Zr^{4+} doublet.

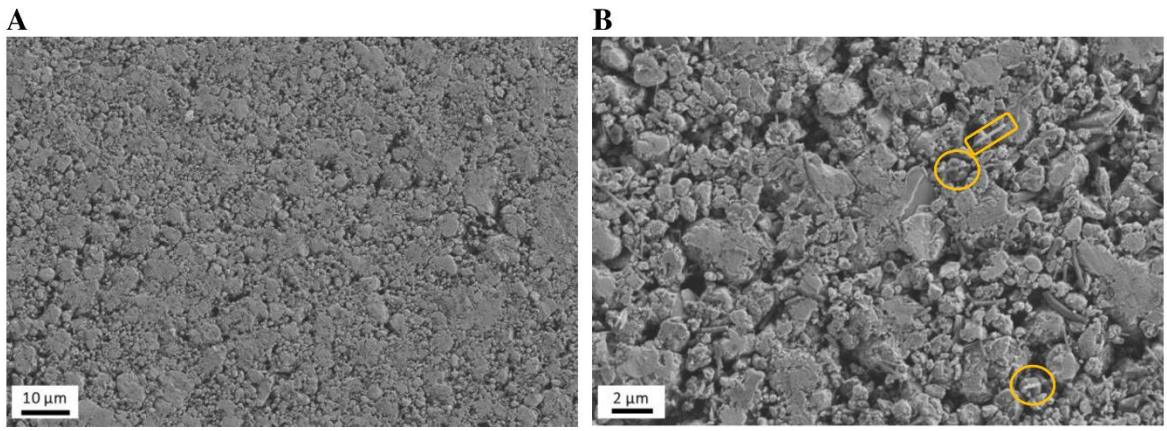

Figure S 12: SEM images of the NFMM:NEZC:VGCF composite in (A) ×1000 magnification (scale 10 µm) and (B) ×4000 magnification (scale 2 µm). Three VCGF fibers are marked with both yellow circles and rectangles in the SEM image (B).

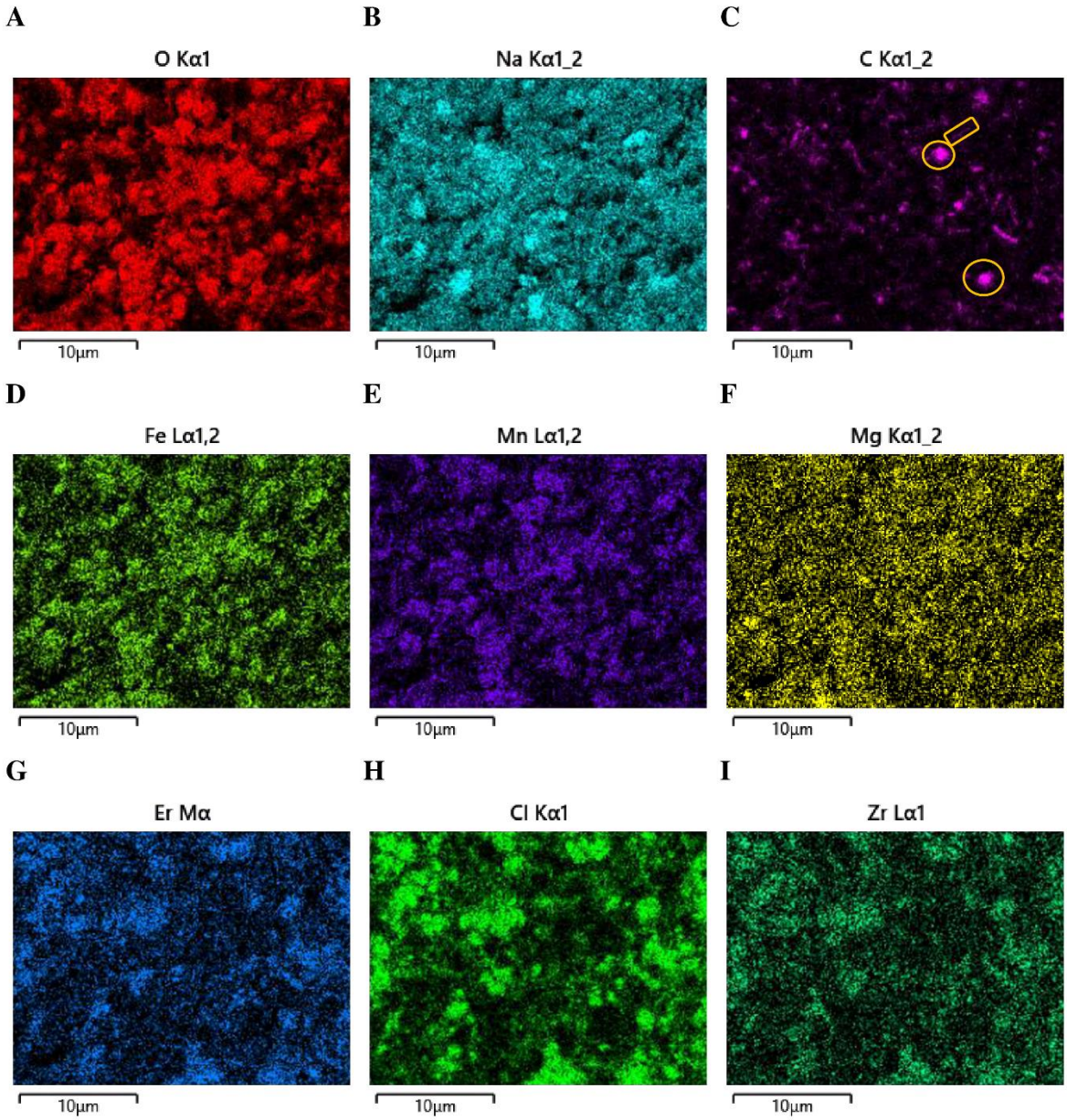

Figure S 13: EDX images of the NFMM:NEZC:VGCF composite shown in **Figure S 12**. (B) The Na $K_{\alpha1,2}$ line is characteristic for both CAM and solid electrolyte. The Fe $L_{\alpha1,2}$ (D), Mn $L_{\alpha1,2}$ (E), Mg $K_{\alpha1,2}$ (F) and O $K_{\alpha1}$ (A) are specific for the CAM, Er M_{α} (G), Cl $K_{\alpha1}$ (H) and Zr $L_{\alpha1}$ (I) for the solid electrolyte. The C $K_{\alpha1,2}$ signal (C) shows the carbon additive (VGCF) distribution in the composite. Three VCGF fibers as already marked in the SEM **Figure S 12** are also marked with yellow circles and rectangles in the EDX for C $K_{\alpha1,2}$.

6. List of Abbreviations

ASSB	All-solid-state battery
BEV	Battery electric vehicles
CAM	Cathode active material
CB	Conduction band
CE	Counter electrode
CEI	Cathode–electrolyte interphase
CPE	Constant phase element
DFT	Density functional theory
GITT	Galvanostatic intermittent titration technique
HOMO	Highest occupied molecular orbital
EDS/EDX	Energy-dispersive X-ray spectroscopy
EIS	Electrochemical impedance spectroscopy
LE	Liquid electrolyte
LIB	Lithium-ion battery
LMIG	Liquid metal ion gun
LUMO	Lowest unoccupied molecular orbital
MCI	Mixed conducting interphase
Me-ASSB	Metal all-solid-state battery
NaSICON	Sodium superionic conductor

6. List of Abbreviations

Na-ASSB	Sodium all-solid-state battery
NEZC	$Na_{2.4}Er_{0.4}Zr_{0.6}Cl_6$
NFM	$Na_{0.66}Fe_{0.5}Mn_{0.5}O_2$
NFMM	$Na_{0.66}Fe_{0.4}Mn_{0.5}Mg_{0.1}O_2$
OCV	Open-circuit voltage
PEEK	Polyether ether ketone
R	Electric resistance
RE	Reference electrode
SE	Solid electrolyte
SEI	Solid electrolyte inteface/interphase
SEM	Secondary electron microscopy
SI	Supporting information
SIB	Sodium-ion battery
SOC	State of charge
TMO	Transition metal oxide
ToF-SIMS	Time-of-flight secondary ion mass spectrometry
VB	Valence band
VGCF	Vapor grown carbon fibers
WE	Working electrode
XPS	X-ray photoelectron spectroscopy
XRD	X-ray diffraction

7. List of Symbols

a	[-]	Activity
C	[-]	C-rate
E	[V]	Electrode potential
$\vec{E}$	[V·m^{-1}]	Electric field
E^0	[V]	Standard electrode potential
E_a	[J·mol^{-1}]	Activation barrier
E_g	[eV]	Energy gap
F	[s·A·mol^{-1}]	Farraday constant
f	[Hz]	Frequency
I	[A]	Current
$\vec{J}$	[A·m^{-2}]	Current density
k_B	[J·K^{-1}]	Boltzmann constant
$\tilde{\mu}_{e^-}$	[V]	Electrochemical potential
ρ	[g·cm^{-3}]	Density
R	[J·mol^{-1}·K^{-1}]	Gas constant
σ	[S·cm^{-1}]	Electrical conductivity
σ_e	[S·cm^{-1}]	Electronic conductivity
σ_i	[S·cm^{-1}]	Ionic conductivity
σ_i^0	[s^{-1}]	Pre-exponential factor

7. List of Symbols

T	[K]	Temperature
t_{Na+}	[-]	Transference number of sodium
t_{Li+}	[-]	Transference number of lithium
U	[V]	Voltage
W_{vol}	[$J \cdot m^{-3}$]	Volumetric energy density
W_{grav}	[$J \cdot g^{-3}$]	Gravimetric energy density
Z	[Ω]	Impedance
z	[-]	Number of electrons

8. References

(1) Haynes, W. M.; Lide, D. R.; Bruno, T. J., Eds. *CRC Handbook of Chemistry and Physics*:*A Ready-Reference Book of Chemical and Physical Data*, 2016-2017, 97th edition; CRS Press, Taylor & Francis Group, 2016.

(2) H. Heimes; A. Kampker; B. Dorn; Christian Offermanns, G. Bockey, S. Wennemar; H. Clever; K. Sasse, J. Vienenkötter, N. Lackner; W. Bernhart; J.-P. Hasenberg; T. Hotz; D. Gallus; K. Koche; I. Demir; T. Haisch. Battery Monitor 2022:The Value Chain in the Field of Tension between Economy and Ecology, RWTH Aachen University, Aachen, 2022.

(3) Chayambuka, K.; Mulder, G.; Danilov, D. L.; Notten, P. H. L. From Li-Ion Batteries toward Na-Ion Chemistries: Challenges and Opportunities. *Adv. Energy Mater.* **2020**, *10* (38), 2001310.

(4) Titirici, M.-M.; Adelhelm, P.; Hu, Y.-S., Eds. *Sodium-ion batteries*:*Materials, characterization, and technology*; Wiley-VCH, 2023.

(5) Deng, J.; Luo, W.-B.; Chou, S.-L.; Liu, H.-K.; Dou, S.-X. Sodium-Ion Batteries: From Academic Research to Practical Commercialization. *Adv. Energy Mater.* **2018**, *8* (4), 1701428.

(6) M. Ridder. The Race for Solid-State Batteries:Six Challenges for Solid-State Batteries. *Porsche Consulting The Magazine*, 2023.

(7) Delmas, C.; Braconnier, J.-J.; Fouassier, C.; Hagenmuller, P. Electrochemical Intercalation of Sodium in NaxCoO2 Bronzes. *Solid State Ionics* **1981**, *3-4*, 165–169.

(8) Stevens, D. A.; Dahn, J. R. High Capacity Anode Materials for Rechargeable Sodium-Ion Batteries. *J. Electrochem. Soc.* **2000**, *147* (4), 1271.

(9) Jhang, L.-J.; Wang, D.; Silver, A.; Li, X.; Reed, D.; Wang, D. Stable All-Solid-State Sodium-Sulfur Batteries for Low-Temperature Operation Enabled by Sodium Alloy Anode and Confined Sulfur Cathode. *Nano Energy* **2023**, *105*, 107995.

(10) Tanibata, N.; Matsuyama, T.; Hayashi, A.; Tatsumisago, M. All-Solid-State Sodium Batteries using Amorphous TiS3 Electrode with High Capacity. *Journal of Power Sources* **2015**, *275*, 284–287.

(11) Fuchs, T.; Culver, S. P.; Till, P.; Zeier, W. G. Defect-Mediated Conductivity Enhancements in $Na_{3-x}Pn_{1-x}W_xS_4$ (Pn = P, Sb) Using Aliovalent Substitutions. *ACS Energy Lett.* **2020**, *5* (1), 146–151.

(12) Janek, J.; Zeier, W. G. Challenges in Speeding up Solid-State Battery Development. *Nat Energy* **2023**, *8* (3), 230–240.

(13) Ye, L.; Feng, Z. Polymer Electrolytes as Solid Solvents and their Applications. In *Polymer Electrolytes*; Elsevier, 2010; pp 550–582. DOI: 10.1533/9781845699772.2.550.

(14) Janek, J.; Zeier, W. G. A Solid Future for Battery Development. *Nat Energy* **2016**, *1* (9).

(15) Dudney, N. J.; West, W. C.; Nanda, J., Eds. *Handbook of solid state batteries*, Second edition; Materials and energy, Vol. 6; World Scientific, 2016.

(16) Zhao, J.; Wang, L.; He, X.; Wan, C.; Jiang, C. Determination of Lithium-Ion Transference Numbers in $LiPF_6$–PC Solutions Based on Electrochemical Polarization and NMR Measurements. *J. Electrochem. Soc.* **2008**, *155* (4), A292.

(17) Wolfenstine, J.; Go, W.; Kim, Y.; Sakamoto, J. Mechanical Properties of NaSICON: A Brief Review. *Ionics* **2023**, *29* (1), 1–8.

(18) Zhang, Z.; Zou, Z.; Kaup, K.; Xiao, R.; Shi, S.; Avdeev, M.; Hu, Y.-S.; Da Wang; He, B.; Li, H.; Huang, X.; Nazar, L. F.; Chen, L. Correlated Migration Invokes Higher Na^+-Ion Conductivity in NaSICON-Type Solid Electrolytes. *Adv. Energy Mater.* **2019**, *9* (42).

(19) Rush, L. E.; Hood, Z. D.; Holzwarth, N. A. W. Unraveling the Electrolyte Properties of Na_3SbS_4 through Computation and Experiment. *Phys. Rev. Materials* **2017**, *1* (7).

(20) Eckhardt, J. K.; Fuchs, T.; Burkhardt, S.; Klar, P. J.; Janek, J.; Heiliger, C. Guidelines for Impedance Analysis of Parent Metal Anodes in Solid-State Batteries and the Role of Current Constriction at Interface Voids, Heterogeneities, and SEI. *Adv Materials Inter* **2023**, *10* (8), 2202354.

(21) Bruce, P. G., Ed. *Solid State Electrochemistry*, 1. paperback ed.; Chemistry of solid state materials, Vol. 5; Cambridge Univ. Pr, 1997.

(22) Fertig, M. P.; Skadell, K.; Schulz, M.; Dirksen, C.; Adelhelm, P.; Stelter, M. From High- to Low-Temperature: The Revival of Sodium-Beta Alumina for Sodium Solid-State Batteries. *Batteries & Supercaps* **2022**, *5* (1).
(23) Cronau, M.; Szabo, M.; König, C.; Wassermann, T. B.; Roling, B. How to Measure a Reliable Ionic Conductivity? The Stack Pressure Dilemma of Microcrystalline Sulfide-Based Solid Electrolytes. *ACS Energy Lett.* **2021**, *6* (9), 3072–3077.
(24) Lacivita, V.; Wang, Y.; Bo, S.-H.; Ceder, G. Ab Initio Investigation of the Stability of Electrolyte/Electrode Interfaces in All-Solid-State Na Batteries. *J. Mater. Chem. A* **2019**, *7* (14), 8144–8155.
(25) Banik, A.; Famprikis, T.; Ghidiu, M.; Ohno, S.; Kraft, M. A.; Zeier, W. G. On the Underestimated Influence of Synthetic Conditions in Solid Ionic Conductors. *Chemical science* **2021**, *12* (18), 6238–6263.
(26) Wang, K.; Ren, Q.; Gu, Z.; Duan, C.; Wang, J.; Zhu, F.; Fu, Y.; Hao, J.; Zhu, J.; He, L.; Wang, C.-W.; Lu, Y.; Ma, J.; Ma, C. A Cost-Effective and Humidity-Tolerant Chloride Solid Electrolyte for Lithium Batteries. *Nature communications* **2021**, *12* (1), 4410.
(27) Deysher, G.; Chen, Y.-T.; Sayahpour, B.; Lin, S. W.-H.; Ham, S.-Y.; Ridley, P.; Cronk, A.; Wu, E. A.; Tan, D. H. S.; Doux, J.-M.; Oh, J. A. S.; Jang, J.; Nguyen, L. H. B.; Meng, Y. S. Evaluating Electrolyte-Anode Interface Stability in Sodium All-Solid-State Batteries. *ACS applied materials & interfaces* **2022**, *14* (42), 47706–47715.
(28) Riegger, L. M.; Schlem, R.; Sann, J.; Zeier, W. G.; Janek, J. Lithium-Metal Anode Instability of the Superionic Halide Solid Electrolytes and the Implications for Solid-State Batteries. *Angewandte Chemie (International ed. in English)* **2021**, *60* (12), 6718–6723.
(29) Park, K.-H.; Kaup, K.; Assoud, A.; Zhang, Q.; Wu, X.; Nazar, L. F. High-Voltage Superionic Halide Solid Electrolytes for All-Solid-State Li-Ion Batteries. *ACS Energy Lett.* **2020**, *5* (2), 533–539.
(30) Zhang, L.; Liu, Y.; You, Y.; Vinu, A.; Mai, L. NASICONs-Type Solid-State Electrolytes: The History, Physicochemical Properties, and Challenges. *Interdisciplinary Materials* **2023**, *2* (1), 91–110.
(31) Quérel, E.; Seymour, I. D.; Cavallaro, A.; Ma, Q.; Tietz, F.; Aguadero, A. The Role of NaSICON Surface Chemistry in Stabilizing Fast-Charging Na Metal Solid-State Batteries. *J. Phys. Energy* **2021**, *3* (4), 44007.
(32) Koerver, R.; Aygün, I.; Leichtweiß, T.; Dietrich, C.; Zhang, W.; Binder, J. O.; Hartmann, P.; Zeier, W. G.; Janek, J. Capacity Fade in Solid-State Batteries: Interphase Formation and Chemomechanical Processes in Nickel-Rich Layered Oxide Cathodes and Lithium Thiophosphate Solid Electrolytes. *Chem. Mater.* **2017**, *29* (13), 5574–5582.
(33) Minnmann, P.; Quillman, L.; Burkhardt, S.; Richter, F. H.; Janek, J. Editors' Choice—Quantifying the Impact of Charge Transport Bottlenecks in Composite Cathodes of All-Solid-State Batteries. *J. Electrochem. Soc.* **2021**, *168* (4), 40537.
(34) Kaufman, J. L.; van der Ven, A. Na_xCoO_2 Phase Stability and Hierarchical Orderings in the O3/P3 Structure Family. *Phys. Rev. Materials* **2019**, *3* (1).
(35) Nayak, P. K.; Yang, L.; Brehm, W.; Adelhelm, P. From Lithium-Ion to Sodium-Ion Batteries: Advantages, Challenges, and Surprises. *Angewandte Chemie (International ed. in English)* **2018**, *57* (1), 102–120.
(36) Yabuuchi, N.; Kajiyama, M.; Iwatate, J.; Nishikawa, H.; Hitomi, S.; Okuyama, R.; Usui, R.; Yamada, Y.; Komaba, S. P2-Type $Na_x[Fe_{1/2}Mn_{1/2}]O2$ Made from Earth-Abundant Elements for Rechargeable Na Batteries. *Nature materials* **2012**, *11* (6), 512–517.
(37) Yang, J.; Maughan, A. E.; Teeter, G.; Tremolet de Villers, B. J.; Bak, S.-M.; Han, S.-D. Structural Stabilization of P2-type Sodium Iron Manganese Oxides by Electrochemically Inactive Mg Substitution: Insights of Redox Behavior and Voltage Decay. *ChemSusChem* **2020**, *13* (22), 5972–5982.
(38) Wang, M. J.; Chang, J.-Y.; Wolfenstine, J. B.; Sakamoto, J. Analysis of Elastic, Plastic, and Creep Properties of Sodium Metal and Implications for Solid-State Batteries. *Materialia* **2020**, *12*, 100792.
(39) Singh, D. K.; Fuchs, T.; Krempaszky, C.; Mogwitz, B.; Burkhardt, S.; Richter, F. H.; Janek, J. Overcoming Anode Instability in Solid-State Batteries through Control of the Lithium Metal Microstructure. *Adv. Funct. Mater.* **2023**, *33* (1).

(40) Ham, S.-Y.; Yang, H.; Nunez-cuacuas, O.; Tan, D. H.; Chen, Y.-T.; Deysher, G.; Cronk, A.; Ridley, P.; Doux, J.-M.; Wu, E. A.; Jang, J.; Meng, Y. S. Assessing the Critical Current Density of All-Solid-State Li Metal Symmetric and Full Cells. *Energy Storage Materials* **2023**, *55*, 455–462.
(41) Ellis, L. D.; Hatchard, T. D.; Obrovac, M. N. Reversible Insertion of Sodium in Tin. *J. Electrochem. Soc.* **2012**, *159* (11), A1801-A1805.
(42) Sangster, J.; Bale, C. W. The Na-Sn (Sodium-Tin) System. *Journal of phase equilibria* **1998**, *19* (1), 76–81.
(43) Hume-Rothery, W. CXXV.—The System Sodium–Tin. *J. Chem. Soc.* **1928**, *0* (0), 947–963.
(44) Stratford, J. M.; Mayo, M.; Allan, P. K.; Pecher, O.; Borkiewicz, O. J.; Wiaderek, K. M.; Chapman, K. W.; Pickard, C. J.; Morris, A. J.; Grey, C. P. Investigating Sodium Storage Mechanisms in Tin Anodes: A Combined Pair Distribution Function Analysis, Density Functional Theory, and Solid-State NMR Approach. *Journal of the American Chemical Society* **2017**, *139* (21), 7273–7286.
(45) Goodenough, J. B.; Park, K.-S. The Li-Ion Rechargeable Battery: A Perspective. *Journal of the American Chemical Society* **2013**, *135* (4), 1167–1176.
(46) Thompson, T.; Yu, S.; Williams, L.; Schmidt, R. D.; Garcia-Mendez, R.; Wolfenstine, J.; Allen, J. L.; Kioupakis, E.; Siegel, D. J.; Sakamoto, J. Electrochemical Window of the Li-Ion Solid Electrolyte $Li_7La_3Zr_2O_{12}$. *ACS Energy Lett.* **2017**, *2* (2), 462–468.
(47) Peljo, P.; Girault, H. H. Electrochemical Potential Window of Battery Electrolytes: the HOMO–LUMO Misconception. *Energy Environ. Sci.* **2018**, *11* (9), 2306–2309.
(48) Zhang, Z.; Wenzel, S.; Zhu, Y.; Sann, J.; Shen, L.; Yang, J.; Yao, X.; Hu, Y.-S.; Wolverton, C.; Li, H.; Chen, L.; Janek, J. $Na_3Zr_2Si_2PO_{12}$: A Stable Na^+-Ion Solid Electrolyte for Solid-State Batteries. *ACS Appl. Energy Mater.* **2020**, *3* (8), 7427–7437.
(49) Qie, Y.; Wang, S.; Fu, S.; Xie, H.; Sun, Q.; Jena, P. Yttrium-Sodium Halides as Promising Solid-State Electrolytes with High Ionic Conductivity and Stability for Na-Ion Batteries. *The journal of physical chemistry letters* **2020**, *11* (9), 3376–3383.
(50) Wu, E. A.; Banerjee, S.; Tang, H.; Richardson, P. M.; Doux, J.-M.; Qi, J.; Zhu, Z.; Grenier, A.; Li, Y.; Zhao, E.; Deysher, G.; Sebti, E.; Nguyen, H.; Stephens, R.; Verbist, G.; Chapman, K. W.; Clément, R. J.; Banerjee, A.; Meng, Y. S.; Ong, S. P. A Stable Cathode-Solid Electrolyte Composite for High-Voltage, Long-Cycle-Life Solid-State Sodium-Ion Batteries. *Nature communications* **2021**, *12* (1), 1256.
(51) Tian, Y.; Sun, Y.; Hannah, D. C.; Xiao, Y.; Liu, H.; Chapman, K. W.; Bo, S.-H.; Ceder, G. Reactivity-Guided Interface Design in Na Metal Solid-State Batteries. *Joule* **2019**, *3* (4), 1037–1050.
(52) Wu, E. A.; Kompella, C. S.; Zhu, Z.; Lee, J. Z.; Lee, S. C.; Chu, I.-H.; Nguyen, H.; Ong, S. P.; Banerjee, A.; Meng, Y. S. New Insights into the Interphase between the Na Metal Anode and Sulfide Solid-State Electrolytes: A Joint Experimental and Computational Study. *ACS applied materials & interfaces* **2018**, *10* (12), 10076–10086.
(53) Hu, P.; Zhang, Y.; Chi, X.; Kumar Rao, K.; Hao, F.; Dong, H.; Guo, F.; Ren, Y.; Grabow, L. C.; Yao, Y. Stabilizing the Interface between Sodium Metal Anode and Sulfide-Based Solid-State Electrolyte with an Electron-Blocking Interlayer. *ACS applied materials & interfaces* **2019**, *11* (10), 9672–9678.
(54) Park, S. W.; Oh, G.; Park, J.-W.; Ha, Y.-C.; Lee, S.-M.; Yoon, S. Y.; Kim, B. G. Graphitic Hollow Nanocarbon as a Promising Conducting Agent for Solid-State Lithium Batteries. *Small (Weinheim an der Bergstrasse, Germany)* **2019**, *15* (18), e1900235.
(55) Walther, F.; Randau, S.; Schneider, Y.; Sann, J.; Rohnke, M.; Richter, F. H.; Zeier, W. G.; Janek, J. Influence of Carbon Additives on the Decomposition Pathways in Cathodes of Lithium Thiophosphate-Based All-Solid-State Batteries. *Chem. Mater.* **2020**, *32* (14), 6123–6136.
(56) Riegger, L. M.; Mittelsdorf, S.; Fuchs, T.; Rueß, R.; Richter, F. H.; Janek, J. Evolution of the Interphase between Argyrodite-Based Solid Electrolytes and the Lithium Metal Anode─The Kinetics of Solid Electrolyte Interphase Growth. *Chem. Mater.* **2023**, *35* (13), 5091–5099.
(57) Richards, W. D.; Miara, L. J.; Wang, Y.; Kim, J. C.; Ceder, G. Interface Stability in Solid-State Batteries. *Chem. Mater.* **2016**, *28* (1), 266–273.

(58) Zhu, Y.; He, X.; Mo, Y. First Principles Study on Electrochemical and Chemical Stability of Solid Electrolyte–Electrode Interfaces in All-Solid-State Li-Ion Batteries. *J. Mater. Chem. A* **2016**, *4* (9), 3253–3266.
(59) Walther, F.; Koerver, R.; Fuchs, T.; Ohno, S.; Sann, J.; Rohnke, M.; Zeier, W. G.; Janek, J. Visualization of the Interfacial Decomposition of Composite Cathodes in Argyrodite-Based All-Solid-State Batteries Using Time-of-Flight Secondary-Ion Mass Spectrometry. *Chem. Mater.* **2019**, *31* (10), 3745–3755.
(60) Edelman, D. A.; Brandt, T. G.; Temeche, E.; Laine, R. M. Sodium-Based Solid Electrolytes and Interfacial Stability. Towards Solid-State Sodium Batteries. *Materials Today Communications* **2022**, *32*, 104009.
(61) Culver, S. P.; Koerver, R.; Zeier, W. G.; Janek, J. On the Functionality of Coatings for Cathode Active Materials in Thiophosphate-Based All-Solid-State Batteries. *Adv. Energy Mater.* **2019**, *9* (24), 1900626.
(62) Kitsche, D.; Tang, Y.; Hemmelmann, H.; Walther, F.; Bianchini, M.; Kondrakov, A.; Janek, J.; Brezesinski, T. Atomic Layer Deposition Derived Zirconia Coatings on Ni-Rich Cathodes in Solid-State Batteries: Correlation Between Surface Constitution and Cycling Performance. *Small Science* **2023**, *3* (2).
(63) Hwang, J.-Y.; Myung, S.-T.; Choi, J. U.; Yoon, C. S.; Yashiro, H.; Sun, Y.-K. Resolving the Degradation Pathways of the O3-Type Layered Oxide Cathode Surface through the Nano-Scale Aluminum Oxide Coating for High-Energy Density Sodium-Ion Batteries. *J. Mater. Chem. A* **2017**, *5* (45), 23671–23680.
(64) Leng, M.; Bi, J.; Wang, W.; Xing, Z.; Yan, W.; Gao, X.; Wang, J.; Liu, R. Ultrathin MgO Coating on Fabricated O3–$NaNi_{0.45}Mn_{0.3}Ti_{0.2}Zr_{0.05}O_2$ Composite Cathode via Magnetron Sputtering for Enhanced Kinetic and Durable Sodium-Ion Batteries. *Journal of Alloys and Compounds* **2021**, *855*, 157533.
(65) Alvarado, J.; Ma, C.; Wang, S.; Nguyen, K.; Kodur, M.; Meng, Y. S. Improvement of the Cathode Electrolyte Interphase on P2-$Na_{2/3}Ni_{1/3}Mn_{2/3}O_2$ by Atomic Layer Deposition. *ACS applied materials & interfaces* **2017**, *9* (31), 26518–26530.
(66) Turgeman, M.; Fayena-Greenstein, M.; Bublil, S.; Shpigel, N.; Tsubery, M. N.; Chae, M.; Elias, Y.; Aurbach, D. Improved High-Energy Na-NCM Cathode Prepared by Ion Exchange Route via Application of Various ALD Treatments. *J. Electrochem. Soc.* **2021**, *168* (1), 10537.
(67) Chun, G. H.; Gong, S. H.; Kim, H.-S.; Shim, J. H.; Yu, S. Enhancing the Interfacial Stability of All-Solid-State High-Energy Sodium-Ion Batteries by Coating Materials: First Principles Calculations. *Applied Surface Science* **2023**, *616*, 156479.
(68) Minnmann, P.; Strauss, F.; Bielefeld, A.; Ruess, R.; Adelhelm, P.; Burkhardt, S.; Dreyer, S. L.; Trevisanello, E.; Ehrenberg, H.; Brezesinski, T.; Richter, F. H.; Janek, J. Designing Cathodes and Cathode Active Materials for Solid-State Batteries. *Adv. Energy Mater.* **2022**, *12* (35).
(69) Bielefeld, A.; Weber, D. A.; Janek, J. Microstructural Modeling of Composite Cathodes for All-Solid-State Batteries. *J. Phys. Chem. C* **2019**, *123* (3), 1626–1634.
(70) Hertle, J.; Walther, F.; Mogwitz, B.; Schröder, S.; Wu, X.; Richter, F. H.; Janek, J. Miniaturization of Reference Electrodes for Solid-State Lithium-Ion Batteries. *J. Electrochem. Soc.* **2023**.

8. References

9. Acknowledgements

I would like to express my sincere gratitude to:

Prof. Janek for giving me the opportunity to dive into my PhD journey from a non-electrochemistry background and for letting me choose a research topic where I felt I could apply my strengths. Your support from the get-go, your backup when needed, and the trust you placed in me to eventually work very independently mean a lot. Thank you for fostering a great atmosphere within the group, both socially and academically.

Felix H. Richter for your supervision and especially for asking the right questions that helped me find the "*roten Faden*" in my papers.

Prof. Philipp Adelhelm for agreeing to be my second reviewer and for your positive attitude in all our interactions. Also, thanks to Prof. Bernd Smarsly and Prof. Maren Lepple for being part of my examination committee.

Matthias Elm, Anja Henß, Bjoern Luerßen, Boris Mogwitz, Klaus Peppler, Marcus Rohnke, Joachim Sann for your assistance in various matters, whether personal, scientific or bureaucratic.

My colleagues, both past and present, many of whom became really good friends.

My "crew" whose friendship has meant a lot to me, especially during the challenging times of the pandemic: Jonas Hertle, Philip Minnmann and Julian Zahnow. Thanks for many fun hours both at work and outside the office.

My office mates – Christoph Alt, Ronja Haas, Julian Kreißl, Kathrin Michel, David Schäfer, Johannes Schubert and Manuel Weiß – for a wonderful working and non-working atmosphere.

Michele Bastianello, Sören Baumann, Juri Becker, Anja Bielefeld, Till Fuchs, Philip Klement, Sascha Kremer, Elisa Monte, Steffen Schröder, Kilian Vettori. Each of you deserves a shout-out for your unique roles in enriching my PhD journey and overall life.

My friends outside the AG Janek and especially to my two closest friends. Miriam Hoffmann for the countless laughs and good times during our joint studies and our PhD phases, and for encouraging me to pursue my path all the way to this point and Jennifer Budnik, my Jenny, for being there for me, no matter what, since 1992.

My dear sister Clara and to my *Mama* and my *Papa*, who believed in me even if my plans sounded a bit far-fetched and my work a bit like gibberish. I am profoundly grateful for your encouragement, your boundless love, understanding and belief in my abilities. Your support means everything to me.

My loving sister Tanja, who made me promise to mention her by name in my Nobel Prize acceptance speech for sodium solid-state batteries. Though that might be a stretch, I want to thank you for everything. I herewith pronounce my deepest gratitude for having you as my big sister. I will always look up to you, even if I surpassed you in height a long time ago. Thank you and I love you!